Department of AERONAUTICS and ASTRONAUTICS
STANFORD UNIVERSITY

AD672589

DENIS WAI-MAN TSAO

PITOT-PRESSURE MEASUREMENTS WITH RAPIDLY TRAVERSING PROBES IN THE WAKE OF A SPHERE IN A DIVERGING HYPERVELOCITY STREAM

APRIL
1968

SUDAAR
NO. 341

AD 672 589

PITOT-PRESSURE MEASUREMENTS WITH P^PIDLY TRAVERSING
PROBES IN THE WAKE OF A SFHF∂E IN A DIVERGING HYPER-
VELOCITY STREAM

Denis Wai-man Tsao

Stanford University
Stanford, California

April 1968

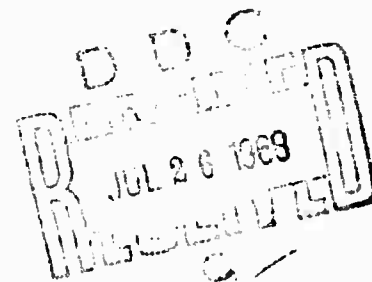Department of Aeronautics and Astronautics
Stanford University
Stanford, California

PITOT-PRESSURE MEASUREMENTS WITH RAPIDLY TRAVERSING PROBES IN THE WAKE OF A SPHERE IN A DIVERGING HYPERVELOCITY STREAM

by

Denis Wai-man Tsao

SUDAAR No. 341

April 1968

ACKNOWLEDGMENTS

TABLE OF CONTENTS

TABLE OF CONTENTS (Cont'd)

LIST OF ILLUSTRATIONS

LIST OF ILLUSTRATIONS (cont'd)

LIST OF SYMBOLS

A	tunnel cross-sectional area in Section 4.2; area in general
A_E	effective area of inviscid core flow in tunnel
A^*	sonic area
C_D	drag coefficient
d	diameter of sphere, $i = 2$ inches
$G(s)$	transfer function, Eq. (3.1)
$G(z)$	z-transform of transfer function $G(s)$, Eq. (3.9)
$\tilde{G}(z)$	z-transform of transfer function of transducer-galvanometer system including data hold, Eqs. (3.12)
$G_1(s)$	transfer function of transducer-amplifier stage, Eq. (A.1)
$G_2(s)$	transfer function of galvanometer, Eq. (A.2)
$g^{(0)}$	first-order term in blast-wave pressure expansion, Eqs. (4.7) and (4.12)
h	enthalpy
k	correction factor for transducer, also defined as "dynamic calibration factor"
k_s	blast-wave source-flow parameter, Eq. (4.6)
L	distance from nozzle throat, Fig. 17
L_o	distance from origin of virtual source, Fig. 17
M	Mach number
M_{sw}	Mach number of shock wave in response experiment
n	distance in boundary layer normal to body surface
$P_{in}(s)$	Laplace transform of $p_{in}(t)$, Eq. (3.1)
$P_{in}(z)$	z-transform of $p_{in}^*(t)$, Eq. (3.6)
$P_{out}(s)$	Laplace transform of $p_{out}(t)$, Eq. (3.1)
$P_{out}(z)$	z-transform of $p_{out}^*(t)$, Eq. (3.7)

p   static pressure

$p_{in}(t)$ input signal in general; pressure input in particular

$p_{in}^*(t)$ sampled input

$p_{out}(t)$ output signal in general; pressure output in particular

$p_{out}^*(t)$ sampled output

p_o' Pitot pressure

$Q(z,s)$ transfer function of data-hold circuit at input, Eq. (3.10)

R   distance from axis of symmetry to bow shock wave, Fig. 1

R_o normalizing constant for shock-wave radius in blast-wave theory, Eq. (4.10)

Re   Reynolds number

r   radial coordinate from axis of symmetry, Fig. 1; $r = |v|$

$\hat{r}$ r/R

r_b radius of sphere $r_b = 1$ inch

r_f radius of viscous wake

S   enthalpy function, $h/h_{t_{ex}} - 1$

s   Laplace variable; also, distance in boundary layer tangential to body surface

T   temperature; also, sampling period

t   time

V   velocity

x   longitudinal distance, downstream from nose of model, Fig. 1

x_n abbreviation for $p_{in}(nT)$, Appendix C

y   rectilinear transverse coordinate, Fig. 1

y_n abbreviation for $p_{out}(nT)$, Appendix C

z	z-transform, Eq. (3.4)
β	pressure-gradient parameter, Eqs. (D.4) and (D.5)
γ	ratio of specific heats
δ	boundary-layer thickness; also, idealized rise time for transducer-amplifier stage, $\delta = 0.211$ milliseconds
$\delta(t)$	delta function representing unit impulse at $t = 0$
ϵ	blast-wave expansion parameter, Eq. (4.8); also, used in Appendix C to denote error in input
ζ	transformed boundary-layer coordinate, Eq. (D.1b); also, damping ratio of galvanometer, $\zeta = 0.6266$
η	boundary-layer similarity variable, Eq. (D.2)
ρ	density
φ	angle from stagnation point, Fig. 1
ψ	pressure function associated with second-order term in blast-wave pressure expansion, Eq. (4.7)
ω_n	undamped natural frequency of galvanometer, Eq. (3.3), $\omega_n = 1900$ radians/second

Subscripts:

1	conditions in free stream just upstream of bow shock wave; precise location in free stream must be specified because of tunnel source flow
2	conditions downstream of bow shock wave; in most instances identified with wake conditions, Fig. 1
bl	pertaining to boundary layer
e	values at edge of viscous wake
ex	values in inviscid flow just external to boundary layer
m	measured values
n	conditions in free stream at nose of model
o	conditions just downstream of wake neck

s   pertaining to source flow

t   total conditions

u   pertaining to uniform flow

w   values at model surface

Superscripts:

~ $\tilde{Q} = Q/Q_o$, for any quantity Q

-        for distances: nondimensionalized with respect to d; for
         T and δ: $\bar{T} = \omega_n T$, $\bar{\delta} = \omega_n \delta$

1. INTRODUCTION

The study of wakes behind objects is a challenging problem in fluid
mechanics. Even for the least complicated cases involving incompressible
flow past simple body shapes, there does not exist a unified theory that
provides a satisfactory solution to the problem. This is because wake
flow may be considered as a juxtaposition of a number of flow phenomena —
i.e., free shear layers, turbulence, and flow separation — that have yet
to be understood properly on an individual basis. In view of the intrac-
table nature of the wake problem, it is not surprising that until recently
research in this area was somewhat fragmentary.

The advent of ballistic missiles and other reentry vehicles, however,
has provided the impetus for a concerted effort to study the wake problem,
particularly in the hypervelocity flow regime. The motivation lies in
the need to monitor reentry vehicles through the observation of their
trail, that is, to relate the dimensional characteristics of the vehicle
to the observable quantities in the wake, such as length of trail or
radar cross section. Research activities along these lines have therefore
increased markedly during the past ten years. This is evidenced by the
fact that in a survey article on recent work, Lykoudis (1966) cites well
over a hundred references. Yet despite these efforts, there still re-
mains a lack of thorough understanding of the basic flow mechanisms within
the wake. This state of affairs attests to the particularly complex na-
ture of the problem in the hypervelocity regime.

To appreciate the essential features of the hypervelocity wake,
consider the flow field for a sphere as sketched in Fig. 1. The regions
that dominate the picture are the recirculation zone and the viscous wake
downstream of it. The origins of the viscous wake can be traced to the
boundary layer over the front half (approximately) of the sphere. Near
the meridian $\varphi = \pi/2$ (the angle φ defined in Fig. 1), the boundary
layer separates to form an annular, free shear layer which subsequently
coalesces near the wake neck and becomes the viscous wake. The flow
within the viscous wake is initially laminar but becomes turbulent

1

somewhere downstream. The position at which transition occurs is dependent on the Reynolds number. Outside the viscous wake, the flow field conforms essentially to the inviscid field around a hemisphere-cylinder model.[*]

In the foregoing model of the wake flow, several distinctive problem areas can be discerned: (1) the separation of the boundary layer and its subsequent role as a free shear layer; (2) the complex flow structure of the "dead-water" region or recirculation zone; (3) the viscous-inviscid interaction of the free shear layer with the outer flow as well as viscous interaction with the recirculation zone; and (4) the problem of laminar-to-turbulent transition and the description of the transport mechanisms in the viscous wake when turbulence sets in. In all of these areas the effects of compressibility and of heat transfer to the body must be taken into account in the hypervelocity case. The theoretician is thus confronted with many complex problems in his attempt at finding wake solutions. At the experimental level, the difficulty with which data can be obtained under hypervelocity flow conditions makes it hard to achieve a comprehensive verification of theoretical solutions.

In an attempt five years ago to gain insight into the wake problem, an experimental program was initiated at Stanford University to study the wake flow behind a circular cylinder in a spark-heated wind tunnel. The original program called for mapping the velocity field in the wake with "tracer-spark" equipment as well as for Pitot-pressure surveys with conventional methods. The tracer-spark technique for velocity measurement was first used for low-speed flows by Bomelburg (1958); an extension of the method to the hypervelocity flow regime was made by Kyser (1964). In addition to the velocity and Pitot-pressure measurements, exploratory studies were also planned to determine the feasibility of using the phenomenon of resonance scattering to detect laminar-to-turbulent transition in the viscous wake. To achieve resonance scattering in the nitrogen stream of the tunnel, a nitrogen laser was to be used as the light source.

---

[*] The presence of the recompression shock wave modifies somewhat the inviscid flow field.

The exploratory studies showed, however, that the laser originally intended for the resonance-scattering experiments did not have sufficient power output for use with commercially available photorecording films or plates. The transition studies were therefore abandoned. As to the mapping of the velocity field, it was found that the gradients in the wake were too severe for the tracer-spark technique to apply.[*] As a result of these instrumentation limitations, the wake-studies program was reduced essentially to the surveying of Pitot pressure.

The measurement of wake Pitot pressure in itself is a fairly routine undertaking. Detailed surveys have been made by McCarthy (1962), for example, for the case of a circular cylinder at a Mach number of 5.8. In McCarthy's work, heat transfer was negligible since the tests were conducted in a steady-flow tunnel. Smith, Kramer, and Brown (1966), on the other hand, measured the Pitot pressure behind a cylinder under conditions where heat-transfer effects were important. In this instance, the tests were performed in a short-duration tunnel at hypervelocity conditions (free-stream Mach number approximately 20), and the data were obtained with a conventional rake fixed with respect to the tunnel.

The experiments to be reported herein were performed at flow conditions similar to those of Smith et al. Differences exist, however, in the type of model used and in the technique employed to survey the Pitot pressure. In place of the conventional stationary rake typical of short-duration testing facilities, use was made of rapidly moving spring-driven probes capable of recording continuous pressure data along a traversed path within the wake. This was done to increase the data-gathering capability of the available pressure-recording system and to improve the quality of data that could have been achieved with stationary rakes. To cover the entire wake region, two traversing probes were used, one for axial traverses and the other for traverses across the wake. Because of the short tunnel running times, these probes were made to be

_____

[*] Research efforts on this technique were then directed toward studying the details of the sparking process itself. This was done to establish the measuring accuracy that can be expected when the technique is used for measuring free-stream velocity (see Kyser, 1967).

3

capable of high speeds of traverse (35 fps and 60 fps, respectively). In addition to the rapidly driven probes, a second innovation was the implementation of a technique that permitted testing in the wake of a support-free sphere. A description of these systems and the associated apparatus, together with a more detailed discussion of the motivation for the use of traversing probes, is given in Chapter 2.

The use of rapidly traversing probes, though facilitating the gathering of data, introduced an instrumentation problem of unexpectedly serious proportions. After a considerable portion of the testing had been completed, it became apparent that the pressure-recording system used in conjunction with the traversing probes did not have a fast enough response to cope with the rapidly changing pressure signal encountered during a traverse across the wake. As a result, the recorded pressure output exhibited considerable time lag and distortion of shape. In an attempt to resolve this problem, a combined experimental and analytical study was made to ascertain the response characteristics of the system, comprised of a pressure transducer, carrier amplifier, and galvanometer. With the response characteristics known, it is possible to use the solution of an analogous problem in the theory of sampled-data control systems to devise a scheme for correcting the galvanometer output for response lag. A discussion of the response problem and an outline of the subsequent correction scheme is given in Chapter 3.

A second difficulty in the experiments, also recognized only after most of the testing had been performed, was the seriousness of the tunnel source-flow effect on the test data. It became apparent that because of the large downstream distances involved in wake testing, the expanding stream in the conical nozzle could significantly affect both the magnitude of the Pitot pressure and the rate of growth of the wake. The suspected source-flow effect on the magnitude of the Pitot pressure has been verified (in the inviscid portion of the wake) by the use of results from the method of characteristics, and this is explained in Chapter 4. By means of a combination of available source-flow solutions, including some method-of-characteristics results, an approximate scheme is then devised to correct both the magnitude of the measured Pitot pressure and the lateral wake dimension.

4

The salient points in the final overall data-reduction procedure are discussed in Chapter 5. These include the essential steps in the application of the correction schemes — for both response lag and source-flow effects — to the experimental data. Representative Pitot-pressure results, after appropriate correction, are also presented and discussed. The corrections are quite large in some cases and lead to significant changes in the shape of the Pitot-pressure profiles. Because of the lack of data that are free of errors due to response lag and source-flow effects, it is not possible to make a direct assessment of the accuracy of the corrections. The scheme for correcting response lag is checked, however, by applying it to a constructed test case. Also, the magnitude of the source-flow correction compares favorably with the results from the method of characteristics. On the basis of these indirect, partial checks, it is believed that the corrections represent an improvement on the raw data.

5

2. APPARATUS AND TEST CONDITIONS

2.1 Wind Tunnel and Model

The experiments were performed in the Stanford University spark-heated wind tunnel, shown schematically in Fig. 2. This tunnel, which uses nitrogen as the test gas, has a useful run time of about 30 milliseconds. The nominal test-section Mach number is 17. It is possible to vary free-stream conditions such as density and temperature by appropriate choice of throat size, initial gas density in the arc chamber, and amount of energy imparted to the gas through the arc discharge. One can, for example, achieve a tenfold variation in the Reynolds number. A discussion of the range and variation of Reynolds number and stagnation temperature encountered in the experiments is given in Section 2.7 under "Test Conditions." A detailed description of the tunnel and its operation appears in the work of Karamcheti, Vali, and Vincenti (1961).

The model is a 2-inch-diameter sphere, a commercially available steel ball bearing. Its location with respect to the tunnel differs according to which portion of the wake is being studied. The alternative of fixing the sphere location and changing the position of the probe is not feasible, since the probe units are heavy and bulky, and once they are installed in the tunnel, they remain in their specified position of installation. In the actual arrangement, the sphere is placed in the portion of the nozzle upstream of the nominal test section, which is in fact a portion of the nozzle. In the course of the tests, eight different stations were used. These are illustrated in Fig. 3, which also contains a schedule of their distance from the vertically traversing probe.

Since the flow in the nozzle is continuously expanding, free-stream conditions at the different stations are not the same, even for identical conditions in the test section. A more complete discussion of the longitudinal variation in stream properties is given in Section 4.2.

2.2 Model Suspension and Release

The task of obtaining wake data behind three-dimensional models in a wind tunnel is inherently difficult. This results from the fact that

6

one cannot support the model from the rear, as is usually done when measuring some quantity, such as surface pressure, on the model itself. Several attempts have been made at various ways of supporting three-dimensional models by means of thin wires or rods (see, for example, Demetriades and Bauer, 1966). None of these methods has been proven to be unquestionably reliable, however. A different approach is used in the work of Vas, Murman, and Bogdonoff (1965). In this instance the model, a sphere, is magnetically suspended in the stream, so that the resulting wake flow is genuinely free of support interference.

The present study is similar to the work of Vas et al. in that a three-dimensional model is used. There is, however, a major difference in the method of suspension. In contrast to the steady-state wind tunnel used by Vas et al., the tunnel employed for the present work has the relatively short running time of 30 milliseconds. In this case, if the model is suddenly released (i.e., left unsupported) in the tunnel at the start of a run, it will not fall appreciably from the effects of gravity over the duration of the run. Even if the vertical drop of the model is not completely negligible, it can be calculated from the usual time-distance relation for free fall. The problem of testing behind a support-free model is thus merely one of devising a means of releasing the model just before flow is established in the tunnel.

A system capable of this type of release for the special case of a sphere is shown in Fig. 4. Before the run, the sphere is suspended by a wire spotwelded to the sphere. At the start of the run, the wire is given a sudden pull, whereupon the weld breaks and the sphere is released into the stream. If the weld is weak enough, and if the impulse supplied by the pull is sufficiently large to break the weld instantaneously, only a small fraction of the energy (of the pulling motion) will be transmitted to the sphere. The little that is transmitted does not raise the sphere appreciably, by virtue of the sphere's large inertial mass (about 1.2 lbm.). An experiment was performed to verify the fact that the rise is negligible. The sphere was suspended between a light source and a photocell so that any movement of the sphere affected the amount of light entering the photocell. It was thus possible to relate the photocell output to the

7

verticle position of the sphere. With this system, it was found that the rise of the sphere was indeed negligible.

Considerable effort was required to find a spotwelding process that provides a weak enough weld. The weld must also, of course, be strong enough to support the weight of the sphere. An important factor in controlling the spotweld was found to be the material of the wire. Another question to be considered in the choice of the wire is the tensile strength of the wire relative to the strength of the weld. Although it is desirable to use a thin wire to achieve a weak weld, an excessively thin wire tends to stretch and break when the pull is applied. After some experimentation, it was found that the best results were obtained with a relatively thick tinned copper wire (gage no. 22). In subsequent tests, the spotwelding process was carefully controlled.

The mechanism for providing the sudden pull on the suspension wire is also shown in Fig. 4. A heavy mass is set in motion by the energy stored in the compressed spring, and the momentum of this moving mass is used to supply the pull. The mass is initially restrained from motion by a locked cam, which is released through the action of a rotary solenoid. The triggering assembly is similar to the one in the vertically traversing probe and is described in detail in Section 2.4. A predetermined amount of slack is provided in the music wire that connects the mass to the suspension wire. The mass is thus permitted to acquire a predetermined speed before it is made to break the weld and withdraw the suspension wire. This speed is necessary so that the wire will clear the flow field rapidly. In addition, the moving mass then exerts a large enough impulsive force on the weld to break it instantaneously.

As the mass travels along the guide tube, it trips two microswitches that are installed inside a slot cut along one side of the tube (see Fig. 4). The signal from the first switch indicates the instant at which the spotweld is broken, thereby supplying the information needed to calculate the free fall of the sphere. The second switch is located three inches from the first and thus indicates the instant at which the tip of the suspension wire is three inches from the point of the weld (or four inches from the tunnel axis, since the radius of the sphere is one inch). At

8

this instant, the tip of the wire has cleared the inviscic core flow of the tunnel – the inviscid core flow having a maximum radius of about four inches (see Section 4.2) – and the wire is assumed to have negligible effect on the flow field around the sphere. By means of the second switch, it is thus possible to ensure that the pressure probing is done only after a clean flow field has been established.

2.3 Traversing Pressure Probes

With a wind tunnel of the steady-flow type, it is common practice to make traverses with various types of probes within a given region of interest. For a short-duration tunnel, however, conventional motor-driven probes are too slow. To survey the Pitot pressure, for example, one may then resort to the use of a stationary rake with an array of impact tubes. An example of this procedure is the work of Smith, Kramer, and Brown (1966), where a stationary rake was used to survey the Pitot pressure in the wake of a circular cylinder, also in a spark-heated tunnel. The disadvantage of such a fixed rake is that a large amount of instrumentation must be available. A still more serious difficulty lies in the fact that the impact tubes cannot be too closely spaced, or shock interaction between adjacent tubes will result. Because of this limitation, it is difficult to use data from a given run to resolve the detailed variation in regions where gradients are high, as for example in the region of transition from the inviscid to the viscous portions of the wake, or in the viscous wake itself. It is, of course, possible to shift the rake slightly from one run to the next and then combine the results from several runs. Unfortunately, in the case of the spark-heated tunnel the inherent lack of precise run-to-run repeatability precludes this method. The situation is worse when an axial variation is to be studied. In this case, since one cannot place impact tubes one behind another, only one data point can be obtained with each run, and poor repeatability then presents an even more formidable problem. In view of these difficulties, it was decided to extend the traversing-probe technique to cope with the short run time of the spark-heated tunnel.

To estimate the necessary probe speed, we note that for the probe to

9

complete a traverse of, say, 9 inches within the tunnel run time of 30 milliseconds, the minimum probe speed must be, ideally, 25 fps. In practice it is not possible to coordinate or time everything precisely, and a more realistic minimum is about 35 fps. Furthermore, it is desirable to make even faster traverses because the flow in a spark-heated tunnel decays with time. To complete the traverse in less than 10 milliseconds would require a speed of about 100 fps. Such speed is difficult, if not impossible, to attain with a motor-driven probe. One must resort instead to pneumatic systems or spring-driven devices.

For the present measurements of Pitot pressure, two spring-driven probes were designed and built, (1) a vertically traversing probe that gives transverse profiles across the wake, and (2) an axially traversing probe capable of surveying the longitudinal variation. These are described in the following sections.

2.4 Vertically Traversing Probe

General Description: The bulk of the results to be presented were obtained with the vertically traversing probe, shown mounted on the tunnel test section in the schematic drawing of Fig. 5. This probe uses one spring for providing the driving force and one for braking. The traversing portion of the probe, shown in Fig. 6, consists of a length of aluminum tubing and an aluminum shell, rigidly pin-mounted at one end that houses two wafer-type pressure transducers. The tube, in addition to being the driven shaft, also provides a protected passageway for the transducers' electrical and vacuum connections. A steel collar pin-mounted to the tube at about the half-way mark serves three functions: (1) it is the "catch" through which the action of the driver and braking springs is transmitted to the driven probe; (2) it serves as a guide for the entire traversing assembly to slide vertically inside the outer brass tube that encases the probe and the springs; and (3) its lower flat surface engages the locked cam when the probe is being cocked. A set-screw inserted in the collar slides in a vertical slot in the brass tube, thereby curbing rotation of the probe about its own axis. The brass tube is bolted onto a heavy base plate, on which is also mounted the support stand for the

10

trigger assembly. When installed in the tunnel, the bulk of the traversing-probe unit remains outside the tunnel, the only parts entering inside being the transducer-carrier housing and a portion of the aluminum guide tube. Since it is difficult to make the unit completely air-tight, a sheet-metal hood with an O-ring attached is placed over the unit during tunnel runs. The enclosure thus becomes a part of the tunnel vacuum chamber.

Driving Mechanism: The maximum design probe speed was set at 100 fps. In addition, the useful acceleration-free traverse of the probe was specified to be 8 inches.

To design a driver spring that will give these results, certain physical limitations had to be taken into account. For example, the spring was to be made from music wire, and the largest music wire that is available commercially has a diameter of 0.180 inches. Furthermore, at the location where the traversing-probe unit is installed, the tunnel inner diameter is 16 inches. If the probe is to have an acceleration-free traverse of 8 inches centered about the tunnel axis, the probe and the driver spring must complete their acceleration in the first 4 inches of motion. This implies that the initial compression of the spring should not appreciably exceed 4 inches.

The theory and formulas used to design the spring are the same as those already reported for the case of the axially traversing probe (see Alligood, Kyser, and Tsao, 1963) and will not be elaborated here. It will suffice to mention that the method is based on the surge-wave-theory approach of Maier, an account of which is given in Chironis (1961). The finished spring has a coil outer diameter of 1.25 inches and is 9.5 inches long when fully extended. It consists of 21 turns of 0.180-inch-diameter music wire, first coiled into form and then heat treated to increase the yield point of the steel. Without heat treatment, the wire will not be stiff enough to give probe speeds close to 100 fps.

After the spring s designed and built, the compression required to give a particular probe speed was found experimentally during bench testing. For all subsequent tunnel runs, the probe was operated at a speed of 60 fps, obtained with a spring compression of 5.5 inches. This

11

speed is short of the design value of 100 fps. This was primarily the result of the fact that the mass of the driven assembly came to exceed the design figure when it was found necessary to reinforce the cushioning and support details for the transducer wiring.

Loading the Probe: The probe is loaded by first engaging the steel collar to the locking cam and then compressing the spring by means of the threaded brass plunger (refer to Fig. 5). To prevent the spring from interfering with the probe after its release, the spring is welded onto the plunger. Thus, when the spring is being compressed, it tends to rotate with the plunger. Large bearing loads result between the spring and the collar, and it was found that of several commercially available ball bearings tested none could handle these loads. The difficulty was resolved through the use of a specially made, flat teflon ring bearing, sketched in Fig. 6.

Trigger Assembly: The mechanism for releasing the probe is illustrated in Fig. 7. The cam-and-sear combination is controlled by a Ledex 25° rotary solenoid with an axial stroke of 0.6 inches.

It is essential that the probe traverse be synchronized with the tunnel run. This is accomplished by integrating the switch closure (of the d. c. circuit) into the circuit for starting the tunnel. Through the use of an appropriate number of relays, one can control the timing to within 5 milliseconds.[*] It was found, however, that if the probe were left in the loaded position for a prolonged time before triggering, the various links and joints would stick slightly. The delay time between switch closure and probe release can thus increase by as much as 15 to 20 milliseconds, and even though the switch is closed at the specified instant relative to tunnel firing, the probe is released too late to complete its traverse within the tunnel run. Care was therefore taken to load the probe just before making the run. In addition, the solenoid-activating voltage was increased from the rated 50 volts to 90 volts to

---

[*] These remarks concerning the necessity of synchronization and the means of achieving it apply also in the case of the release of the sphere.

12

provide a higher force from the rotary arm. When these precautions were taken, it was possible to program the probe traverse into the tunnel running sequence to within the desired accuracy of 5 milliseconds.

Position Transducer: The position of the traversing probe relative to the tunnel is indicated by a combination of a light source and photocell. The physical arrangement is shown schematically in Fig. 8(a), and Fig. 8(b) is a diagram of the associated circuitry. An aluminum ring, attached to the brass tube near the base, holds the light and the photocell in diametrically opposed positions. Small holes (1/16-inch in diameter) are drilled at half-inch and one-inch intervals through the aluminum traversing tube. Snug-fitting lucite rods are inserted into these holes and glued in place.

The position transducer functions as follows: Whenever one of the lucite rods lines up with the idealized light path, the photocell senses the light directly. When the wall of the aluminum tubing is in the way, however, only reflected light reaches the photocell. The signal from the photocell therefore exhibits a series of spikes corresponding to the position of the lucite rods, and can be used as a position indicator. Figure 9(a) shows an oscillograph record of the photocell-circuit output. To establish the actual position correspondence of the individual spikes, one such spike must be calibrated by direct measurement. It is then possible to obtain a time-position plot from the oscillograph trace. An example is shown in Fig. 9(b), where it can be seen that the probe reaches its peak speed after the first 3 to 4 inches of travel. This speed of approximately 60 fps is maintained for the 8 inches of traverse, within which the data recorded by the pressure transducers are considered reliable.

Pressure Transducers and Associated Wiring: The probe carries two pressure transducers of the variable-reluctance wafer design originated at AEDC (see Smotherman, 1960). These are housed in the aluminum shell illustrated in Fig. 6, with the wafer plane vertical so as to minimize any effects that the probe's acceleration might have on the displacement of the transducer diaphragm. To obtain the fastest response possible with the transducers, their pressure-side inlets are used directly as Pitot-pressure orifices.

13

Electrical and reference-vacuum connections to the transducers must be routed through the aluminum tube. The size of the electric cables hence dictates not only their own weight but also the size and weight of the tube. It is therefore important to use the smallest cables available. The present choice was a Microdot coaxial cable with an outside diameter of 0.068 inches.

Some difficulties were encountered in finding adequate means of anchoring the cables to the shaft. It was thought at first that potting the entire transducer-carrier shell would enable the soldered joints to withstand the large impact loads that are involved during acceleration and braking. Potting alone was not sufficient, however, because the cabling that hangs outside the shaft has a tendency to whip about during the impulsive start and stop of the probe motion. The situation was finally remedied by clamping the cables to the shaft at the top, and in addition the potting was extended to include the lower portion of the shaft. The potting compound used is a General Electric RTV 102 adhesive. The compound proved to be an ideal potting medium because it sets into a rubbery substance that provides a firm cushioning support; at the same time it does not harden into a solid that easily cracks upon impact.

The pressure transducers were patterned after the initial design of Smotherman (1960). They are not immune to external forces, as is a later acceleration-compensated version of the same basic transducer. After several runs with the probe, it became apparent that the probe's random lateral vibrations during descent had a noticeable effect on the diaphragm deflection, as manifested by a low-frequency noise in the transducer output. The noise level could be as high as 5 to 10% of the actual pressure signal. To correct the output for this vibrational noise, the upper transducer was converted into an accelerometer as follows: A short length of tygon tubing, with the front end blocked by a thin metal disc, was slipped over the transducer intake. A tiny puncture is made in the wall of the tygon tube to permit the passage of air during static calibration. With this arrangement the upper transducer experiences no Pitot pressure during a tunnel run but does register the noise due to the lateral vibration. Assuming that the two transducers experience identical vibration

14

and that their sensitivity to acceleration forces is given by static calibration, one can then subtract the noise from the output of the lower transducer, leaving a clean pressure signal.

2.5 Axially Traversing Probe

A detailed account of the design, construction, and operation of the axially traversing probe has already been given by Alligood et al. (1963). The mechanical principles are similar to those of the vertically traversing probe and need not be elaborated upon here. An assembly drawing of the probe is given in Fig. 10. A photograph of the probe mounted in the tunnel is shown in Fig. 11 (the nozzle of the tunnel, including the test section, is rolled back to the left).

A redesigned Pitot-pressure rake has since replaced the one shown in the photograph. The details of the new rake are shown in Fig. 12. The spacing of the Pitot tubes has been modified to give an improved survey of the inner viscous wake. The size of the tubes has also been modified on the basis of the following considerations of low-Reynolds-number effects, data resolution, and structural strength. The parameter controlling the effect of low Reynolds numbers is the ratio of the inner to the outer diameter of the tube. The effects are minimized by maximizing this ratio, that is, by minimizing the wall thickness for a given outside diameter. To obtain good data resolution, it is desirable to use as small a tube as possible consistent with adequate strength from the structural standpoint. The Pitot tubes as finally selected have an outside diameter of 0.034 inches and a wall thickness of 0.002 inches.

2.6 Pressure Instrumentation

To calculate the flow conditions in the test region, measurements are needed of the time history of the arc-chamber pressure and the test-section Pitot pressure (see Section 2.7).

The arc-chamber pressure is measured by a bonded-strain-gage transducer fabricated at Stanford. The sensing element is basically a four-arm resistive Wheatstone bridge. The transducer has a range of 0-20,000 psig. It is calibrated periodically against a Heise gage that has a

15

range of 0-30,000 psig. Between such static calibrations, the linear behavior of the transducer is assumed to hold. The overall sensitivity of the amplifier-galvanometer system is checked from run to run, however. This is done by means of a standard resistor (in the amplifier circuit) that serves as an external calibrator.

The Pitot pressure in the test section, as well as in the wake flow, is measured with a two-arm variable-reluctance transducer with a range of 0-3 psi differential. Two types of gage are used: one is of the wafer design of AEDC but fabricated at Stanford, and the other is a heavier Hidyne unit. All Pitot-pressure transducers are calibrated statically before each run against manometers containing either mercury or oil of unit specific gravity.

The transducers are used in conjunction with 20-kilocycle carrier amplifiers (CEC Type 1-127). The output is recorded on a CEC Type 5-114 recording oscillograph. The recording galvanometers are flat to 1000 cps in the case of the arc-chamber pressure and to 120 cps or 185 cps (galvanometer option) in the case of the Pitot pressure.

The oscillograph is also used to record the photocell-circuit output after it has been amplified by a Sanborn 150-1300 d. c. amplifier. Other data outputs (viz., information pertaining to sphere release, etc.) are channeled directly to the oscillograph.

2.7 Test Conditions

The calculation of flow conditions in the test region is based on the work of Grabau, Humphrey, and Little (1961) and is performed on an electronic computer. The range of temperatures in which the calculations are valid has been extended with the incorporation of a nitrogen-properties subroutine due to Smith (1962).

The essential input information required for the calculations consists of the arc-chamber pressure and the stagnation pressure at the station where the flow conditions are desired. The arc-chamber pressure is readily obtained; the stagnation pressure at the nose of an unsupported sphere cannot be obtained experimentally, however. Furthermore, the test region is too small to accommodate a separate probe to monitor

16

equivalent information, i.e., the Pitot pressure in the free stream at the same longitudinal station. It is therefore necessary to use information taken from a separate calibration run in which the time history of the Pitot pressure is obtained with a stationary probe positioned in place of the sphere. It has been found that for a particular set of operating conditions, the ratio of arc-chamber pressure to test-section Pitot pressure is more repeatable than either pressure individually. Consequently instead of taking the Pitot pressure directly from the calibration run, we adopt the ratio of the two pressures for use in the sphere runs.

A consideration is now given of the variation of test conditions encountered in the experiments. The flow quantity that will be used as the primary parametric variable is the Reynolds number, $Re_{l_n,d}$, based on the diameter d of the sphere and on free-stream conditions at the nose. Three sets of operating conditions have been used to obtain three basic Reynolds numbers. Within each of the three sets of conditions, some variation in Reynolds number arises from the following causes: (1) the tunnel flow decays in time, and the Reynolds number decreases during a given probe traverse; (2) free-stream conditions at the nose of the sphere are different for different positions of the sphere since the tunnel stream expands along the nozzle; and (3) overall tunnel flow conditions vary somewhat from run to run because of lack of exact repeatability.

Typical flow conditions are summarized in Tables 2.1 and 2.2 at the end of this section. The results of Table 2.1 pertain to a fixed test station, the variable being the operating conditions. In contrast, the results of Table 2.2 reflect the variation in conditions caused by a shift of the test station. In both tables, the time for which the data are given is 20 milliseconds after the start of the tunnel run, which corresponds roughly to the middle of the run.

17

Table 2.1

Free-Stream Conditions at Station A

Total Temperature °K	Mach Number	Reynolds Number (based on d = 2")
3,730	16.0	2.18×10^{4}
2,370	17.7	7.40×10^{4}
1,450	16.2	1.77×10^{5}

Table 2.2

Variation of Free-Stream Conditions with Location of Test Station

Station	Total Temp. °K	Mach Number	Reynolds Number (based on d = 2")
A	1,270	16.31	2.35×10^5
B	1,270	16.16	2.40×10^5
C	1,270	16.00	2.46×10^5
D	1,270	15.84	2.52×105
E	1,270	15.68	2.58×10^5
F	1.270	15.51	2.64×10^5
G	1,270	15.35	2.70×10^5
H	1,270	15.03	2.81×10^5

3. TRANSDUCER-GALVANOMETER RESPONSE AND CORRECTION

3.1 Preliminary Remarks

When pressure instrumentation was first chosen for the Stanford spark-heated tunnel, it was decided that an oscillograph would be used for recording pressure information. The oscilloscope, despite its superior response and versatility in other respects, was passed over in deference to the oscillograph's capability of recording as many as 26 channels of data on a single time base. To use oscilloscopes to provide the equivalent capacity would not have been economically possible. Also, the task of operating the many oscilloscopes simultaneously during calibration or tunnel run would have been difficult. Furthermore, data reduction is easier and more accurate on the oscillograph. These factors all contributed towards the selection of the oscillograph as the basic instrument for recording pressure data.

3.2 Response Considerations

For the recording of routine arc-chamber pressure and of Pitot pressure in the test section (measured with a stationary probe), the choice of the oscillograph was satisfactory because the different types of galvanometer that were available turned out to be adequate for their respective assignments. For example, in the case of arc-chamber pressure, where good response is essential, one can use a relatively fast galvanometer (flat to 1000 cps). On the other hand, for the Pitot-pressure transducer, where a substantial level of high-frequency noise in the amplified output requires a slower galvanometer (flat to 125 or 180 cps), response is not of prime concern when only the test-section Pitot pressure is involved.[*]

When the traversing probes were introduced, the same combination of galvanometer and Pitot-pressure transducer was taken over. This led to a response problem that was recognized only after a substantial amount of

---

[*] This difference in response requirements stems from the fact that the time history of the arc-chamber pressure is the more critical of the two pressure inputs in the calculation of test-section flow conditions.

20

data had already been taken. The problem is particularly acute with the vertically traversing probe, because the probe speed is high and large gradients are present in the transverse Pitot-pressure profiles. For example, for the probe speed of 60 fps used and for an overall system response lag of — say — one millisecond, the entire profile would appear to be shifted off center by about eight-tenths of an inch. In addition, since large gradients are present in the profile, its shape would be distorted, and the pressure trace actually recorded would lose some of the symmetry normally to be expected in such a profile. In other applications, for instance the axially traversing probe, response requirements are not so exacting. The discussion that follows will pertain only to the vertically traversing probe.

When it became apparent that the response of the pressure-recording system was not fast enough for work with the vertically traversing probe, it was also recognized that it would be difficult to improve on the response by replacing components of the existing system with other readily available equipment. One possibility was to replace the galvanometer with an oscilloscope. This was not attempted, however, because previous experience showed that the amplifier output exhibited considerable high-frequency noise, and to obtain a clean pressure signal would have required that a low-pass filter be inserted ahead of the oscilloscope. From the response standpoint, the filter would then effectively reduce the oscilloscope to the level of a galvanometer, thereby defeating the purpose of using the oscilloscope in the first place.

Besides the slow response of the galvanometer, there is also the question of the response behavior of the transducer itself. The problem of transducer response has been studied by Smotherman and Maddox (1963), who determined the rise time for various configurations of the wafer transducer. This work is not directly applicable to the Stanford version of the basic AEDC design, however, since some differences exist in the dimensions and construction details, and these control the response characteristics of the transducer. Furthermore, Smotherman and Maddox did not study the response of the combined transducer-amplifier-galvanometer system, which is of interest here. It was decided therefore that a separate experimental study should be conducted to obtain the desired

21

information. When the response characteristics of the overall system were known, one could hope to devise an analytical correction scheme that could then be applied to the recorded pressure output.

The experimental determination of the system response characteristics is based on the theory of linear systems. It is therefore appropriate to introduce some of the fundamental concepts before proceeding to the results of the experimental study.

3.3 System Transfer Function

The transducer-galvanometer combination may be considered as a linear system provided an approximation is made regarding the transducer itself (see Appendix A). In what follows, the assumption of a linear system will be adopted throughout.

The response characteristics of the transducer-galvanometer system is specified if the system's transfer function is known. In the theory of linear systems, a transfer function $G(s)$ is defined (see, for example, Clark, 1962) as the ratio of the Laplace transform of the output to the Laplace transform of the input, i.e.,

$$G(s) \equiv \frac{P_{out}(s)}{P_{in}(s)} = \frac{\mathcal{L}\{p_{out}(t)\}}{\mathcal{L}\{p_{in}(t)\}} \quad , \tag{3.1}$$

where s is the Laplace variable, and $p_{in}(t)$ and $p_{out}(t)$ are respectively the input and output to the system, as shown in Fig. 13(a). In the present case, $p_{in}(t)$ and $p_{out}(t)$ refer specifically to the pressure input and output. When the transfer function is known, the system output to a specific input is then given by

$$p_{out}(t) = \mathcal{L}^{-1}\{G(s) \cdot P_{in}(s)\} \tag{3.2}$$

A convenient way of obtaining the transfer function is to consider the response of the system to a unit step-input (whose Laplace transform is $1/s$), the output in this case being known as the "transient response".

22

If the Laplace transform of the transient response is denoted by $X(s)$, then from Eq. (3.1) the transfer function is simply $s[X(s)]$. This relationship in fact provides a means for experimental determination of the transfer function. That is, one can impose a step function on the system and record the corresponding output; the output can then be compared with theoretically calculated transient-response curves (given in standard textbooks on automatic control systems) to yield the appropriate function for $X(s)$, which in turn gives the transfer function. This procedure is not difficult if the order of the system is known. For a system of components in series, an alternative approach is to find the transfer function for each component; the overall transfer function is then simply the product of the individual transfer functions (see Clark, 1962, p. 30).

To find the transfer function for the transducer-galvanometer system, the experimental approach was used. Briefly, a step increase in pressure of known magnitude was generated at one end of a simple shock tube by means of shock-wave reflection. The transducer positioned at this end thus experienced a step input of pressure. The transducer output and galvanometer output were then used to find the transfer function of the system components. The experimental details and the intermediate steps used in arriving at the composite transfer function $G(s)$ for the transducer-galvanometer system are outlined in Appendix A. The final result for $G(s)$ was found to be

$$G(s) = \frac{k\omega_n^2}{\delta} \frac{1 - e^{-s\delta}}{s(s^2 + 2\omega_n \zeta s + \omega_n^2)} \quad , \tag{3.3}$$

where ω_n = undamped natural frequency of galvanometer,

ζ = damping ratio of galvanometer,

k = correction factor to transducer, and

δ = approximate rise time of transducer.

The values of the system parametric constants ω_n, ζ, k, and δ are also given in Appendix B.

23

The determination of the transfer function defines the response characteristics of the transducer-galvanometer system. It does not, however, provide directly a means for calculating the system response to a pressure input of arbitrary shape, such as that encountered in the wake. This follows from the fact that in general an arbitrarily varying time function cannot be expressed analytically, and its Laplace transform – if it exists at all – cannot be calculated in closed form. The problem of finding the output to an input of arbitrary shape has an approximate solution, however, provided a sampling process is introduced at the input and at the output. We shall first show that the data-reduction procedure in the present case does introduce a fictitious data-sampling process. The resulting problem is then amenable to treatment by the theory of sampled-data control systems. One of the basic mathematical devices of this theory, the z-transform, is introduced in Section 3.5, which also gives an account of the application of the theory to the present case of the pressure-recording system. After we have established the procedure for calculating the sampled output from the input and the transfer function, we then consider the inverse problem of deducing the input when the output is given. The solution is based on a method of successive approximations and is presented in Section 3.6.

3.4 Analog in Sampled-Data Theory

In the data-reduction scheme, output-pressure information is obtained by reading deflections off the oscillograph record at regular time intervals, typically of one-half millisecond for runs with the vertically traversing probe. This procedure may be likened to sampling the pressure output by inserting after the galvanometer a switch that closes momentarily every T seconds, T being the sampling period. An equivalent sampling process would be to block the galvanometer light beam from the photo-recording paper at all times except for a flash every T seconds. This analogy with a sampled-data system is illustrated in Fig. 13. (For the fundamentals of sampled-data theory, see Kuo, 1963, or Ragazzini and Franklin, 1958.) The physical transducer-galvanometer system, whose block diagram was shown in Fig. 13(a), is a system for continuous signals.

24

The switch that simulates the sampling process, the so-called "ideal sampler", is depicted in Fig. 13(b) together with a graphical representation of its sampling function in the form of a unit-impulse train. The block diagram for the analogous sampled-data system is shown in Fig. 13(c). (The function of the "hold circuit" placed ahead of the pressure transducer will be explained in the next section.)

We note that in addition to the insertion of a sampler switch at the output in Fig. 13(c) — which is the appropriate representation of the process of reading off discrete values — a similar switch is inserted at the input as well. This input sampler is introduced to complete the analogy, since in a sampled-data system the presence of this sampler is mandatory. This is because the fundamental problem in sampled-data theory is to find the appropriate manner of sampling the input so that one needs to feed to the system only the sampled sequence instead of the continuous input while still being able to extract approximately the same information at the output. Thus in a sampled-data system the input sampler is the essential switch; the synchronous switch at the output is inserted simply to facilitate the analysis. In the analog for the transducer-galvanometer system, on the other hand, the output switch is the more meaningful one because it is at the output that discrete values are read off; the input sampler is included so that we may draw an exact analogy with the sampled-data problem and use the available results from the theory. With the introduction of the fictitious sampler into the transducer-galvanometer system, however, the question arises as to whether the sequence of input sampled by the switch is an accurate representation of the continuous input at the sampling instants. Thus, after the analogy has been drawn, the subsequent problem is twofold: (1) to find the appropriate sampling procedure for the transducer-galvanometer system, and (2) to show that for this system there is indeed a correspondence between the sampled input and the continuous input.

To find the appropriate sampling procedure in the present instance, use was made of the test case involving the transient response of the system.[*]

---

[*] This test case has been considered in the last section, Eq. (3.3) and the paragraph preceding it.

Since the transient response was determined experimentally, it was possible to choose the sampling procedure that gave the best agreement with experimental results, and this will be discussed in the next section. To show that there is correspondence between the sampled input and the continuous input (the second part of the problem), the following plausibility argument is used. In sampled-data theory, the sampled-sequence representation of the input is by definition exact, irrespective of the sampling procedure. The basic tenet of the theory states that with the proper choice of a sampling process, the sampled-output information then accurately represents the continuous output. Now, in the analogous case for the transducer-galvanometer system, the roles of input and output are interchanged. At the output the sampled sequence is known to correspond to the continuous signal, since the sampling describes in actuality the process of reading discrete values off a continuous trace on the oscillograph record. Now, by virtue of part (1) in the foregoing, it can be assumed that the appropriate sampling procedure is used. We thus infer, by an application in reverse of the basic tenet of sampled-data theory, that the sampled input does represent adequately the continuous input at the particular sampling instants.

3.5 The z-Transform Method

In the theory of sampled-data control systems, the basic mathematical tool is the z-transform. The z-transform is actually a shorthand notation for the reciprocal of the Laplace transform of a unit impulse occurring at $t = T$, that is,

$$\mathcal{L}\left\{\delta(t-T)\right\} = e^{-Ts} \equiv z^{-1} \quad . \tag{3.4}$$

Similarly, the Laplace transform of the unit-impulse train of Fig. 13(b), which is basic to the data-sampling process, is expressible in terms of a polynomial in z^{-1} as follows:

$$\mathcal{L}\left\{\sum_{n=0}^{\infty} \delta(t-nT)\right\} = \sum_{n=0}^{\infty} e^{-nTs} = \sum_{n=0}^{\infty} z^{-n} \quad . \tag{3.5}$$

26

Since a sampled sequence (with sampling period T) of any function $f(t)$ can be represented by $\sum\limits_{n=0}^{\infty} f(nT)[\delta(t-nT)]$, it follows from Eq. (3.5) that the Laplace transform of the sampled input can be expressed as

$$\mathcal{L}\{\sum_{n=0}^{\infty} p_{in}(nT)\delta(t-nT)\} = \sum_{n=0}^{\infty} p_{in}(nT)z^{-n} \equiv P_{in}(z) \ . \qquad (3.6)$$

The corresponding expression for the sampled output is

$$P_{out}(z) = \sum_{n=0}^{\infty} p_{out}(nT)z^{-n} \ . \qquad (3.7)$$

It is shown in standard texts on sampled-data systems that the functional relationship between $P_{in}(z)$ and $P_{out}(z)$ is completely analogous to the corresponding case of Eq. (3.1) for continuous signals. Thus, for sampled-data systems the relationship is

$$P_{out}(z) = G(z) P_{in}(z) \ , \qquad (3.8)$$

where $G(z)$, the z-transform of the transfer function, is evaluated according to the formula (see Ragazzini and Franklin, 1958, p. 57)

$$G(z) = \sum_{\substack{poles\ of \\ G(s)}} residue \left[G(s) \frac{1}{1-e^{Ts}z^{-1}} \right] \ . \qquad (3.9)$$

The function $G(z)$ is normally expressed in terms of the quotient of two polynomials in z^{-1}. Further simplification is possible by long division to yield a single polynomial in z^{-1}.

Ideally, Eq. (3.8) used in conjunction with Eqs. (3.6) and (3.7) for $P_{in}(z)$ and $P_{out}(z)$ gives a method for calculating $P_{out}(z)$ when $G(z)$ and $P_{in}(z)$ are given (by equating coefficients of like powers in

27

z^{-1}). However, if the sampled input were fed directly into the linear system, some of the original information between sampling instants would be lost, resulting in an inaccurate output. It is therefore necessary to use some form of interpolation scheme to supply additional information between the sampling instants. This is done by the fictitious hold circuit, or "data hold", inserted between the input sampler and the transducer (refer to Fig. 13(c)). The function of the hold circuit is to reconstruct the sampled-input sequence and transform it into a piecewise continuous or piecewise smooth data curve before feeding the information into the linear system. Interpolators of various orders can be used, depending on the accuracy desired and on the shape of the particular data curve under consideration. A detailed discussion of the subject of hold circuits is given by Jury (1964).

In the present instance, the most suitable hold circuit is a first-order interpolator having the transfer function (see Jury, 1964, p. 222)

$$Q(z,s) = \frac{z(1-z^{-1})^2}{Ts^2} \ .$$ (3.10)

Because this transfer function contains the Laplace variable s, the function must be included in the right-hand side of Eq. (3.9) before the z-transform of the overall transfer function can be evaluated. For clarity, the overall transfer function that includes the first-order interpolator is denoted by $\tilde{G}(z,s)$, that is,

$$\tilde{G}(z,s) = Q(z,s) \ G(s) \ ,$$ (3.11)

where $G(s)$ for the transducer-galvanometer system is given by Eq. (3.3). The algebraic details of evaluating $\tilde{G}(z)$, the z-transform of $\tilde{G}(z,s)$, from Eq. (3.9) are outlined in Appendix B. The final result is

$$\tilde{G}(z) = \frac{k}{\lambda \bar{\bar{T}} \bar{\delta}} \ \frac{m_{-1}z + m_0 + m_1 z^{-1} + m_2 z^{-2}}{1 + d_1 z^{-1} + d_2 z^{-2}} \ ,$$ (3.12a)

28

$$\text{or,} \quad \tilde{G}(z) = r_{-1}z + r_0 + r_1 z^{-1} + r_2 z^{-2} + \cdots, \qquad (3.12b)$$

where $\bar{T} = \omega_n T$, $\bar{\delta} = \omega_n \delta$, and λ, m_{-1}, m_0, m_1, m_2, d_1, d_2 are all non-dimensional functions of the system parameters. The series representation of $\tilde{G}(z)$ in Eq. (3.12b), found by straightforward division from Eq. (3.12a), is in a form convenient for later use. The coefficients r_{-1}, r_0, r_1, $r_2, \ldots$ have been calculated with an electronic computer and are listed in Appendix B. An inspection of the magnitudes suggests that the series is convergent.

In the analogy of the transducer-galvanometer system with a sampled-data system, we have assumed that a suitable sampling rate has been used. Furthermore, no immediate justification was given for choosing an inter-polator of a particular order as the appropriate data hold. These two aspects of the problem are interrelated, and several combinations of sampling period and interpolator were tested to establish the most sat-isfactory combination. The criterion used to gage the relative success of a particular combination was to determine how closely the calculated sampled output matches the experimentally recorded output corresponding to the unit-step pressure input generated by shock-wave reflection. Interpolators of zeroth, first, and second order were tried and the sampling period was varied from 0.1 to 0.5 milliseconds. The best results were obtained with the first-order interpolar of Eq. (3.10) and a sampling period of 0.25 milliseconds. Now, in the reduction procedure for wake runs (discussed in Chapter 5), the time interval between data read-outs was 0.5 milliseconds. To use the foregoing results with a sampling period of 0.25 milliseconds, additional data had to be obtained at points midway between any two adjacent data-readout instants. This additional information was obtained by interpolating the 0.5-millisecond data. The interpolation was carried out with Lagrange's interpolation coefficients (see Henrici, 1964, pp. 183-185); either a three-point or a four-point formula was used, depending on the portion of the output trace considered.

29

3.6 The Indirect Correction Scheme

With the inclusion of the data hold in the overall transfer function, Eq. (3.8) must now be modified to read[*]

$$P_{out}(z) = \tilde{G}(z) \, P_{in}(z) \quad . \tag{3.13}$$

The problem at hand is to find $P_{in}(z)$ when $P_{out}(z)$ and $\tilde{G}(z)$ are given. Conceptually, one is therefore inclined to seek an inverse of the transfer function so as to calculate $P_{in}(z)$ directly from $P_{out}(z)$ according to

$$P_{in}(z) = \tilde{G}^{-1}(z) \cdot P_{out}(z) \quad . \tag{3.14}$$

An examination of $\tilde{G}(z)$ reveals, however, that the inverted function, if evaluated exactly, will be unbounded at $t = 0$. The use of Eq. (3.14) would then lead to anomalous results.

To understand the behavior of $\tilde{G}^{-1}(z)$ about $t = 0$, consider the physical interpretation of the series representation of $\tilde{G}(z)$ in Eq. (3.12b). The response lag in the transducer-galvanometer system is due mainly to the galvanometer, which is a second-order system. The output from the galvanometer corresponding to a step-input thus approximates that calculated for a second-order system; namely, at $t = 0$ the output curve has zero deflection as well as zero slope (see Fig. 14). For zero deflection, the coefficient of z^0 in $P_{out}(z)$ must vanish. It follows from Eq. (3.13) that ideally the coefficient r_0 in Eq. (3.12b) would be zero as well. In this ideal case, it is easy to see that the inverse transfer function $\tilde{G}^{-1}(z)$ would indeed be unbounded at $t = 0$. In actuality the coefficient r_0 is small but not zero, owing to the slight distortion of information inherent in the data-sampling and

---

[*] The function $\tilde{G}(z)$ in the present study involves the first-order interpolator $Q(z,s)$ of Eq. (3.10). In general, however, $\tilde{G}(z)$ may involve a data hold of any order.

30

reconstruction process.[*] The behavior of the inverse function is never-
theless unstable about $t = 0$, and this instability in turn infects the
entire series.

An inversion of $\widetilde{G}(z)$ was in fact attempted by first taking the
reciprocal of the right-hand side of Eq. (3.12a) and then dividing to
obtain a series in z^{-1}. The series thus obtained is divergent, however,
as contrasted with the convergent series for $\widetilde{G}(z)$ of Eq. (3.12b). The
divergence of the series for $\widetilde{G}^{-1}(z)$ is an indication of the instability
of the inverse function.

With the failure of the direct calculation of $P_{in}(z)$ according to
Eq. (3.13), an iterative scheme was devised by which $P_{in}(z)$ can be
calculated indirectly from Eq. (3.13) through a series of successive
approximations. Briefly, an initial guess is made for $P_{in}(z)$, say
$P_{in}^{(0)}(z)$, and the output $P_{out}^{(0)}(z)$ corresponding to this guessed input
is found from Eq. (3.13). By comparing $P_{out}^{(0)}(z)$ with the actual output
$P_{out}(z)$, it is possible to derive a correction term that provides an
improvement on $P_{in}^{(0)}(z)$. This forms the basis for an iterative procedure
that can be repeated until the desired accuracy is obtained.

The derivation of the correction scheme is lengthy; the details are
given in Appendix C. In brief, by considering the magnitude of the
coefficients r_i of $\widetilde{G}(z)$ together with the functional relationship of
Eq. (3.13), it can be shown that an improvement on the ith approximation
to $P_{in}(z)$ at $t = nT$, for $n \geq 3$, is given by

$$P_{in,n}^{(i+1)} = P_{in,n}^{(i)} + \frac{P_{out,n+3} - P_{out,n+3}^{(i)}}{\sum\limits_{j=0}^{6} r_j} , \qquad (3.15)$$

---

[*] The inclusion of a first-order interpolator introduces some incon-
sistency in $\widetilde{G}(z)$ about $t = 0$. Since the interpolator operates on
adjacent data points, at $t = 0$ it interpolates the point $t = -T$ as
well. This results in the physically unrealistic term of $r_{-1}z^{+1}$ in
$\widetilde{G}(z)$ in addition to ascribing a nonzero value to r_0.

where $P_{out}^{(i)}(z)$ is the output calculated from $P_{in}^{(i)}(z)$ with the use of Eq. (3.13). For $n = 0,1,2$ the corresponding expressions are slightly different and are given in Appendix C. Convergence of the correction scheme is not particularly rapid, since it is based primarily on a linear analysis. The iteration procedure is simple, however, and as many as 5 to 15 iterations can be performed rapidly on an electronic computer.

To test the accuracy of the foregoing correction scheme, it was applied to a case in which both the input and the output sequences are constructed and are therefore known sequences. This verification procedure consists of the following steps: (1) construct a sequence of input data points that simulates the type of Pitot-pressure data that one might expect to obtain in the experiments; (2) calculate the corresponding output according to Eq. (3.13); and (3) apply the correction scheme to this output in an attempt to recover the constructed input.

The constructed sequences of input and output data from steps (1) and (2) are shown in Fig. 15. Even though the data as used in the actual calculation are discrete points at the sampling instants, they are nevertheless shown in this figure as piecewise continuous curves. This is done to improve visual representation. The input curve is made up of three segments, corresponding to an idealized representation of the Pitot-pressure variation in the three distinct flow regions traversed by the probe in going from the tunnel wall to the wake axis. The first region is the tunnel boundary layer, in which the Pitot pressure increases linearly.* Upon crossing the bow shock wave into the inviscid portion of the wake, the Pitot pressure undergoes an initial jump, after which the pressure decreases, rapidly at first but flattening out gradually as the viscous wake is approached; a parabolic segment is used to represent this variation. In the third region, the viscous wake, the Pitot pressure

---

* In the case where the bow shock wave intersects the tunnel boundary layer downstream of the probing station, there is a region between the boundary layer and the shock wave in which the Pitot pressure is constant. This region need not be represented separately, however, since a line denoting constant pressure is essentially the same as the line representing the linear pressure increase in the boundary layer.

32

is taken to be given by a second parabolic segment whose minimum corresponds to the axis of the wake. The calculated output corresponding to this input exhibits the essential features of the measured Pitot-pressure profiles (see Chapter 5 for comparison).

In the application of the correction scheme, the initial, guessed input (shown as a dashed curve) was taken to be essentially the output curve shifted backwards in time by an appropriate amount. A modification was provided at the jump discontinuity by using a backwards linear extrapolation. The corresponding input data as finally reconstructed are shown in the figure as discrete points. (To avoid crowding the figure, we have plotted the input at intervals of $4T$ only.) From a comparison of the reconstructed input with the original input, we observe that there is good agreement between the two sets of data.

A discussion of the application of the correction scheme to the measured Pitot-pressure profiles is deferred to Chapter 5, when the overall data-reduction procedure is described.

4. SOURCE-FLOW EFFECTS AND CORRECTION

4.1 Consequence of Free-Stream Nonuniformities

The Stanford spark-heated tunnel has a conical nozzle that includes a portion nominally used and designated as the test section (see Fig. 2). For the present experiments, however, the actual test region includes this test section together with a considerable portion of the nozzle upstream (see Section 2.1 and Fig. 3). In what follows it is therefore appropriate to use the term "nozzle" to denote the entire test region.

The undisturbed stream in the nozzle is nonuniform in two respects. The flow through the nozzle, starting from the tunnel throat, approximates that from a three-dimensional point source. Thus none of the streamlines are parallel to one another, and the flow has transverse nonuniformity. The second aspect of the nonuniformity is actually a consequence of the first, though it is useful to consider it separately. As the gas flows through the diverging nozzle it expands, resulting in longitudinal gradients in the various flow quantities.[*]

When a model is placed in such a nonuniform stream, the flow field around it differs from that for the same body immersed in a uniform stream. Mathematically speaking, the difference (for supersonic flow) stems from the different upstream boundary conditions for the two cases. Since for most flow fields there is a shock wave emanating from the nose of the model, this difference in the upstream boundary condition can be accounted for at the upstream side of the shock wave. The flow field around the model accomodates this different set of upstream boundary conditions by making suitable adjustments in the shape of the shock wave, with the result that the shape of the shock wave in source flow differs from that in uniform flow for the same model. It is useful to bear in

---

[*] An exception to this statement is found in the velocity. In a hypervelocity tunnel, the speed of flow approaches the highest attainable value of $V_1 = (2h_{t_1})^{\frac{1}{2}}$ early in the expansion process and does not increase appreciably thereafter. Thus it is permissible to assume, for the sake of ease of computation and analysis, that the undisturbed stream velocity is constant in the test region under consideration.

34

mind that once this change in shock-wave shape has been taken into consideration, it will be incorrect to consider in addition that the downstream flow field is also expanding locally within a diverging nozzle. The reason is that the boundary pertinent to the downstream flow field is the enveloping bow shock wave and not the nozzle wall (or strictly speaking the edge of the boundary layer that exists along the nozzle wall), and the effects of the source flow associated with the diverging nozzle have already been accounted for in the shape adjustment of the shock wave. The situation changes, however, after the shock wave intersects the nozzle boundary layer. In this situation, the flow in the region bounded by the reflected shock wave and the edge of the boundary layer is directly affected by the diverging geometry of the edge of the boundary layer.

In the present experiments, the wake Pitot pressure is among the flow quantities affected by the tunnel source flow. To use the pressure data for comparison with any theoretical results worked out for the case of uniform flow, the data first must be corrected for source-flow effects. Such correction would also be important if the data were to be applied to examples of actual flight, for which a uniform atmosphere prevails. We shall consider the effects only insofar as they change the shape of the shock wave and not after interaction between shock wave and boundary layer has occurred. In the following sections, we discuss the analytical basis for approximate schemes used to correct the measured Pitot pressure for source-flow effects.

+.2 Tunnel Source Flow

Before proceeding to the main portion of the analysis, it is appropriate to consider the nature and magnitude of the source flow in the Stanford tunnel.

The flow in the tunnel may be regarded as consisting of an inviscid core flow and a thick hypersonic boundary layer on the tunnel wall. If the thickness of the boundary layer along the nozzle is a constant fraction of the local nozzle radius, then the edge of the boundary layer will form a cone within the nozzle cone, the apexes of both cones being at the

throat of the nozzle.[*] In this case, the inviscid flow will be that due
to a point source situated at the throat. Theoretical results supported
by experiment show, however, that the edge of the boundary layer is not
a conical surface. The boundary layer thus has a contouring effect on
the inviscid flow, and the magnitude of the local source-flow effect is
different from that associated with the ia ⊥ case of a point source
positioned at the throat. We shall present a comparison of theory with
experiment, after which the magnitude of the local source-flow effects
will be assessed.

The problem of boundary-layer development in a hypersonic nozzle has
been studied analytically by Rasmussen and Karamcheti (1966). Results
from this work (Fig. 6) can be used to deduce the variation of the area
ratic A_E/A with the longitudinal distance L along the nozzle. Here
A_E is the effective area of the inviscid flow, A is the tunnel cross-
sectional area, and L is measured from the throat. When the variation
of the area ratio A_E/A is known, it is possible to calculate the
variation of other flow quantities. For example, to find the ratio of
the Pitot pressure at any two points along the length of the nozzle, one
starts by writing the Pitot pressure p_o' as

$$p_o' = f(\rho,T,V)\rho V^2 \quad . \tag{4.1}$$

In this equation the function $f(\rho,T,V)$ is essentially a constant for a
wide range of conditions when the Mach number is high. Furthermore, the
velocity may be assumed to be constant along the length of the nozzle
under consideration (see footnote on p. 34). Making use of mass conser-
vation, we then have, for two points a and b,

---

[*] This is an idealization based on the fact that the throat diameter is
very small relative to the other dimensions of the conical nozzle.

36

$$\frac{(p'_o)_b}{(p'_o)_a} = \frac{\rho_b V_b^2}{\rho_a V_a^2} = \frac{(\rho A_E V)_b}{(\rho A_E V)_a} \frac{V_b}{V_a} \frac{(A.)_a}{(A_E)_b}$$

$$(4.2)$$

$$= \frac{(A_E)_a}{(A_E)_b} = \frac{(A_E/A)_a}{(A_E/A)_b} \frac{A_a}{A_b} \quad ,$$

where A_a/A_b is calculated directly from the nozzle geometry.

It is now possible to compare the theoretical results with experimental data and this is done in Fig. 16. Two theoretical curves are shown. The solid curve is a plot of Eq. (4.2) in which the ratio A_E/A, deduced from the theory of Rasmussen and Karamcheti, varies from 0.416 to 0.475. The second theoretical curve (dashed line) is based on the assumption that the Pitot pressure varies inversely as the tunnel area A instead of the effective area A_E. This is equivalent to saying that in Eq. (4.2) the ratio A_E/A is taken to be constant, that is, that the edge of the boundary layer forms a conical surface with apex at the nozzle throat. The difference between the two set of results indicates that the inviscid flow in the tunnel as predicted by the theory of Rasmussen and Karamcheti is different from that in the ideal case of a source situated at the nozzle throat. Also shown in Fig. 16 are experimental points deduced from data obtained in a single run with the axially traversing probe. The good agreement between the experimental results and the theory of Rasmussen and Karamcheti verifies the earlier statement that the boundary layer has a contouring effect on the inviscid flow. Admittedly the range in which the theory is substantiated by the data is somewhat limited, owing to the relatively short traverse (9 inches) of the probe. In view of the close agreement, however, we shall adopt the results of Rasmussen and Karamcheti for present purposes.

The Pitot-pressure correction scheme worked out in later sections (Sections 4.5 and 4.6) is based on theory that pertains to a simple source flow. To render the theory applicable to the present situation where the stream is not a simple source flow, the following approximation is made in regard to the stream nonuniformity. It is assumed that the local

37

nonuniform stream can be replaced by a virtual source that gives at the station of interest the same longitudinal flow gradients as those calculated from the theory of Rasmussen and Karamcheti (see Fig. 17(a) for illustration). A characteristic length associated with this virtual source is L_o, the distance from the origin of the source to the nose of the model, that is, to the station of interest. This length is used to define a "source-flow parameter" r_b/L_o, where r_b is a characteristic dimension of the model, here taken to be the radius of the sphere. The source-flow parameter gives a measure of the seriousness of the source-flow effects on the flow field around the model.

The problem is now to find a relation that expresses L_o in terms of the longitudinal gradients. With this relation, one can then use the results of Rasmussen and Karamcheti to find the variation of L_o with the axial distance L from the nozzle throat. To derive the required relation, consider the sketch shown in Fig. 17(b). The two points a and b within the virtual source flow are situated at distances L_o and $(L_o + \Delta L_o)$ from the origin of the virtual source. From Eq. (4.2), we have[*]

$$\frac{(p_o')_b}{(p_o')_a} = \frac{A_a}{A_b} = \left(\frac{L_o + \Delta L_o}{L_o}\right)^{-2} \quad , \tag{4.3}$$

which leads to

$$1 + \frac{\Delta p_o'}{(p_o')_a} = \left(1 + \frac{\Delta L_o}{L_o}\right)^{-2} = (1 + \frac{\Delta L}{L_o})^{-2} \quad . \tag{4.4}$$

In the limit as b approaches a, Eq. (4.4) reduces to the required relation

---

[*] Since Eq. (4.2) dealt with the tunnel stream, the appropriate area to use was the effective area. In the case of the virtual source flow, however, it is not necessary to use the "effective" subscript.

$$L_o = -2 \frac{(p'_o)_a}{(dp'_o/dL)_a} \quad . \tag{4.5}$$

The quantity $(dp'_o/dL)_a$ is evaluated graphically from the Pitot-pressure
curve deduced from the results of Rasmussen and Karamcheti and shown in
Fig. 16. The variation of L_o thus calculated is given in Fig. 18 as a
function of L. Shown for comparison is the straight-line relationship
$L_o = L$ that would prevail if the edge of the boundary layer were a conical
surface with apex at the throat. It can be seen that the distance (L_o-L)
varies from 20 inches at $L = 80$ inches to 32 inches at $L = 110$ inches.
Thus the origin of the virtual source is at a distance of 20 to 32 inches
from the throat. Considered in terms of the overall values of L_o
involved (100 to 140 inches), this gradual shift of 12 inches is a rela-
tively minor change. Thus the approach used here of representing the
local nonuniform stream by an idealized point source appears to be rea-
sonable.

The description of the source flow is now complete. In the next
section a discussion is given of the available solutions to problems of
flow around objects placed in a source flow. We then turn to the specific
problem of source-flow effects on wakes and begin with a general descrip-
tion of the wake behind a sphere. Particular emphasis is placed on showing
that some of the available source-flow solutions can be applied to the
wake problem. The theory of the correction scheme for wake flow is then
treated in Sections 4.5 and 4.6.

4.3 Available Source-Flow Solutions

Source-flow effects were recognized to be significant only after a
considerable number of hypervelocity tunnels had been put into operation.
It was then found that substantial errors could result from the conduct
of tests in a diverging stream. This realization stimulated a consid-
erable amount of analytical work aimed at finding ways for correcting the
experimental data.

The first published work on source-flow effects is due to Baradell
and Bertram (1960). They use the method of characteristics to calculate

39

the flow field about a blunted flat plate in the flow from a point source. The solution for the nose region is an approximation, since the body surface here is replaced by a so-called "sonic wedge". Several other studies make use of simple Newtonian theory to estimate the effects on the surface pressure on slender bodies. This is done by Burke and Bird (1962) and Whitfield and Norfleet (1962) for wedges and cones, and by Hall (1963), who includes the Busemann centrifugal term for flow over curved surfaces. The work of Hall, in particular, extends the application of the simple Newtonian-flow model to generalized free-stream nonuniformities. Hall also treats the problem of a blunted slender body (typically a hemisphere-cylinder combination) by performing a perturbation analysis on a flow model based on the detached-shock-wave theory of Cheng (1960). The source-flow perturbations of the shock-wave location and surface pressure are thereby estimated.

A different approach is used by Berndt (1962), who adopts the constant-density approximation to estimate the effect on the shock-wave stand-off distance and the stagnation-point velocity gradient for a blunt nose. Following a suggestion by Berndt, Meyer (1963) used the blast-wave analogy to treat the problem of a hemisphere-cylinder model in the flow from a point source.

More recently, Savage (1966) has used the Newtonian successive-approximation scheme of Cole (1957) to calculate the effect on the flow field about a slender cone. This method of solution represents a more systematic approach to the problem than does the straightforward perturbation method based on the simple Newtonian-flow model. The results of Savage, worked out to second order in the Newtonian expansion, are not significantly different, however, from those of Whitfield and Norfleet, and of Hall.

As regards numerical solutions, in addition to the early work of Baradell and Bertram, there are two recent studies by Eaves and Lewis (1965) and Inouye (1966a). Eaves and Lewis consider a hemisphere-cylinder model in which source-flow effects are included in the method-of-characteristics calculations but neglected in the solution for the subsonic-transonic flow in the nose region. That is, the blunt-body solution is for a uniform parallel flow, whereas in the supersonic portion of the

40

flow field the upstream boundary condition at the shock wave corresponds to the case of nonuniformities resulting from a point source. Also included in this analysis are viscous effects over the model and their interaction with the inviscid flow field. The work of Inouye, on the other hand, treats exclusively the inviscid problem. The solution is exact in that source-flow effects are accounted for in both the subsonic-transonic region and the supersonic region. The solution for these regions is based respectively on the blunt-body solution of Van Dyke (1958) and on the method of characteristics. The model configurations considered include a spherical nose, ellipsoidal nose, spherically blunted cone, and, of particular interest to the present investigation, a hemispherical nose with a cylindrical afterbody.

To see which of the aforementioned solutions are applicable to the current problem of source-flow correction we first review briefly the general character of the wake behind a sphere. This is done in the next section, which also gives a preliminary discussion of how the pertinent solutions will be used.
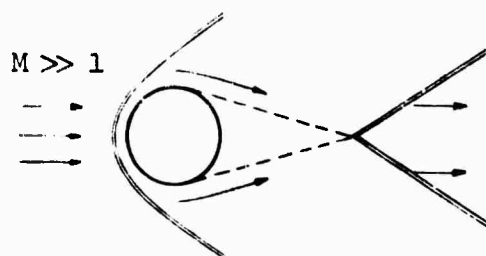
4.4 The Wake Behind a Sphere

For the present study, we are not concerned directly with the near-wake region upstream of the wake neck. The near wake will be considered only in terms of its gross effect on the wake downstream; the complicated structure of the recirculation zone will be ignored for the most part. The remainder of the wake (downstream of the neck) is assumed to consist of two distinct regions, the outer inviscid wake and the inner viscous wake (see Fig. 1).

The flow in the outer inviscid region consists primarily of the familiar entropy layer and shock layer. The overall picture of the inviscid wake behind the sphere is comparable to the aft portion of the flow field around a hemisphere-cylinder model. This similarity is based on the following considerations:

(1) The inviscid flow field around a blunt-nosed body is dominated by the bow shock wave, which in turn is dictated by the shape of the nose. The sphere and the hemisphere-cylinder have identical nose shapes.

41

(2) Even if the two flow fields are not the same in every detail, the overall picture of the inviscid flow is affected only slightly by the differences. To illustrate this, we construct an inviscid flow field for the sphere in which the supersonic stream comes together at the rear (see accompanying sketch[*]). By construction the space that is taken up by the cylindrical afterbody in the case of the hemisphere-cylinder is now occupied by fluid; the two flow fields are therefore somewhat different. This difference does not significantly affect the rest of the inviscid flow field, however. This is because the fluid near the longitudinal axis, being part of the entropy layer, is of low density. In addition, the volume difference that is under consideration is relatively small. Thus the details of the afterbody geometry do not play a crucial role in determining the overall inviscid flow field. In the actual flow behind the sphere the existence of the viscous wake modifies the above picture in any case. The viscous wake may be thought of in a sense as replacing the cylindrical afterbody. The amount of fluid that flows through the viscous wake is small, however, and the inviscid wakes may still be considered similar to each other.

(3) Insofar as the inviscid wake is concerned, the recompression shock wave emanating from the neck region has been shown by Feldman (1961) to have negligible effect and will be disregarded in the analysis to follow. Here again the equivalence of the two wakes is substantiated.

In view of the similarity of the inviscid wakes for the sphere and

_____

[*] The conical region behind the sphere, drawn in dashed line, may be interpreted as being either a dead-water region or a solid afterbody. This extension in boundary is necessary because otherwise the stream would have to be turned through 90° at the rearmost point on the sphere, which is not possible for a supersonic stream.

the hemisphere-cylinder, all the source-flow solutions worked out for
the latter case can be applied to the inviscid wake of the sphere. In
particular the solutions of Meyer (1963), Hall (1963), and Inouye (1966a,b)
will be used simultaneously, as well as first-order blast-wave theory.
Where possible the approximate solutions of Hall and the results from
blast-wave theory are preferred because of their inherent simplicity.
The work of Inouye is invaluable, however, in that it provides a means
for checking the accuracy of the other methods.

Turning to the inner, viscous portion of the wake, we note that it
has its origin in the boundary layer on the sphere. The boundary layer
separates near the meridian $\varphi = \pi/2$ (φ defined in Fig. 1), despite the
existence there of a favorable pressure gradient in the external inviscid
flow. Separation in this instance is caused by high-pressure signals
that originate in the downstream compression region near the wake neck and
propagate upstream through the subsonic portion of the wake and boundary
layer. The boundary layer after separation becomes a free shear layer
in which mixing takes place with the external inviscid flow. Viscous-
inviscid interaction then characterizes the compression process that
accompanies the turning of the shear layer back to parallel with the wake
axis. The resultant inner wake is relatively hot, and viscous effects
are then important. A short distance after the annular shear layer has
coalesced into the viscous wake proper, the flow becomes supersonic
throughout. Since the flow in the viscous wake is of the boundary-layer
type, the static pressure at a given longitudinal location is uniform
and equal to the value in the external inviscid flow at that location.
One may thus think of an inviscid-pressure "envelope" surrounding the
viscous wake. In general the development of the viscous wake depends both
on this imposed pressure field and on the diffusion processes present.
For the conditions of the current tests, however, the pressure field has
the more important effect, as will be shown in Section 4.6. To the extent
that this is true, the inviscid solutions for the hemisphere-cylinder
model are again applicable in the analysis of the viscous wake. In
addition, since the viscous wake originates in the boundary layer, a
consideration of source-flow effects on the viscous wake must necessarily
include the related effects on the boundary layer as well. To study

43

these latter effects, we need the inviscid pressure distribution over the nose region, which the numerical work of Inouye (1966a) alone provides, since the studies of Meyer and Hall do not treat the nose region in detail but only account for the cumulative effect of the nose shape through the overall nose drag.

We now proceed to a more detailed consideration of the source-flow correction schemes in the next two section.

4.5 Source-Flow Correction for Inviscid Wake

It was pointed out in the last section that the inviscid wake behind a sphere is essentially equivalent to the aft portion of the inviscid flow field of a hemisphere-cylinder model. The latter model in a source flow has been studied by several investigators (see Section 4.3). In these studies the flow variable of primary interest has been the static pressure on the surface of the model. The results show that a source flow has considerable influence on the magnitude of the surface pressure, as well as the static pressure in general. To illustrate this, the normalized pressure difference, $(p_{2_u} - p_{2_s})/p_{2_u}$, as calculated from unpublished results of Inouye[*], is presented in Fig. 19 as a function of the normalized radial distance $\hat{r} = r/R$. Here p_2 denotes the static pressure in the wake (that is, downstream of the bow shock wave), the subscripts "u" and "s" refer to uniform flow and source flow respectively, and R is the distance from the axis of symmetry to the bow shock wave. The results are for an x/d of 5 (x and d defined in Fig. 1), which is the farthest station considered by Inouye. The values of p_2 for source flow are taken from the case with $r_b/L_o = 0.02$, the smallest value of the source-flow parameter studied by Inouye. For the particular case considered, the quantity $(p_{2_u} - p_{2_s})/p_{2_u}$ ranges from 0.35 to 0.40. Thus the difference in the static pressure is an order of magnitude larger than the source-flow parameter and should not be ignored.

---

[*] The author wishes to thank Mr. M. Inouye of Ames Research Center for providing these results.

For the present investigation the quantity of more direct interest is the wake Pitot pressure p_o'. This can be deduced from the static pressure and the Mach number, the latter being also available from Inouye's unpublished results. The fractional difference $(p_{o_u}' - p_{o_s}')/p_{o_u}'$ thus calculated is plotted along with the static-pressure results in Fig. 19. Although the difference here is not as large as for the static pressure, it is still from ten to fifteen times the value of r_b/L_o. In the present experiments the source-flow parameter r_b/L_o assumes values up to 0.01. On the basis of dependence on r_b/L_o alone (if we assume a linear dependence) errors of 10 to 15 percent may thus be anticipated in the Pitot pressure in the most serious case. The quantity r_b/L_o is not the only controlling parameter, however; source-flow effects also increase with the distance x/d. In the present tests the station with the largest value of r_b/L_o is at an x/d of about 15, compared with $x/d = 5$ for the case considered in Fig. 19. Because of the added source-flow effect due to the larger value of x/d, the discrepancy in Pitot pressure can thus be expected to be substantially larger than 10 to 15 percent.

Besides affecting the magnitude of the Pitot pressure, the source flow also changes the lateral extension of the wake. It is thus desirable to find a means of correcting for both these effects. An immediately obvious approach is the direct use of method-of-characteristics results. The calculations that this method entails are involved and lengthy, however, and we seek to develop an approximate scheme that makes use of relatively simple analytical expressions. In this derivation, Inouye's more accurate method-of-characteristics results will be used either to check the approximate theory employed or to justify the assumptions that are made.

We shall first outline the essential steps in the correction method, after which the various points that require explanation will be discussed in detail.

(1) Up to the point where $\hat{r}$ is 0.7 to 0.8, the variation of the total pressure with $\hat{r}$ is assumed to be the same for uniform flow and source flow.

45

(2) At a given longitudinal station, the variation of the static-pressure ratio $p_2(\hat{r})/p_{2_e}$ with $\hat{r}$ is assumed to be unchanged from uniform flow to source flow. Here $p_{2_e} = p_2(\hat{r}_e)$ is the pressure at the surface of the cylindrical afterbody, which in the case of the wake behind a sphere is equivalent to the hypothetical "surface" separating the viscous and inviscid wakes, or the "edge" of the viscous wake. Since the ratio $p_2(\hat{r})/p_{2_e}$ cannot be deduced from experimental data, we use the results from first-order blast-wave theory, which compare favorably with the method-of-characteristics results.

(3) The longitudinal variation of the surface pressure for uniform flow, $(p_{2_e})_u$, is given satisfactorily by first-order blast-wave theory. The corresponding pressure in source flow, $(p_{2_e})_s$, is obtained by combining blast-wave theory with a simple correction formula due to Hall (1963). An alternative approach that applies to the vertically traversing probe is to deduce $(p_{2_e})_s$ at the particular station from experimental results, and then use Hall's correction formula to obtain $(p_{2_e})_u$. In either case, with the aid of (2) the transverse distributions $p_{2_u}(\hat{r})$ and $p_{2_s}(\hat{r})$ are ascertained independently of the method-of-characteristics results.

(4) With $p_{2_s}(\hat{r})$ known from (3), we then use the measured Pitot-pressure distribution $p'_{o_s}(\hat{r})$ to deduce the distribution of the total pressure $[p_{t_2}(\hat{r})]_s$. This is done through the use of routine normal-shock relations. By virtue of condition (1), the determination of $[p_{t_2}(\hat{r})]_s$ also gives the total-pressure distribution in uniform flow, $[p_{t_2}(\hat{r})]_u$.

(5) With the distribution $[p_{t_2}(\hat{r})]_u$ from (4) and $p_{2_u}(\hat{r})$ from (3), the required Pitot-pressure distribution in uniform flow, $p'_{o_u}(\hat{r})$, can be deduced accordingly.

(6) The lateral distance in the inviscid wake in source flow, r_s, is corrected by a simple scaling down of the distance with the ratio R_u/R_s,

46

where R is the distance from the wake axis to the shock wave.

In the foregoing outline, steps (4) and (5) are straightforward and need no further explanation at this point.[*] Steps (1), (2), (3), and (6) on the other hand require elaboration. Since the theory in support of these steps draws from the work of Meyer (1963), Hall (1963), and Inouye (1966a,b), we now describe these solutions in brief and note some of the results.

Meyer solved the inviscid problem of a hemisphere-cylinder model in a source flow by application of the blast-wave analogy. Formulating the problem in the manner of the second-order blast-wave theory of Sakurai (1953, 1954) and accounting for source-flow effects through the upstream boundary condition at the bow shock wave, Meyer showed that source-flow effects come into play only in the second-order terms, where they appear through a blast-wave source-flow parameter k_s defined by

$$k_s = \frac{1}{4} \left(\gamma J_o C_D \right)^{1/2} M_{1_n}^2 \left(\frac{r_b}{L_o} \right) .$$ (4.6)

In this definition J_o is a function of γ alone and is 0.877 for $\gamma = 1.4$ (see Sakurai, 1953), C_D is the drag coefficient of the nose, M_{1_n} is the Mach number upstream of the shock wave at the nose, r_b is the nose radius of the hemisphere-cylinder, and L_o is the distance from the nose to the origin of the source. With the source-flow parameter k_s as the parametric variable, solutions are obtained by numerical integration for the pressure, density, radial component of velocity, and shock-wave shape.

The second-order results from Meyer's work that are of interest to the present study are those for static pressure and shock-wave shape. Although none of these results are actually employed in the correction scheme, they are useful in the comparison of the relative accuracy of various theories. It is through this comparison that we are able to show

---

[*] Later (in Section 5.3) when the correction scheme is applied to actual test data, some of the details of these two steps will be discussed.

47

that the second-order results do not represent a significant improvement over first-order blast-wave theory. Furthermore, the first-order results, which are adopted for use in the correction scheme, are contained in the second-order results. For these reasons we summarize the pertinent results from Meyer's second-order solution.

Meyer's result for the static pressure can be written as

$$\frac{p(\bar{x},\hat{r};k_s)}{p_{1_n}} = \frac{g^{(0)}(\hat{r})}{\epsilon(\bar{x};k_s)} \{1 + \psi(\hat{r};k_s)\epsilon(\bar{x};k_s)\} \quad , \qquad (4.7)$$

where $\bar{x} = x/d$, ϵ is the parameter in the blast-wave expansion, and $g^{(0)}$ and $g^{(C)}\psi$ are respectively the first- and second-order coefficients in the expansion. The quantity ϵ is given by

$$\epsilon = \frac{J_o(R/R_o)^2}{[1-\lambda_1 J_o(R/R_o)^2]} \quad , \qquad (4.8)$$

with

$$(R/R_o)^2 = \frac{8}{(\gamma J_o C_D)^{1/2}} \frac{\bar{x}}{M_{1_n}^2} \left[1 - 2\lambda_1\left(\frac{J_o}{\gamma C_D}\right)^{1/2} \frac{\bar{x}}{M_{1_n}^2}\right], \qquad (4.9)$$

and

$$R_o^2 = (\gamma/4) C_D r_b^2 M_{1_n}^2 \quad . \qquad (4.10)$$

Source-flow effects enter into Eqs. (4.8) and (4.9) through the parameter

$$\lambda_1 = -1.992 - 2.695 \, k_s \, , \quad \text{for} \quad \gamma = 1.4 \quad . \qquad (4.11)$$

The function $g^{(0)}$ in Eq. (4.7) depends on $\hat{r}$ and γ but not on k_s

and is given by

$$g^{(0)}(\hat{r};\gamma) = \frac{2\gamma}{\gamma+1}\left[\frac{\gamma+1}{\gamma} - \frac{1}{\gamma}\hat{r}^{\frac{4\gamma}{\gamma^2-1}}\right]^{-\frac{1}{2}(\gamma^2+2\gamma-1)} . \qquad (4.12)$$

The quantity $\psi(\hat{r};k_s)$ is not expressible in closed form and must be obtained by numerical integration. Meyer's results for ψ are shown in Fig. 20 for values of k_s ranging from 0 to 1.6.

It is now possible to derive a simplified expression for the surface pressure. Since there is practically no radial gradient in the pressure near the body surface — this is confirmed by blast-wave theory — it is customary in balst-wave applications to use the pressure at the axis ($\hat{r} = 0$) as the surface pressure. The variation of $\psi_{\hat{r}=0}$ with k_s for this special case is given by the linear relation

$$\psi_{\hat{r}=0} = -0.662 - 3.596\, k_s . \qquad (4.13)$$

When Eqs. (4.8) through (4.13) are used in Eq. (4.7), the resultant pressure can be expanded in the parameter $2\lambda_1(J_o/\gamma C_D)^{1/2}M_{1_n}^2/\bar{x}$. To second order the following is obtained for the surface pressure:

$$\frac{p_{2_e}}{p_{1_n}} = 0.0671\ \sqrt{C_D}\ \frac{M_{1_n}^2}{\bar{x}} + 0.353 - 0.669\, k_s , \quad \text{for } \gamma = 1.4 . \quad (4.14)$$

The value of C_D for the hemispherical nose is taken to be 1.0.

In first-order blast-wave theory (see Lukasiewicz, 1961), the surface-pressure result is simply the first term of the right-hand side of Eq. (4.14):

$$\frac{p_{2_e}}{p_{1_n}} = 0.0671\ \sqrt{C_D}\ \frac{M_{1_n}^2}{\bar{x}} . \qquad (4.15)$$

49

The first-order result for the transverse variation of the static pressure, $p_2(\hat{r})$, will also be needed. This is most conveniently given by the ratio $p_2(\hat{r})/p_{2_e}$, for which we have from Eq. (4.7), with the second-order term omitted:

$$\frac{p_2(\hat{r})}{p_{2_e}} = \frac{g^{(0)}(\hat{r};\gamma)}{g^{(0)}(0;\gamma)} \quad . \tag{4.16}$$

The right-hand side of this equation is easily calculated from Eq. (4.12).

As to the study of Hall (1963), source-flow solutions for the hemisphere-cylinder model are obtained explicitly for surface pressure and shock-wave location. In this work the quantity r_b/L_o is used as the source-flow parameter. We will have occasion to use the ratios $(p_{2_e})_s/(p_{2_e})_u$ and R_s/R_u, for which Hall's results are

$$\frac{(p_{2_e})_s}{(p_{2_e})_u} = 1 - \frac{20\gamma}{\gamma+7}\left(\frac{r_b}{L_o}\right)\bar{x} \quad , \tag{4.17}$$

$$\frac{R_s}{R_u} = 1 + \frac{10}{\gamma+7}\left(\frac{r_b}{L_o}\right)\bar{x} \quad . \tag{4.18}$$

We are now in a position to present the supporting evidence and provide the specific formulas for steps (1), (2), (3), and (6) in the correction procedure outlined earlier.

(1) In the inviscid flow behind the bow shock wave, the total pressure p_{t_2} along any given streamline is a constant. Its value changes from streamline to streamline, however, because the fluid along the various streamlines has traversed portions of the bow shock wave that have different angles of inclination. Nevertheless, the value of p_{t_2} is a function only of the angle of inclination of the portion of the shock wave traversed by the fluid in question. This is because the total pressure ahead of the shock wave, p_{t_1}, is the same everywhere in the

50

free stream in both the uniform flow and the source flow. Now, at a given longitudinal station where the shock-wave inclination is not large, the streamlines that are not too close to the shock wave are almost horizontal. The fluid here has crossed the shock wave at points considerably farther upstream. In particular, if consideration is limited to the entropy layer next to the body, the fluid there has traversed the segment of the bow shock wave that is nearly normal to the flow axis. The slope at corresponding points of this segment does not differ significantly between uniform flow and source flow. This can be confirmed by comparing values of $(dR/dx)_u$ and $(dR/dx)_s$ calculated from Eq. (4.9). This suggests that the distribution $p_{t_2}(\hat{r})$ is the same for both uniform flow and source flow if the portion of the flow field near the shock wave is excluded from consideration.

This conjecture is in fact supported by the method-of-characteristics calculations of Inouye (1966b), whose unpublished results have been used to obtain the ratio $(p_{t_2})_s/(p_{t_2})_u$ given in Fig. 21. Although the ratio tends to behave erratically near the shock wave, it is nevertheless close to unity for a considerable portion of the wake. If the difference $[(p_{t_2})_u-(p_{t_2})_s]/(p_{t_2})_u$ is to be less than 5% for the case under consideration, then the total-pressure distribution may be assumed to be the same up to $\hat{r}$ of about 0.7. Within this range the assumption is quite good, considering the fact that the corresponding difference in the wake Pitot pressure can be as large as 30%.

(2) The normalized static-pressure distribution $p_2(\hat{r})/p_{2_e}$, as calculated from Inouye's method-of-characteristics results, is compared in Fig. 22 for uniform flow and source flow. The agreement in this case is good all the way to the shock wave, although one cannot take full advantage of this fact, in view of the limited range of validity of the assumption concerning the identity of total pressure in step (1). Shown in the same figure are points calculated from Meyer's second-order blast-wave result of Eq. (4.7), for both uniform flow and source flow, and from the first-order blast-wave result of Eq. (4.16). There is good agreement among the five sets of results, except for the second-order results for source flow in the range of $\hat{r}$ between 0.85 and 1.0, which is in any case

51

outside the range of interest. For the portion of the wake where $\hat{r}$ is less than 0.7, in particular, there is only a small difference among all five sets of results. For simplicity of calculation it will therefore be assumed that the distribution given by first-order blast-wave theory can be used for both uniform flow and source flow. The advantage here is that this result, Eq. (4.16), involves a simple analytical expression that is a function only of $\hat{r}$ and γ. The second-order results of Meyer would have improved the accuracy somewhat. They were not used, however, because of the added complexity of calculation, expecially the inclusion of the function ψ that cannot be expressed rnalytically.

(3) We now consider the available solutions or the longitudinal variation of the surface pressure p_{2_ϵ}. Results from the first- and second-order blast-wave theory, Eqs. (4.15) and (4.14) respectively, are compared in Fig. 23 against the more accurate numerical results of Inouye. The corresponding correction curves are ven in Fig. 24. The rrection formula of Hall, Eq. (4.17), has been used with the first-order blast-wave curve, even though in Hall's analysis he uses the Newton-Busemann pressure formula rather than the blast-wave expression of Eq. (4.15). This is consistent with Hall's theory, however, since in deriving the result of Eq. (4.17) for the pressure ratio Hall implies the adoption of the first-order theory by using the parabolic bow shock wave from this theory.

The method-of-characteristics results in Figs. 23 and 24 have been obtained by extrapolation and interpolation of Inouye's results. The calculations of Inouye (1966a) were carried out only to $\bar{x}$ of 5. The curve for uriform flow for points beyond is therefore extrapolated with the use of the blast-wave correlation method suggested by Van Hise (1961). In this extrapolation, we have used as a guide the method-of-characteristics calculations of Feldman (1960) for air with real-gas effects $(M_{1_n} \cong 18)$ and carrie to $\bar{x} = 50$. Also, since Inouye's results are for $r_b/L_o = 0$, 0.02, 0.04, and 0.06, the correction curve, which is for $r_b/L_o = 0.01$ (or $k_s = 0.8$), is obtained by graphical interpolation of Inouye's correction curves (his Fig. 11b) up to $x/r_b = 10$. Beyond this

52

point a linear extrapolation has been adopted to continue the linear
trend exhibit d by the original curve.

The comparison of results in Fig. 23 shows that for the range of
stations involved in this study $(\bar{x} < 15)$, first-order blast-wave theory
gives a more accurate prediction of the surface pressure than the second-
order theory for both uniform flow and source flow. In addition, the
correction formula of Hall is considerably more accurate than Meyer's
second-order result from Eq. (4.14). Strictly speaking, the numerical
results of Inouye are superior to both Meyer and Hall in terms of accuracy.
For the present study, however, we are interested in a set of relatively
simple analytical expressions that afford more flexibility with regard to
the source-flow parameter, the Mach number M_{1_n}, and the longitudinal
station $\bar{x}$. These conditions are met by the combined results of Hall,
Eq. (4.17), and first-order blast-wave theory, Eq. (4.15), and these will
be used in the current work, even though some accuracy is sacrificed in
the process.

(6) With regard to the lateral distance r_s in source flow, we correct
it to uniform flow according to the simple relation

$$r_u = (R_u/R_s)r_s \quad , \tag{4.19}$$

where R_u/R_s, the ratio of the distances to the shock wave, is given by
Eq. (4.18). This correction appears to be reasonable, since the normalized
radial distance $\hat{r} = r/R$ correlates quite well the pressure results for
uniform flow and source flow. For the ratio R_u/R_s, we have used Eq.
(4.18) rather than Meyer's result from second-order blast-wave theory, which
can be calculated from Eq. (4.9). This is because Eq. (4.18) has been
shown by Hall to be in better agreement with experimental data.

This completes the discussion of the essentials of the correction
scheme for the Pitot pressure in the inviscid wake. Some of the details
of the method will be considered in Section 5.3, following a general
description of the data-reduction procedure. We proceed now to a discussion
of the corresponding scheme for the viscous wake.

53

4.6 Source-Flow Correction for Viscous Wake

The general character of the viscous wake has been discussed in Section 4.4. It was pointed out that this portion of the wake originates in the boundary layer over the hemispherical nose. This boundary layer upon separation becomes a free shear layer that subsequently coalesces to form the viscous wake. To consider the source-flow effects on the development of the viscous wake — and in particular on the Pitot pressure — it is necessary first to study the effect on the flow in the boundary layer and the free shear layer. In the analysis to follow it will be useful to divide the viscous-flow region into two parts: (1) the boundary layer on the body together with the free shear layer, and (2) the viscous wake downstream of the neck. This division is desirable because the flow differs somewhat in these two subregions and different approaches are used to study the source-flow effects.

Boundary Layer and Free Shear Layer: We first consider only the boundary layer over the hemispherical nose prior to separation. At the end of this subsection, it will be shown that the conclusion reached for the boundary layer applies equally well through the free shear layer.

To study the effect on the boundary layer, we use the source-flow results of Inouye (1966a) for the inviscid external flow as an input to the boundary-layer solution of Cohen and Reshotko (1956). Parts of both these solutions that are pertinent to the present study will now be described in brief.

The work of Cohen and Reshotko gives self-similar solutions for two-dimensional boundary-layer flows with arbitrary pressure gradient and Mach number but with the Prandtl number Pr restricted to 1.0. The study also has as a parametric variable the quantity $S_w = h_w/h_{t_{ex}} - 1$, where the subscript "w" refers to conditions at the surface of the model. For a perfect gas S_w is equal to $(T_w/T_{t_{ex}} - 1)$ and thus is a measure of the ratio of model temperature to free-stream total temperature.

The inclusion of a non-zero pressure gradient means that the solution is not restricted to a flat plate and can be applied to the case

54

of the hemispherical nose under study in the present work, provided that local similarity is assumed. Also, the two-dimensional boundary-layer transformations used by Cohen and Reshotko must be modified to account for the axial symmetry in the flow over the hemisphere. The restriction on the Prandtl number is not a serious one for the current study in which only comparative information is being sought. The ratio of the thicknesses of the velocity and thermal boundary layers is associated with the Prandtl number (see Schlichting, 1960, p. 301). It is reasonable to assume that the source flow affects these layers to about the same extent, regardless of the ratio of the thicknesses. We shall therefore use the results for $Pr = 1.0$ for the present case where the Prandtl number is approximately 0.7. As regards the parameter S_w, it is assumed to have the value -1.0, that is, the body is assumed to be "cold". This is justifiable because the initial temperature of the model does not exceed one-fifth, and for most runs is closer to one-tenth, the value of the free-stream total temperature. Since the duration of the run is short, the model does not heat up significantly in the course of the run.

The primary input to the solution of Cohen and Reshotko is the static pressure in the inviscid stream external to the boundary layer, or equivalently, the surface pressure $p_{2_{ex}}$ on the body of interest. For the case of the hemispherical nose under study here, this information can be obtained from Inouye's surface-pressure results, which are given in Fig. 25 for uniform flow $(r_b/L_o = 0)$ and source flow $(r_b/L_o = 0.02)$. According to Inouye, although in the subsonic-transonic region the difference $[(p_{2_{ex}})_u - (p_{2_{ex}})_s]/(p_{2_{ex}})_u$ is of the same order of magnitude as the source-flow parameter r_b/L_o, the difference in the supersonic region soon becomes an order of magnitude larger than r_b/L_o. For example, the results of Fig. 25 show that at $\varphi = \pi/2$ (supersonic region) the pressure ratio $p_{2_{ex}}/(p_{t_2})_n$ for uniform flow and source flow is respectively 0.036 and 0.030, giving a difference of about 17%. With this large difference in $p_{2_{ex}}$, it is reasonable to expect that the development of the boundary layer will be significantly affected by the source flow. The magnitude of the effect can be assessed by substituting

55

both sets of surface-pressure results into the solution of Cohen and Reshotko and computing the boundary-layer growth in the two cases.

In contrast to the relatively large difference in surface pressure, the total pressure along the body streamline is the same for uniform flow and source flow. This results from the assumption of isentropic flow in the inviscid stream in both cases. In either case the total pressure corresponds to the stagnation-point pressure, which is the same in uniform flow and source flow since the fluid has traversed the normal portion of the bow shock wave and conditions ahead of it are identical in both cases.

On the basis of these considerations of surface pressure and total pressure in the inviscid stream, we are now in a position to study the effect of the source flow on the boundary layer. The details of the calculations and the various assumptions are given in Appendix D. Here we shall merely outline the approach and summarize the results:

(1) In the solution of Cohen and Reshotko, an important parametric variable is the pressure-gradient parameter β, which depends on conditions in the external flow. In the present case, by virtue of the isentropic condition, the external flow is completely specified by the pressure results of Fig. 25. It is thus possible to use these data to calculate the values of β at $\varphi = \pi/2$ for uniform flow and source flow. It is found that the difference $(\beta_s - \beta_u)/\beta_u$ is only 0.0066 for the case with $r_b/I_o = 0.02$. The variation in β is thus negligibly small, particularly when compared with the relatively large difference of 0.17 in the surface pressure.

(2) Certain ratios of flow quantities, when expressed as functions of a boundary-layer similarity variable η, are relatively insensitive to changes in β. Since the difference in β between uniform flow and source flow is small, one can assume that these ratios are the same for the two flows. Examples of ratios that satisfy this condition are the total-enthalpy ratio $h_t/h_{t_{ex}}$ and the velocity ratio V/V_{ex}.

(3) Using the identity in the ratios of velocity and total enthalpy, one can calculate the temperature ratios $T_u/T_{t_{ex}}$ and $T_s/T_{t_{ex}}$ as

56

functions of η. For the case with $r_b/L_o = 0.02$, the fractional difference $(T_u-T_s)/T_u$ at $\varphi = \pi/2$ is about 0.05 throughout almost the entire boundary layer.

(4) The temperature ratios calculated in (3) can be used to estimate the difference in the lateral extent of the boundary layer in the physical plane. At $\varphi = \pi/2$, the ratio δ_s/δ_u of the boundary-layer thickness turns out to be given by the relation

$$\delta_s/\delta_u = 1 + 4.75\ (r_b/L_o)\ , \quad \text{for}\ \ \psi = \pi/2\ . \tag{4.20}$$

The above results have been calculated for the boundary layer at $\varphi = \pi/2$. It is assumed that the boundary layer has not seperated up to this point, but that it does so shortly thereafter, so that the results describe the conditions just before separation. The process of fluid sepu..tion is complicated, and no attempt will be made to analyze it here. We shall simply assume that neither the location of separation nor the local separation mechanism is significantly differert for uniform flow and source flow. Whereas the profile shapes of specific flow quantities before and after separation undoubtedly differ considerably from each other, it seems reasonable to assume that the functional relationship in each case is independent of the slightly different local conditions that exist in uniform flow and source flow. This functional relationship is therefore assu⁻ to be the same for the two flows. With this assumption, the boundary-layer thickness δ in uniform flow and source flow bears the same relationship to each other after separation as before. Equation (4.20) then provides the ratio of the thickness of the free shear layer just after separation.

The application of Eq. (4.20) can be extended to the entire free shear layer through the following argument. The fluid in the free shear layer (from separation to recompression at the neck) is dominated by the adjoining recirculation zone, in which the static pressure, or base pressure, is essentially constant. The free shear layer thus undergoes a constant-pressure mixing process. The assumption of a constant-pressure process has in fact been used in base-flow and near-wake-flow models

by various investigators, such as Denison and Baum (1963) and Reeves
and Lees (1965). To the extent that this assumption is valid, it is
reasonable to stipulate that the ratio of the cross-sectional area of the
shear layer at separation to its area at the neck is the same for both
uniform flow and source flow. We base this assumption (regarding the
ratio of areas) on the fact that significant area changes in the shear
layer occur only if there is a marked variation in the pressure field,
as for example in an expanding flow. In the present instance of the
shear layer along the recirculation zone, however, the pressure is
essentially constant in each of the two cases of uniform flow and source
flow. The cross-sectional area of the layer can thus be expected to
remain basically unchanged from the separation point to the neck. When
mixing is included, the shear layer does undergo an area increase, owing
to the entrainment of fluid from the outside. It seems reasonable to
assume, however, that the rate of area increase is the same for both
uniform flow and source flow. This then leads to the identity in area
ratio for the two cases. On this basis Eq. (4.20) is applicable through-
out the entire free shear layer as well.

The boundary layer and the free shear layer are annular in shape
at separation. As the shear layer flows towards the axis, its thickness
increases, until eventually it coalesces just ahead of the neck. This
change in cross-sectional geometry brings about a modification of the
ratio of the lateral dimension of the viscous wake at the neck. The
ratio of the areas of the annular boundary layer at $\varphi = \pi/2$ is

$$\frac{A_{bl_s}}{A_{bl_u}} = \frac{(2r_b + \delta_s)\delta_s}{(2r_b + \delta_u)\delta_u} \cong \frac{\delta_s}{\delta_u} \quad , \qquad (4.21)$$

for $(2r_b + \delta_u) \gg (\delta_s - \delta_u)$. Since the ratio of the areas of the boundary
layer is assumed to apply as well to the areas of the coalesced shear
layer at the neck, then we have

58

$$\frac{(\bar{r}_{f_o})_s}{(\bar{r}_{f_o})_u} = 1 + \frac{(\bar{r}_{f_o})_s - (\bar{r}_{f_o})_u}{(\bar{r}_{f_o})_u} \simeq \left(\frac{A_{bl_s}}{A_{bl_u}}\right)^{\frac{1}{2}} = \left(\frac{\delta_s}{\delta_u}\right)^{\frac{1}{2}}$$

$$(4.22)$$

$$= \left(1 + \frac{\delta_s - \delta_u}{\delta_u}\right)^{\frac{1}{2}} \cong 1 + \frac{1}{2}\frac{\delta_s - \delta_u}{\delta_u} \quad,$$

where $\bar{r}_{f_o} = r_{f_o}/d$ denotes the radius of the viscous wake at the neck. Thus, from purely geometric considerations, the effect of the source flow on the lateral dimension of the viscous wake is approximately half the effect on the boundary layer.

We are now in a position to consider the viscous wake proper downstream of the neck.

Viscous Wake Proper: The problem of deriving a source-flow correction for the viscous wake will be considered in two parts. The first is to determine the extent to which the source flow influences wake growth. From this consideration we devise a correction for the lateral dimension of the wake. The second aspect of the problem is to obtain a local magnitude correction for the measured Pitot pressure.

The growth of the viscous wake is governed both by expansion due to the imposed inviscid-pressure envelope and by laminar or turbulent diffusion of various flow quantities from the inner to the outer wake. Since one of the major points of difference between the two portions of the wake is that the inner wake is much hotter, an important fluid property to be considered is the static enthalpy. Lees and Hromas (1962) have studied the problem of wake growth on a semi-empirical basis, taking into account both expansion and turbulent diffusion of static enthalpy. They assume that the development of the viscous wake can be divided approximately into three stages for which either expansion or diffusion, or both, is important. Expansion without diffusion governs the initial stage of wake growth up to the point at which the imposed inviscid pressure — and hence the pressure all the way through the viscous wake — is four times the free-stream static pressure, p_{1_n}, at the nose of

59

the model. Downstream from this point to where the pressure has decayed to p_{1_n}, both expansion and diffusion are important. Beyond this region diffusion becomes the sole mechanism. (The term "diffusion" here refers to turbulent diffusion only, since the laminar counterpart may be assumed to be insignificant by comparison.)

The farthest station encountered in the present experiments ($\bar{x} \cong 15$) is about midway through the second region considered by Lees and Hromas. According to their model, therefore, both expansion and diffusion should be included in devising a source-flow correction scheme. When their results are considered in detail, however, it is found that within the present region of interest (that is, up to $\bar{x} = 15$) the contribution to wake growth from diffusion is relatively small. By assuming that the expansion and diffusion mechanisms can be treated as uncoupled, one can devise a correction scheme that accounts for source-flow effects due to expansion alone. The diffusion contribution by virtue of its insignificant part in the overall picture of wake growth, is assumed to be the same in both uniform and source flows.

We now consider in some detail parts of the solution of Lees and Hromas, who have worked out the uniform-flow problem for $M_{1_n} = 22$. At this Mach number, the wake pressure is $4p_{1_n}$ at $\bar{x} = 7.5$ and approaches p_{1_n} at $\bar{x}$ of about 50. The turbulent-diffusion calculations were carried out for two cases: (1) pressure held constant at p_{1_n} downstream of $\bar{x} = 7.5$, and (2) pressure gradually decreasing from $4p_{1_n}$ to p_{1_n}, starting from the same axial location. The results of their calculations are shown in Fig. 26[*], in which $\bar{r}_f = r_f/d$ is the normalized radius of the viscous wake, the subscript "i" denoting the value at $\bar{x} = 7.5$, which corresponds to the station at which diffusion is first included. In case (1), $\bar{r}_f/\bar{r}_{f_i}$ remains less than 1.2 up to $\bar{x}$ of

---

[*] The curves in this figure are deduced from Fig. 4 of Lykoudis (1963) rather than from Lees and Hromas because the scales used in Lykoudis's work are easier to read.

about 25, whereas the growth is considerably faster over the same distance when expansion is taken into account in case (2). The relatively small wake growth of case (1) may be interpreted as indirect evidence that diffusion does not contribute significantly to the overall growth upstream of $\bar{x} = 25$.

In the application of the foregoing results — worked out for $M_{1_n} = 22$ — to the present case of $M_{1_n} = 17$, the longitudinal distances at which the pressure is $4p_{1_n}$ and p_{1_n} are now different. To calculate the pertinent distances in the present case we can use the pressure formula from second-order blast-wave theory, Eq. (4.14), this being preferred over the first-order expression of Eq. (4.15) because the former is more accurate for the larger distances involved here. For $M_{1_n} = 17$, it is found that the pressure is $4p_{1_n}$ at $\bar{x} = 4.5$ while p_{1_n} occurs at $\bar{x} = 30$. The corresponding distances for $M_{1_n} = 22$ were $\bar{x} = 7.5$ and $\bar{x} = 50$. Since for this earlier case turbulent diffusion was relatively unimportant upstream of about 25 body diameters, we may assume that in the present instance it is likewise unimportant for $\bar{x} < 15$. Hence in considering the data from the current experiments, in which $\bar{x}$ varies from 3 to 15, we shall account for the source-flow effects associated with the expansion process but not those connected with diffusion.

We now consider the expansion process that accompanies the decay of static pressure along the wake. At any given longitudinal station, the static pressure within the viscous wake is assumed to be uniform and equal to the pressure of the inviscid flow just outside the wake. The longitudinal variation of this pressure, for both uniform flow and source flow, is a known quantity either from the numerical solution of Inouye or from first-order blast-wave theory (see Section 4.5). In addition the ratio of the areas of the viscous wake at the neck, A_{o_s}/A_{o_u}, is given by Eqs. (4.20) and (4.22) as

$$\frac{A_{o_s}}{A_{o_u}} = \left[\frac{(\bar{r}_{f_o})_s}{(\bar{r}_{f_o})_u}\right]^2 = 1 + 4.75\left(\frac{r_b}{L_o}\right) . \qquad (4.23)$$

61

The problem is now to derive an expression for the area ratio A_s/A_u for any station farther downstream. This will then provide a means for correcting the lateral position within the wake from source flow to uniform flow. The expression for this area ratio should be in terms of the static pressure and flow quantities deducible therefrom.

To derive the desired expression, consider an elemental annular streamtube within the viscous wake. If ΔA denotes the cross-sectional area of this streamtube at any station $\bar{x}$ and ΔA^* is the fictitious sonic area associated with ΔA, then one can write the area relation[†]

$$\frac{\Delta A^*}{\Delta A} = \left(\frac{\gamma+1}{2}\right)^{\frac{1}{2}\frac{\gamma+1}{\gamma-1}} \left(\frac{p}{p_t}\right)^{\frac{\gamma+1}{2\gamma}} M \quad . \qquad (4.24a)$$

In particular, for ΔA_o and ΔA_o^* just downstream of the neck we have

$$\frac{\Delta A_o^*}{\Delta A_o} = \left(\frac{\gamma+1}{2}\right)^{\frac{1}{2}\frac{\gamma+1}{\gamma-1}} \left(\frac{p_o}{p_{t_o}}\right)^{\frac{\gamma+1}{2\gamma}} M_o \quad . \qquad (4.24b)$$

These equalities are point relations and do not require the assumption of isentropic flow. In fact the flow within the viscous wake in general is not isentropic, and the total pressure and sonic area are not invariant along any given streamtube. We shall however make the simplifying assumption that their variations for uniform flow and source flow are identical insofar as ratios between corresponding longitudinal stations are concerned. That is, we assume that for a given pair of longitudinal stations $\bar{x}_a$ and $\bar{x}_b$ within the viscous wake one may write

---

[†] In this equation and in the discussion to follow, the subscript "2" that denotes "downstream of the bow shock wave" is omitted so as to render the subscript situation more easily manageable.

62

$$\left(p_{t_b}/p_{t_a}\right)_s = \left(p_{t_b}/p_{t_a}\right)_u \quad;$$

$$\left(\Delta A_b^*/\Delta A_a^*\right)_s = \left(\Delta A_b^*/\Delta A_a^*\right)_u \quad.$$

$$(4.25)$$

Thus local differences in pressure and other thermodynamic quantities (between uniform flow and source flow) are assumed to have an insignificant effect on the ratios of total pressure and sonic area of corresponding streamtubes. If Eqs. (4.24) are now written for both uniform flow and source flow to form the ratio $\Delta A_s/\Delta A_u$ and Eqs. (4.25) are used to simplify the result, one obtains the relation

$$\frac{\Delta A_s}{\Delta A_u} = \frac{\Delta A_{o_s}}{\Delta A_{o_u}} \frac{\tilde{M}_u}{\tilde{M}_s} \left(\frac{\tilde{p}_u}{\tilde{p}_s}\right)^{\frac{\gamma+1}{2\gamma}} \quad, \tag{4.26}$$

where the notation $\tilde{Q}$ is used to denote the ratio Q/Q_o.

On the right-hand side of this equation, the ratio $\Delta A_{o_s}/\Delta A_{o_u}$ is equal to A_{o_s}/A_{o_u}, which is given by Eq. (4.23). Its value is a function of the source-flow parameter r_b/L_o but not of the lateral location of the streamtube within the viscous wake. The static pressure is uniform at a particular longitudinal station, so that the ratios $\tilde{p}_u$ and $\tilde{p}_s$ are also independent of lateral position. The compound ratio $\tilde{M}_u/\tilde{M}_s$ in general varies with the lateral coordinate. We shall assume however that at corresponding longitudinal stations, the transverse distribution of the normalized Mach number M/M_e is identical for uniform flow and source flow, that is,

$$\left(M/M_e\right)_s = \left(M/M_e\right)_u \quad. \tag{4.27}$$

The rationale behind this assumption will be discussed in Appendix E. Writing this equation for $\bar{x}_o$ and $\bar{x}$, we then obtain

$$\tilde{M}_u/\tilde{M}_s = \tilde{M}_{e_u}/\tilde{M}_{e_s} \quad. \tag{4.28}$$

63

The compound ratio $\tilde{M}_{e_u}/\tilde{M}_{e_s}$ can be calculated from the inviscid-pressure results, since at the edge of the viscous wake the flow is isentropic. When this relation is used in Eq. (4.26), the entire right-hand side becomes independent of the lateral coordinate of the particular stream-tube under consideration. The elemental areas can thus be integrated to give

$$\frac{A_s}{A_u} = \frac{A_{o_s}}{A_{o_u}} \frac{\tilde{M}_{e_u}}{\tilde{M}_{e_s}} \left(\frac{\tilde{p}_u}{\tilde{p}_s}\right)^{\frac{\gamma+1}{2\gamma}} . \tag{4.29}$$

Since the integration can be carried out from the wake axis to any desired position $\bar{r}$ within the viscous wake, the ratio A_s/A_u applies not only to the overall area of the viscous wake but also to the area of radius $\bar{r}$. Thus the desired source-flow correction formula for the lateral position $\bar{r}$ can be obtained from Eq. (4.29) as

$$\frac{\bar{r}_s}{\bar{r}_u} = \left(\frac{A_s}{A_u}\right)^{\frac{1}{2}} = \left[\frac{A_{o_s}}{A_{o_u}} \frac{\tilde{M}_{e_u}}{\tilde{M}_{e_s}} \left(\frac{\tilde{p}_u}{\tilde{p}_s}\right)^{\frac{\gamma+1}{2\gamma}}\right]^{\frac{1}{2}} . \tag{4.30}$$

We turn now to an outline of the procedure for correcting the magnitude of the measured Pitot pressure. The scheme is analogous in general to the one used in Section 4.5 for the inviscid wake.

(1) The measured Pitot pressure corresponds to the source-flow value, denoted by p'_{o_s}. In particular, its value at the edge of the viscous wake, $(p'_{o_e})_s = p'_{o_s}(\bar{r}_{e_s})$, is known from the measurements provided $\bar{r}_{e_s}$ is found. The determination of $\bar{r}_{e_s}$ will be considered in Section 5.3.

(2) If the flow at the viscous-wake edge $\bar{r}_{e_u}$ or $\bar{r}_{e_s}$ is assumed to be isentropic, the total pressure p_{t_e} is equal to the known stagnation pressure at the nose, this pressure being the same for both uniform flow and source flow. The justification for the isentropic-flow assumption

will be given following this outline.

(3) For the source-flow case, the knowledge of $(p'_{o_e})_s$ and $(p_{t_e})_s$ determines uniquely the ratios of flow quantities at $\bar{r}_{e_s}$. In particular, the quantities M_{e_s} and p_{e_s} are known.

(4) Since p_s within the viscous wake is equal to p_{e_s}, its determination in step (3), together with the measurement of p'_{o_s}, leads to the specification of the Mach number within the entire viscous wake in source flow. Thus it is possible to calculate the quantity $(M/M_e)_s$ throughout the wake.

(5) The major assumption that relates the source-flow results to those for uniform flow concerns the Mach-number ratio M/M_e. As in the derivation of the formula for correcting the lateral distance, this ratio is assumed to be the same for both uniform flow and source flow. The basis for this assumption is considered in Appendix E.

(6) To calculate M_{e_u}, we observe from step (2) that p_{t_e} is the same for uniform flow and source flow. Only one other flow quantity is needed to specify the flow, and for this the static pressure $p_{e_u} = p_u$ is chosen. The value of p_{e_u} is obtained from p_{e_s} by means of the correction formula of Hall, Eq. (4.17).

(7) The flow within the viscous wake in a hypothetical uniform stream is now specified by p_u and M_u to the extent that the desired value of p'_{o_u} can be calculated with the use of a routine normal-shock relation.

In the foregoing procedure, the isentropic-flow assumption is invoked at the edge of the viscous wake. The flow here is assumed to have expanded isentropically from the stagnation point. Strictly speaking, there are losses at the separation point and during recompression at the wake neck. Although these losses may not be negligible in each of the two cases of uniform flow and source flow, we reason that their effect on the overall correction scheme can be taken to be negligible. This can be seen from the following consideration. Owing to separation and

65

recompression losses, the actual total pressure at the edge is less than the stagnation pressure and can be represented by $k_\ell(p_{t_2})_n$. Since the losses are not large and are comparable for uniform flow and source flow, the factor k_ℓ takes on a value close . 1 for both cases. Now, the total pressure at the edge is used in steps (3) and (6) in a "parallel" manner, that is, once for uniform flow and once for source flow in identical sets of formulas. It would appear, therefore, that using $(p_{t_2})_n$ in place of $k_\ell(p_{t_2})_n$ and thereby neglecting the factor k_ℓ in the calculations will lead to only a small error in the overall results.

The analysis of the source-flow correction scheme for the viscous wake is now complete. The application of the results of this and the preceding section to the experimental data will be considered in Section 5.3.3, which also presents some of the intermediate steps.

5.   DATA REDUCTION AND RESULTS

5.1 Preliminary Remarks

The theory behind the method for correcting for transducer-galvanometer lag has been treated in Chapter 3. The corresponding theory for source-flow effects has been presented in Chapter 4. Consideration will now be given to the problem of implementing these theories and applying them to the experimental data.

Although data from both the vertically and axially traversing probes will be considered, the correction will be applied only to the results from the former. The reasons for omitting the corrections in th. case of the axially traversing probe are discussed in Section 5.2.

We shall present the results from the two probes separately in Sections 5.2 and 5.3. In each section the salient points in the data-reduction procedure are discussed in some detail. Because only Pitot-pressure data were obtained, it is not possible to deduce additional information regarding the wake flow. For this reason, no attempt will be made to discuss the experimental results in this context. Some consideration will be given, however, to the magnitude of the corrections to which the experimental data were subjected.

5.2 Results from Axially Traversing Probe

5.2.1 General Discussion

A relatively small number of runs were made with the axially traversing probe. The results from these runs will be presented without correction for response lag. As to source-flow effects, instead of applying the detailed correction scheme of Chapter 4, we adopt a simpler and more intuitive approach to account for the effects in this case.

Response corrections are considered unnecessary since the time rates of change in the pressure signal are substantially smaller than those encountered with the vertically traversing probe. Two factors contribute to this effect: (1) the spatial gradients in the wake flow are less severe in the longitudinal direction than in the traverse direction, and

67

(2) the speed of 35 fps of the axially traversing probe is small compared with the speed of about 60 fps for the vertically traversing probe, so that the spatial gradients do not appear as rapidly changing time signals to the transducers. For this reason, it was thought that only minor signal distortions were involved. It was therefore considered unnecessary to correct for the time lag due to a slow galvanometer.

An aspect of the response problem that cannot be ignored, however, is the anomalous behavior of some of the wafer transducers (see Appendix A). When a step pressure of known magnitude is applied to these transducers, they register initially anywhere from 0.6 to 1.3 of the expected pressure increase. These measured values, based on static calibration, do not reflect the expected oscillatory response that is characteristic of galvanometers; that is, if the galvanometer overshoot were included, the value of 1.3 would be even higher. Thus the sensitivity of the galvanometers as determined by static calibration is not applicable when recording time-varying signals.

In the case of the axially traversing probe this behavior of the transducers has led to difficulties that did not arise with the vertically traversing probe. In the latter instance, it was possible to ascertain experimentally the response characteristics of the particular transducer involved, primarily because this transducer responded quite accurately to the imposed pressure step. The value of k, the transducer correction factor, was found to be 1.04 (see Appendix A). When the value of k departs significantly from 1.0, however, the question of recovery to the asymptotic value becomes a difficult problem for which the response study does not provide a solution. The inconsistent response of the transducers explains in part the peculiar shape of transverse Pitot-pressure profiles that were previously reported (without comment) by Alligood, Kyser, and Tsao (1963).

In view of the serious degree of uncertainty associated with transducer performance, we consider it unwarranted to attempt a detailed source-flow correction of the data from the axially traversing probe. For the same reason no attempt will be made to reduce the data obtained from all the impact tubes in the rake. Effort will be concentrated instead on deducing the variation of Pitot pressure along the axis of

68

the wake, this being the most valuable information obtainable from the
data under these circumstances. In deducing this variation, an intuitive
method of correction will be used to account for source-flow effects.
This is discussed in the next section.

5.2.2 Data Reduction and Results

Tunnel runs with the axially traversing probe were made (both with
and without the sphere) for each of the three sets of operating conditions
listed in Section 2.7. In the wake runs, the sphere was positioned at
station F, and the useful traverse of the probe was from $\bar{x} \cong 4$ to
$\bar{x} \cong 9$. Figure 27 shows the oscillograph records of two runs made at the
same operating conditions, with and without the model. The traces
corresponding to the impact tubes located at $\bar{y} = \pm 0.094$ are marked on
the records. (The coordinate $\bar{y}$ denotes the normalized vertical distance
with respect to the measured tunnel axis, values above the axis being
positive.) These two tubes are the closest to the idealized wake axis.
In actuality the sphere falls slightly during the run; if exact position
correspondence is desired, appropriate adjustment must be made to account
for the sphere's free fall.

Since the stagnation pressure on the sphere cannot be measured
directly, this information is obtained from a corresponding calibration
run (see Section 2.7 for details). Ordinarily this stagnation pressure
is used to normalize the wake Pitot pressure so as to account for the
gradual decay in the tunnel flow. In the present instance, we are inter-
ested also in making use of any readily available means of accounting
for source-flow effects in the tunnel, other than making direct use of
the detailed correction scheme devised in Chapter 4. Now, the tunnel-
empty traces of Fig. 27(b) give the longitudinal variation of the Pitot
pressure in the free stream of the tunnel source flow. An intuitive
approach is therefore to use this free-stream variation to correct for
the source-flow effects. Given that this is the only information avail-
able, we can show that both tunnel decay and source-flow effects can best
be taken into account if the wake Pitot pressure is simply divided by
the corresponding free-stream Pitot pressure at the same location. This

relatively straightforward data-reduction procedure was followed in obtaining the longitudinal variation of the Pitot pressure near the wake axis ($\bar{r} \cong 0.1$). The results of three runs, correspu. ling to the three basic Reynolds numbers for the experiments, are presented in Fig. 28.

5.3 Results from Vertically Traversing Probe

5.3.1 Data Reduction

Figure 29 shows the oscillograph record for a wake run made with the vertically traversing probe. The traces that are labelled correspond, from top to bottom, to the arc-chamber pressure, two channels of wake Pitot pressure measured with a stationary probe (see below), photocell output, the wake Pitot-pressure profile and the associated mechanical noise measured with the traversing-probe transducers, and the pulsed signal that gives the instant at which the sphere is released into the stream. The function of the stationary probe, whose position in the wake is shown in the accompanying sketch, is to monitor the random fluctuations in the tunnel flow. This is done by using the Pitot pressure from the stationary probe in conjunction with the stagnation pressure taken from a calibration run (refer to Section 2.7 for the method of obtaining the latter pressure). By assuming that the ratio of these two pressures is essentially constant during the run, we can incorporate the random fluctuations that are present in the wake Pitot pressre into the stagnation pressure. The stagnation pressure thus modified is then used to normalize the wake Pitot-pressure profile.
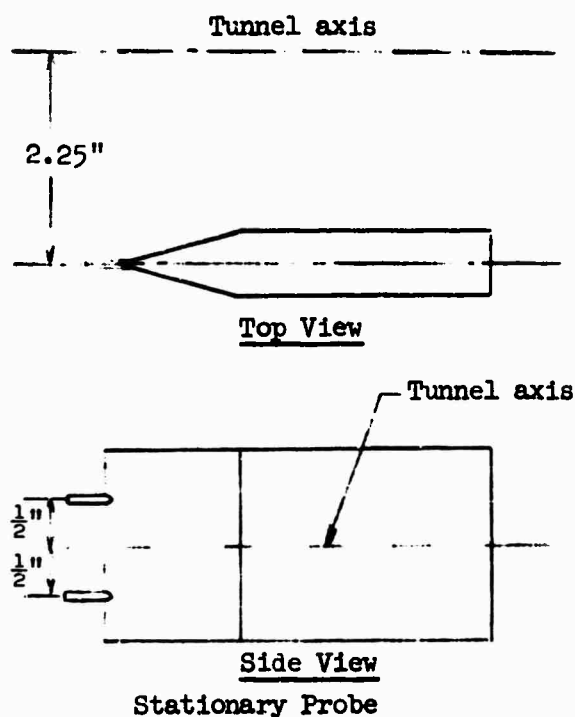
Tunnel axis

2.25"

Top View

Tunnel axis

$\frac{1}{2}$"
$\frac{1}{2}$"

Side View

Stationary Probe

70

The photocell output gives the position of the probe with respect
to the tunnel during probe traverse. Before release the sphere is
positioned at the center of the tunnel (to within about 0.05 inches);
after its release it is assumed to fall from gravity effects. Thus with
an appropriate correction for free fall, the photocell output then gives
the position of the probe with respect to the sphere, if for the moment
we assume that there is no response lag in the system associated with
the photocell. To proceed from this to a calculation of the lateral-
distance coordinate for the Pitot-pressure profile, the oscillograph
trace must first be corrected for transducer-galvanometer response lag.
(This correction will be discussed in Section 5.3.2.)

After the gravity and response corrections had been applied, it was
found that the axis of the wake, taken to be the minimum of the Pitot-
pressure profile, is at a calculated position of y of approximately
+0.2 inches. This discrepancy occurred consistently throughout the
reduced data. A probable source of error is that some response lag does
exist in the photocell galvanometer, even though its response is relatively
fast (flat to 1,000 cps). We assume that it is permissible at this point
to shift the entire profile uniformly so that the minimum corresponds to
$y = 0$. After this shift the lateral dimension of the wake is then
finally corrected for source-flow effects (see Section 5.3.3).

5.3.2 Response Correction

In Section 3.6 an example was given of the application of the
correction scheme to a specially constructed input-output pair of curves.
In that instance, we were able to recover accurately the input from the
output through a series of successive approximations. When the correction
scheme was applied to the measured Pitot-pressure profiles, however, some
difficulty was encountered at first in deducing the correct input for a
given recorded output. If the data that have been subjected to mechanical-
noise correction and subsequent normalization by the stagnation pressure
are used directly, the input curves deduced from the correction scheme
exhibit large oscillations throughout the entire curve.

An examination of the output data shows that the points do not form

71

a smooth curve, owing to the fact that it is not possible to eliminate the mechanical noise completely through the use of the accelerometer output. A factor that also contributes to the unevenness is that the random fluctuations in the tunnel flow cannot be taken out completely by normalization. Since the galvanometer functions basically as a low-pass filter, a small oscillation in the output is interpreted by the correction scheme as having originated from a much larger oscillation. In addition, the input-output relationship is not unique; that is, it is possible for more than one input to have the identical output. This aspect of the system, which is reflected in the correction scheme, apparently leads to instability problems in the iteration procedure once oscillation sets in.

To remedy the problem of exaggerated noise in the input, the output curve is first smoothed before it is subjected to the correction scheme. The curve-smoothing formulas used are standard least-squares formulas (see Hildebrand, 1956, Chapter 7, especially pp. 291-296). The degree of the polynomial and the number of points employed are dependent on the shape of the particular portion of the curve under consideration, and on how much smoothing is required. The curve-smoothing routine that was eventually incorporated in the data-reduction program consists of third-degree formulas that apply to five, seven, or nine points. Application of the formulas is repeated until the deduced input becomes free of unwanted oscillations. Apart from the foregoing modification to the recorded output, however, the basic correction scheme is identical to the method outlined in Section 3.6.

5.3.3 Source-Flow Correction

In the theory of source-flow correction presented in Chapter 4, perfect-gas relations were used throughout the derivation. Strictly speaking, the perfect-gas assumption is at times incorrect, since the temperature in parts of the wake is sufficiently high that real-gas effects must be taken into consideration. Although the temperature distribution in the wake is not given a priori, it is nevertheless known that the viscous wake is notably hot, particularly in the initial stages. The viscous-wake temperature is likely to be of the order of the

72

free-stream total temperature, which ranges approximately from 1,250 to 3,750°K in the experiments reported here (see Section 2.7). In this range of temperatures in nitrogen, whose characteristic temperature for vibration is 3,390°K, the vibrational contributions to the values of the specific heats is considerable. For example, at a temperature of 2,850°K, $c_{v_{vib}}$ is 0.89R. Thus the possible influence of caloric imperfections in the gas must be recognized.

Since the correction method itself is approximate in nature, no attempt has been made to use exact calculations for flow properties. Instead the alternative approach is adopted whereby it is shown that caloric imperfections have negligible effect on the corrected results. To show this we first make the engineering assumption that perfect-gas formulas may be used locally to relate flow quantities. The value of γ in these formulas is taken to be the value appropriate to the local flow. Typical correction calculations are then made for selected values of γ within a sufficiently inclusive range. The limiting values are taken to be 1.4 and 1.3, corresponding respectively to the value for a calorically and thermally perfect gas and to the value of 9/7 (approximately) when the vibrational modes are fully excited. The results of these calculations differ by less than 0.1%. From this we conclude that the correction method is insensitive to caloric imperfections, and that the value of 1.4 may be used for γ throughout the calculations without seriously affecting the results.

With these preliminary considerations, we now proceed to the application of the correction scheme to the results from a typical run. We begin by using the experimental pressure data to deduce the lateral variation of static pressure throughout the wake (at the given longitudinal station). This reduces essentially to finding the pressure $(p_{2_e})_s$ at the edge of the viscous wake, since in the viscous wake the pressure is assumed to be constant and equal to $(p_{2_e})_s$, and the pressure in the inviscid wake is given through the ratio $p_{2_s}(\hat{r}_s)/(p_{2_e})_s$ from the first-order blast-wave result of Eq. (4.16).

It is possible to deduce $(p_{2_e})_s = p_2(\vec{r}_{e_s})$ from experimental

73

pressure data provided the location of the viscous-wake edge, $\bar{r}_{e_s}$, can be ascertained. For the near stations (stations A, B, C) where the viscous wake is laminar, $\bar{r}_{e_s}$ can be found by observing the change of shape of the Pitot-pressure profile in going from the viscous wake to the inviscid wake. The pressure in the laminar viscous wake follows a Gaussian variation, whereas in the inviscid wake the profile exhibits a parabolic shape. The edge of the viscous wake, $\bar{r}_{e_s}$, is taken to be the point where the pressure ceases to follow the Gaussian variation. Thus for the profile shown in Fig. 30, $\bar{r}_{e_s}$ is taken to be 0.56.[*] For the more distant stations (stations D through H), the profile does not exhibit an obvious change of shape, and it is not possible to locate the edge from the mere examination of the profile. It is then necessary to assume that the value of $\bar{r}_{e_s}$ can be determined from a linear extra-polation of a plot of $\bar{r}_{e_s}$ versus $\bar{x}$ for the near stations (stations A, B, C).

With $\bar{r}_{e_s}$ known, the Pitot pressure $p'_{o_s}(\bar{r}_{e_s})$ is then obtained from the measured profile. The pressure $(p_{2_e})_s$ at the edge can now be deduced from $p'_{o_s}(\bar{r}_{e_s})$ and the local total pressure $[p_{t_2}(\bar{r}_{e_s})]_s$. This latter quantity is equal to the stagnation pressure on the model, by virtue of the assumed isentropic condition along the streamline emanating from the stagnation point (see Section 4.6 for details). We first calculate[**] the Mach number $(M_{2_e})_s$ from the normal-shock relation (with unnecessary subscripts omitted)

$$\frac{p'_o}{p_{t_2}} = \left[\frac{(\gamma+1)M_2^2}{(\gamma-1)M_2^2+2}\right]^{\frac{\gamma}{\gamma-1}}\left[\frac{\gamma+1}{2\gamma M_2^2-(\gamma-1)}\right]^{\frac{1}{\gamma-1}} . \qquad (5.1)$$

---

[*] This method of determination has been used successfully by McCarthy (1962).

[**] This is done by first rearranging Eq. (5.1) to give an equation in M_{2_e} and then solving for the root by any standard method, such as Newton's method, that is applicable to algebraic equations.

74

The static pressure $(p_{2_e})_s$ is then obtained from the Rayleigh Pitot formula

$$\frac{p_o'}{p_2} = \left[\frac{(\gamma+1)M_2^2}{2}\right]^{\frac{\gamma}{\gamma-1}} \left[\frac{\gamma+1}{2\gamma M_2^2 - (\gamma-1)}\right]^{\frac{1}{\gamma-1}} \quad . \tag{5.2}$$

With reference to the step-by-step outline of the correction schemes set forth in Sections 4.5 and 4.6, we now proceed to some of the additional details.

Inviscid Wake: In deference to the limited lateral range of validity of the assumption concerning the identity in the total-pressure distribution for uniform flow and source flow, the correction scheme is applied to data up to $\hat{r} = 0.8$ only. (Since the procedural steps to follow do not necessarily correspond to the ones in Section 4.5, a different numbering system is used here.)

(a) The pressure ratio $p_2(\hat{r})/p_{2_e}$ is the same for both flows and is given by the first-order blast-wave result of Eq. (4.16). From this equation the static-pressure distribution in source flow, $p_{2_s}(\hat{r})$, is readily obtained.

(b) The transverse distributions of static pressure and of the measured Pitot pressure are combined to give the total-pressure distribution $(p_{t_2})_s$ in source flow. In these calculations we make use of Eqs. (5.1) and (5.2), in reverse order, again using the Mach number as an intermediate variable.

(c) For the portion of the inviscid wake up to $\hat{r} = 0.8$, the transverse distribution of total pressure is the same for uniform flow and source flow. Thus the distribution in uniform flow $(p_{t_2})_u$ is known from step (b).

(d) The static-pressure distribution in uniform flow p_{2_u} is given by Eq. (4.16) provided $(p_{2_e})_u$ is known. The latter quantity is calculated

75

from $(p_{2_e})_s$ with the use of Hall's correction formula of Eq. (4.17).

(e) The required Pitot-pressure distribution in uniform flow, $p'_{o_u}(\hat{r})$, is then deduced from $[p_{t_2}(\hat{r})]_u$ from step (c) and $p_{2_u}(\hat{r})$ from step (d), again using the normal-shock relations with the Mach number as an intermediate flow parameter.

(f) The correction for the experimentally deduced lateral position in the inviscid wake is simply a scaling down of the coordinate $\bar{r}_s$ with the ratio R_u/R_s, that is, $\bar{r}_u = (R_u/R_s)\bar{r}_s$. For the ratio R_u/R_s we use Hall's source-flow solution in Eq. (4.18) for the shock-wave shape.

To ascertain which portion of the inviscid profile is to be subjected to the foregoing correction (that is, which portion satisfies the condition $\hat{r} \leq 0.8$), we need the value of either R_u or R_s. For cases where the bow shock wave intersects the wall boundary layer downstream of the probing station, it is possible to determine R_s from the Pitot-pressure trace on the oscillograph record. In this situation the transducer, in crossing the shock wave, experiences a marked pressure jump which is clearly reflected in the galvanometer output. For stations where the intersection occurs ahead of the station, the interaction between shock wave and boundary layer renders it impossible to determine R_s experimentally. We then use the following empirical formula for R_u from Van Hise (1960):

$$R_u/d = 0.98(\bar{x})^{0.48} \ . \tag{5.3}$$

Viscous Wake:

(a) The static pressure within the viscous wake at a given longitudinal station is uniform and equal to p_{2_e} at that station. It has been shown above how the value of $(p_{2_e})_s$ is deduced from experimental pressure data. The corresponding value of $(p_{2_e})_u$ for uniform flow is determined as in step (d) for the inviscid wake.

(b) The distribution $p_{2_s}(\bar{r}_s) = (p_{2_e})_s$ is used with the measured

76

Pitot-pressure distribution $p'_{o_s}(\bar{r}_s)$ to calculate the variation of Mach number, $M_{2_s}(\bar{r}_s)$, according to Eq. (5.1).

(c) In the viscous wake, the normalized Mach-number distribution $M_2(\bar{r})/M_{2_e}$ is assumed to be the same for uniform flow and source flow. Since the distribution for source flow is known from step (b) and since the value of $(M_{2_e})_u$ has already been calculated in step (e) for the inviscid wake, the distribution $M_{2_u}(\bar{r}_u)$ is fully determined.

(d) The Mach number $M_{2_u}(\bar{r}_u)$ is then used with the static pressure $p_{2_u}(\bar{r}_u) = (p_{2_e})_u$ from step (a) to calculate the required Pitot-pressure distribution $p'_{o_u}(\bar{r}_u)$ in uniform flow.

(e) The lateral position coordinate $\bar{r}_s$ in the viscous wake is corrected according to Eq. (4.30) to give $\bar{r}_u$ in uniform flow.

5.3.4 Results

For a comparison of the data before and after the successive corrections for response lag and source-flow effects, a set of results from a typical run is given in Fig. 31. Shown in this plot are (1) the uncorrected data with appropriate normalization, (2) the results corrected for response lag, and (3) the final results after the profile of (2) has been properly centered and then subjected to source-flow corrections. The difference between adjacent curves is considerable, especially between curves (1) and (2), where the shift in time (or equivalently the lateral coordinate) leads to large magnitude corrections at a given position within the profile. For the particular run illustrated in Fig. 31, the source-flow correction amounts to about 7%, which is about ten times the magnitude of the source-flow parameter $r_b/L_o = 0.0078$. For certain of the more distant stations, the source-flow correction is as much as 30%.

Representative data from selected runs, after appropriate correction, are presented in Figs. 32 through 35. The dashed curves are the results corrected for response lag, and includes a subsequent centering of the profile. The application of the source-flow correction to the dashed curves then leads to the final results given by the solid curves. The

77

results of Figs. 32, 33, and 34 correspond to runs made during the final phase of the testing program, in which only the near stations (stations A, B, C, and D) were probed. The results of Fig. 35 pertain to an earlier series of runs that covered the entire range of stations considered in Section 2.7, the farthest position being at $x/d = 15.6$ (station H).

The later runs were confined to the near stations for two reasons. First, because the Pitot pressure decreases with distance from the model, there is a corresponding increase in the relative level of mechanical noise that is apparent to the galvanometer. The recorded data for the distant stations must therefore be subjected to increased curve smoothing, and in the process some accuracy is unavoidably sacrificed. The second and more important reason for favoring the near stations is that earlier experience showed that the inviscid stream in the tunnel is too small to permit satisfactory testing at the more distant stations. When the sphere is placed far upstream into the nozzle, the interaction between the bow shock wave and the tunnel boundary layer appears to have a sizable effect on the wake at the probing station. The profile in this instance exhibits a trough-like shape that is suggestive of turbulent wakes (refer to Fig. 35 for profiles of the distant stations). Data from other sources, such as Vas, Murman, and Bogdonoff (1965) and McCarthy (1962), show that the wake is not predominantly turbulent at these stations, however. We surmise that the tunnel boundary layer has "infected" a considerable portion of the inviscid wake, if not part of the viscous wake as well. For this reason some uncertainty exists in the data for stations E and beyond.

With regard to the source-flow correction, we have used the schemes derived in Sections 4.5 and 4.6 for the distant stations as well, even though these schemes are basically for the situation in which turbulent diffusion is unimportant. This has been done for want of a better method.

The results presented are grouped according to Reynolds number.[*]

---

[*] The Reynolds number is based on the sphere diameter and on calculated free-stream conditions at the nose of the model at 20 milliseconds after the start of the run.

The three groups of runs in Fig. 32, 33, and 34 correspond to the three
basic Reynolds numbers at which the tests were performed (see Section
2.7). The nominal test-section Reynolds number for the runs of Fig. 35
is approximately 20,000 and is essentially the same as the low-Reynolds-
number series of Fig. 32. Nevertheless, two separate plots have been
used because the runs in Fig. 35 (runs 459 through 471) were made prior
to certain modifications to the tunnel arc-chamber and collector assembly.
The changes in operating conditions and flow-decay characteristics that
accompanied the modifications necessitated recalibration of the tunnel
flow. It was thought desirable, therefore, to consider runs 459 through
471 as a separate series. Since the flow in the tunnel after modification
decayed at a slower rate, it seems reasonable to expect that the data
from the post-modification runs are of better quality.

Although the usable traverse of the probe is centered roughly about
the wake axis (approximately four inches to either side), we have pre-
sented only the data from the upper half of the profiles. If the whole
profile is considered, some asymmetry is noticeable between the upper
and lower halves, even after appropriate normalization and response
correction. We presume that the asymmetry is not due to system response
lag, since the correction scheme has been shown in the example of Section
3.6 to be capable of removing the associated shape distortion. The most
plausible explanation for the asymmetry is that the effects of flow decay
are not completely accounted for by the process of normalization. Given
this circumstance, it seems reasonable to emphasize one-half of the pro-
file. The upper half was chosen because the information on this side is
more complete. This choice also minimizes interference of the probed
region from the rest of the traversing probe, should such interference
exist.

5.4 Concluding Remarks

In Sections 5.2.2 and 5.3.4 we have presented the Pitot-pressure
results obtained with the two traversing probes. No extensive discussion
was given to interpret the results because of lack of experimental know-
ledge of other quantities such as velocity and total temperature. Since

79

the verall flow picture in the wake behind a sphere is relatively complex is not possible to make simplifying assumptions and deduce the variation of other flow quantities from the measured Pitot pressure alone. A case in point concerns the assumption (often made in hypersonic inviscid flow) that the velocity is approximately constant and equal to the free-stream value. This assumption is invalid in the viscous wake, which unfortunately is also the main region of interest in wake studies. In the viscous wake, it is thus not possible to infer density variations from Pitot-pressure results.

A considerable portion of the research effort in this study was directed toward developing the rapidly traversing probes and toward perfecting the technique of testing behind a support-free sphere. From the standpoint of mechanical operation, these techniques have been shown to be feasible. The success of the overall scheme of mapping Pitot pressure is hampered somewhat, however, by inadequate instrumentation response and by source-flow effects in the tunnel stream. Both these factors can lead to substantial errors in the recorded data. It is possible, however, to correct for these effects with the use of approximate schemes devised herein. When these corrections are taken into account, the experimental systems and techniques evolved in the study appear to merit consideration as a means of studying the near wake of a cold, support-free sphere.

APPENDIX A

EXPERIMENTAL DETERMINATION OF PRESSURE-INSTRUMENTATION
TRANSFER FUNCTION

In Section 3.3, a discussion was given of the transfer function
$G(s)$ of the transducer-galvanometer system. The method of deducing the
result of Eq. (3.3) is now described. The experimental procedure is
represented schematically in Fig. 36. A pressure step of suitable size,
generated by a simple shock tube, is imposed on the pressure transducer.
The response of the transducer as seen at the amplifier output is recorded
on an oscilloscope, whereas the galvanometer output is recorded on the
oscillograph that is a normal part of the pressure-recording system. It
is thus possible to consider the response of the overall system in two
stages, a transducer-amplifier combination and the galvanometer. Separate
transfer functions are found for these two sub-systems. The overall
transfer function is then the product of the two component functions.

The shock-tube arrangement for generating the pressure-step input
to the transducer is shown in Fig. 37. The transducer is mounted onto
the end plate, the inlet tube of the transducer being flush with the
inside of the plate. As many as three transducers of the wafer type can
be accommodated in the same test. When the shock wave is reflected from
the end plate, at time $t = t_1$, say, the transducer experiences a
pressure jump of magnitude $p_5 - p_1$. The pressure level then remains at
p_5 until the disturbances that result from the interaction of the con-
tact surface with the reflected shock wave reach the transducer, say at
$t = t_2$. The time interval of interest is thus $t_2 - t_1$ at the input,
since it is during this interval that the pressure differential imposed
on the transducer conforms to a step input.

It is possible to relate p_5/p_1 to p_4/p_1 (see, for example,
Liepmann and Roshko, 1957, p. 388). For the present experiments, two
sets of conditions were used; these are as follows:

81

P_4/P_1	P_5/P_1	M_{sw}
9.17	6.60	1.581
24.30	12.50	1.890

(The test gas in there experiments was air; the initial temperatures T_1 and T_4 were assumed to be equal.) A pressure jump $p_5 - p_1$ of any desired size could then be obtained by choosing appropriate values of p_1 and p_4. Two sets of conditions are useful because for certain values of $p_5 - p_1$, the pressure level of p_1 or p_4 calculated from one set may be difficult to control accurately,* in which case the other set of conditions is usually found to give more satisfactory results. The weaker shock wave does, however, yield a longer interval $t_2 - t_1$ (approximately 4 milliseconds compared to about 2.5 milliseconds for the case of the stronger shock wave) and is preferred where a choice exists.

Typical response curves are shown in Fig. 38. The response curve of Fig. 38(a) pertains to the first stage, the transducer-amplifier combination, while the curve of Fig. 38(b) relates to the entire system including the galvanometer. In the oscilloscope record of Fig. 38(a), the upper trace is the signal from a pressure transducer located about one and a half feet upstream of the end plate. This signal serves to trigger the oscilloscope before the arrival of the shock wave at the transducer under test. It is thus possible to record the response at time $t = t_1$.

The response curve at the amplifier output may be idealized, as in Fig. 39(a), to a step of height k and with a frontal plane that is inclined rather than vertical. The quantity δ is the time taken for the output to reach the value k and in the present instance is taken to be the rise time of the transducer-amplifier stage. The output level k is a normalized quantity and its value is given by the magnitude of the output, based on static calibration, normalized with respect to the

---

* The pressure gage and manometers used to measure p_1 and p_4 were such that reading errors (percent) were more serious for certain values of the pressure than for others.

82

input pressure $p_5 - p_1$. (The latter quantity is thus shown as 1 in Fig. 39(a).) In the sense that k relates the dynamic behavior of the system to its static calibration factor, it is appropriate to define k as the "dynamic calibration factor". With the foregoing definitions of k and δ, it can be seen that if the system is linear, the shape of the normalized response curve will be independent of the magnitude of the input pressure $p_5 - p_1$.

The overall system was first checked for linearity by imposing pressure steps that ranged from 0.1 to 1.5 psi differential. For this range of pressure differentials, which corresponded to the levels encountered in the wake tests, there was no detectable dependence of the normalized response on the magnitude of the input pressure. According to the response studies of Smotherman and Maddox (1963), the rise time δ does depend on the magnitude of the input pressure, which implies that the transducer is essentially nonlinear. However, the variation in δ is significant only when relatively low pressures are involved, as encountered for example in measuring static pressure. For the present application to Pitot pressures, the transducer was assumed to have linear response and a correspondingly constant rise time. Aside from the possible small discrepancies in the input independence of δ, the linearity of the overall pressure system was confirmed by experiment. The pressure step was then held fixed at 1.0 psi for convenience and a sequence of ten tests were performed.

An unforeseen result of these tests was the discovery that initially the pressure level (p_5-p_1) measured by the transducer, based on the static calibration factor, did not correspond to the theoretically expected value of the pressure jumped generated by the shock-wave reflection. That is, the dynamic calibration factor k was found to be different from unity. After a check of the relations used for p_4/p_1 and p_5/p_1 and of the associated calculations, the possibility of erroneous computation was ruled out. Also, several transducers used in the same test consistently measured different values for $(p_5-p_1)_m$, with typical values of k ranging from 0.6 to 1.3. This suggested that the discrepancy was in the pressure-recording system. Subsequent checks for possible amplifier or galvanometer malfunction showed that none of the

83

system components external to the transducer were at fault. Furthermore,
it was established from the oscillograph record that the pressure traces
tended to settle to the correct values eventually, indicating that the
discrepancy was associated with the dynamic behavior of the pr   ire
transducer. This anomalous response characteristic is attributed to
faulty fabrication of the transducers, most probably in the construction
and positioning of the sensing coils and the spacing of the pole pieces.
The reason for this hypothesis is that there appears to be a definite
correlation between the performance of a parti_ular transducer and how
well it balances in the amplifier circuit.

Because of the unpredictable nature of the response, the transducers
must be calibrated dynamically on an individual basis if they are to be
used for measurement. For the transducer actually used in the vertically
traversing probe, the dynamic calibration factor k was found to be
1.04. An average value for the rise time δ was found to be 0.211 milli-
seconds.

The transfer function for the transducer-amplifier stage can now be
calculated directly by taking the Laplace transform of the idealized
response curve of Fig. 39(a). The evaluation of the Laplace transform
is simplified if the response diagram is taken to be the difference
$f' - f''$, where f' and f" are shown in Fig. 39(b) to be two parallel
lines of slope k/δ whose t-intercepts are 0 and δ respectively.
The Laplace transform of f' and f" are standard expressions. The
transfer function of the transducer-amplifier stage, $G_1(s)$, is thus

$$G_1(s) = \frac{\mathcal{L}\{f'\} - \mathcal{L}\{f''\}}{\mathcal{L}\{\text{unit step}\}}$$

$$= \frac{(k/\delta)(1/s^2) - (k/\delta)(e^{-s\delta}/s^2)}{(1/s)} = \frac{k}{s\delta}(1 - e^{-s\delta}) .$$

(A.1)

The transfer function for the galvanometer stage was taken to be
the standard function for a second-order system, which is characteristic
of galvanometers in general. The response curve of Fig. 38(b) provides
the necessary check. It is possible to deduce from this curve the

84

natural undamped frequency ω_n and the damping factor ζ for the galvanometer in question. These values correspond closely to the manufacturer's specifications. The response curve of Fig. 38(b) represents the overall system response, which includes the transducer-amplifier stage. Since the rise time δ is small compared with the overall system rise time, the matching with a second-order system would be valid. The standard second-order transfer function is given by

$$G_2(s) = \frac{\omega_n^2}{s^2 + 2\zeta\omega_n s + \omega_n^2} \quad . \tag{A.2}$$

The overall system transfer function is thus

$$G(s) = G_1(s)\, G_2(s)$$

$$= \frac{k\omega_n^2}{\delta} \frac{1 - e^{-S\delta}}{s(s^2 + 2\zeta\omega_n s + \omega_n^2)} \quad . \tag{A.3}$$

85

APPENDIX B

THE Z-TRANSFORM OF THE TRANSFER FUNCTION

The system transfer function for continuous-data signals has been found in Appendix A as

$$G(s) = \frac{k\omega_n^2}{\delta} \frac{1 - e^{-s\delta}}{s(s^2 + 2\zeta\omega_n s + \omega_n^2)} \quad . \tag{B.1}$$

In Section 3.4, a fictitious data-sampling process was introduced into the transducer-galvanometer system to describe the data-reduction procedure of reading discrete data points off the oscillograph record. In the mathematical model for the resulting sampled-data system (discussed in Section 3.5), a fictitious data hold was inserted to interpolate the data between adjacent sampling instants $t = 0, T, 2T, 3T, \ldots$. For the transducer-galvanometer system with the transfer function of Eq. (B.1), a first-order data hold $Q(z,s)$ of Eq. (3.10) was found to give the best results. The transfer function including the data hold is then

$$\tilde{G}(s,z) = G(s) \, Q(z,s)$$

$$= \frac{k\omega_n^2}{T\delta} \frac{z(1-z^{-1})(1-e^{-s\delta})}{s^3(s^2 + 2\zeta\omega_n s + \omega_n^2)} \quad . \tag{B.2}$$

From the theory of sampled-data systems, the z-transform of $\tilde{G}(z,s)$ is given by (see Ragazzini and Franklin, 1958, p. 57)

$$\tilde{G}(z) = \sum_{\substack{\text{poles of} \\ \tilde{G}(z,p)}} \text{Residue} \left[\tilde{G}(z,p) \frac{1}{1 - e^{pT}z^{-1}} \right] , \tag{B.3}$$

where p is a dummy variable used in place of the Laplace variable s. The function $\tilde{G}(z,p)$ of Eq. (B.2) has a third-order pole at

86

$p = 0$, and simple poles at $p = -\alpha, -\bar{\alpha}$, where $\bar{\alpha}$ is the complex conjugate of α, and $\alpha \equiv \omega_n(\zeta + i\sqrt{1-\zeta^2})$, since $\zeta \le 1$. Equation (B.3) may now be written

$$\mathcal{G}(z) = \sum_{p=0,-\alpha,-\bar{\alpha}} \text{Res}\left[z(1-z^{-1})^2 \frac{k\omega_n^2}{T\delta} \frac{1 - e^{-p\delta}}{p^3(p+\alpha)(p+\bar{\alpha})(1-e^{pT}z^{-1})} \right]$$

(B.4)

$$= z(1-z^{-1}) \frac{k\omega_n^2}{T\delta} \sum_{p=0,-\alpha,-\bar{\alpha}} \text{Res}\left[\frac{1 - e^{-p\delta}}{p^3(p+\alpha)(p+\bar{\alpha})(1-e^{pT}z^{-1})} \right] ,$$

the last step being permissible since the factor that is not considered in the evaluation of the residues does not contain the variable p explicitly.

Residue at $p = 0$: Define $\phi(p)$ as

$$\phi(p) \equiv \frac{1 - e^{-p\delta}}{(p+\alpha)(p+\bar{\alpha})(1-e^{pT}z^{-1})} .$$

(B.5)

Then the residue at the third-order pole at $p = 0$ is

$$\text{Res}\,(0) = \frac{1}{2!} \left. \frac{d^2\phi}{dp^2} \right|_{p=0}$$

(B.6)

$$= \frac{c_0 + c_1 z^{-1}}{\omega_n^4(1-z^{-1})^2} ,$$

where $c_0 = -2\zeta\bar{\delta} - \bar{\delta}^2/2$,

$\quad\quad c_1 = (2\zeta+\bar{T})\bar{\delta} + \bar{\delta}^2/2$,

and $\quad \bar{\delta} = \omega_n\delta, \quad \bar{T} = \omega_n T$.

87

<u>Residues at $p = -\alpha$, $p = -\bar{\alpha}$:</u> It is convenient to evaluate the residues at $p = -\alpha$ and $p = -\bar{\alpha}$ simultaneously, because of the conjugate nature of the roots α and $\bar{\alpha}$. We then have

$$\text{Res}(-\alpha) + \text{Res}(-\bar{\alpha}) = \frac{1 - e^{-p\delta}}{p^3(p+\bar{\alpha})(1-e^{pT}z^{-1})}\bigg|_{p=-\alpha} + \frac{1 - e^{-p\delta}}{p^3(p+\alpha)(1-e^{pT}z^{-1})}\bigg|_{p=-\bar{\alpha}}$$

$$\tag{B.7}$$

$$= \frac{f_0 + f_1 z^{-1}}{\lambda\omega_n^4(1+d_1 z^{-1}+d_2 z^{-2})} \quad ,$$

where $d_1 = 2e^{-\zeta\bar{T}}\cos \lambda T$,

$\quad\quad d_2 = e^{-2\zeta\bar{T}}$,

$\quad\quad f_0 = -\sin 3\theta - e^{\zeta\bar{\delta}}\sin (\lambda\bar{\delta}-\cdots)$,

$\quad\quad f_1 = -e^{-\zeta\bar{T}}\sin (\lambda\bar{T}-3\theta) + e^{-\zeta(\bar{T}-\bar{\delta})}\sin (\lambda\bar{T}+\lambda\bar{\delta}-3\theta)$,

and $\quad \lambda = \sqrt{1-\zeta^2}$,

$\quad\quad \theta = \tan^{-1}(\lambda/\zeta)$, from the notation $\alpha = \omega_n e^{i\theta}$.

Combining Eqs. (B.4), (B.6), and (B.7), we obtain

$$\mathcal{G}(z) = \frac{k}{\lambda\bar{T}\bar{\delta}}\frac{m_{-1}z + m_0 + m_1 z^{-1} + m_2 z^{-2}}{1 + d_1 z^{-1} + d_2 z^{-2}} \quad , \tag{B.8}$$

where $m_{-1} = \lambda c_0 + f_0$,

$\quad\quad m_0 = \lambda c_0 d_1 + \lambda c_1 - 2f_0 + f_1$,

$\quad\quad m_1 = \lambda c_0 d_2 + \lambda c_1 d_1 + f_0 - 2f_1$,

$\quad\quad m_2 = \lambda c_1 d_2 + f_1$.

The system parameters were found experimentally to have the values

88

$$k = 1.04 \quad,$$

$$\delta = 0.211 \text{ milliseconds} \quad,$$

$$\zeta = 0.6266 \quad,$$

$$\omega_n = 1900 \text{ radians/sec.}$$

The sampling period T was taken to be 0.25 milliseconds, even though
during data reduction, data were read off the oscillograph record every
one-half millisecond. A value of 0.25 milliseconds for T was found to
give more accurate results compared to the case with T = 0.5 milliseconds
because with the sampling rate doubled, the first-order or linear data
hold reconstructs the sampled data into a curve that resembles more
closely the original continuous data curve. The information at the
sampling instants between data readouts was obtained with the use of
interpolation formulas (see discussion at the end of Section 3.5).

With the values of the system parameters thus specified, it is
possible to evaluate the constants that appear in Eq. (B.8). An electronic
computer was used to perform the arithmetic involved in transforming the
quotient into a series in z^{-1}:

$$\tilde{G}(z) = r_{-1}z + r_0 + r_1 z^{-1} + r_2 z^{-2} + \cdots \quad . \tag{B.9}$$

The values of a representative number of r_i's are listed in the table
at the end of this appendix. It can be seen from Eq. (3.13) that the

sum $\sum_{i=-1}^{n} r_i$ represents the response of the system at $t = nT$ to a

unit-step input. Thus the alternation in sign of successive sequences
of 8 or 9 r_i's indicates that oscillations (of approximate period 16T,
say) are present in the calculated response output. The general trend
of decreasing coefficients beyond r_3 implies that the oscillation
eventually damps out. These two observations are in keeping with the
characteristic behavior of an underdamped system.

The fact that the coefficient r_{-1} is nonzero means that the out-
put has a deflection at $t = -T$, which is physically inadmissible. This

89

behavior is due to the inclusion of the first-order data hold that effects a linear interpolation between the zero input at $t = -T$ and the unit-step input at $t = 0$. For a similar reason, r_0 is not zero as it should be in principle. In the application of the coefficients r_i's in the correction scheme (see Appendix C), r_{-1} was taken to be zero, whereas the nonzero value of r_0 was retained. This approach was considered reasonable, since the output calculated in this manner, for a unit-step input, agreed well with the experimentally recorded output discussed in Appendix A.

Coefficients in Series Expansion of $\tilde{G}(z)$

i	r_i	i	r_i
-1	-6.4792689,-03	25	1.4417189,-04
0	2.3199572,-02	26	-5.8938240,-06
1	9.9651717,-02	27	-8.7658587,-05
2	2.0891119,-01	28	-1.1811693,-04
3	2.3429669,-01	29	-1.1520153,-04
4	2.0919678,-01	30	-9.4369901,-05
5	1.6044702,-01	31	-6.7135251,-05
6	1.0679144,-01	32	-4.0914622,-05
7	5.9384394,-02	33	-1.9628658,-05
8	2.3333841,-02	34	-4.6157902,-06
9	-4.3871813,-04	35	4.4327616,-06
10	-1.3474022,-02	36	8.6825478,-06
11	-1.8413414,-02	37	9.5770539,-06
12	-1.8064358,-02	38	8.4721437,-06
13	-1.4857427,-02	39	6.4491078,-06
14	-1.0609776,-02	40	4.2573953,-06
15	-6.4970768,-03	41	2.3384101,-06
16	-3.1450905,-03	42	8.9003754,-07
17	-7.7192826,-04	43	-5.7138223,-08
18	6.6547992,-04	44	-5.6988905,-07
19	1.3470357,-03	45	-7.5752768,-07
20	1.4980708,-03	46	-7.3458316,-07
21	1.3313658,-03	47	-5.9934902,-07
22	1.0172732,-03	48	-4.2476382,-07
23	6.7432266,-04	49	-2.5761347,-07
24	3.7268871,-04	50	-1.2245572,-07

APPENDIX C

DERIVATION OF RESPONSE CORRECTION SCHEME

In Section 3.5, we arrived at expressions for the z-transform $P_{out}(z)$ for the pressure output and $\tilde{G}(z)$ for the system transfer function. These expressions are given in Eqs. (3.7) and (3.12), respectively. The problem in Section 3.6 is to deduce the input z-transform $P_{in}(z)$ from the relation[*]

$$P_{out}(z) = \tilde{G}(z) \cdot P_{in}(z) \quad . \qquad (C.1)$$

It is convenient in what follows to use the simpler notation

$$X(z) = P_{in}(z) \quad ,$$

$$Y(z) = P_{out}(z) \quad .$$

Equation (C.1) then becomes

$$Y(z) = \ddot{G}(z) \cdot X(z) \quad , \qquad (C.2)$$

with

$$X(z) = x_0 + x_1 z^{-1} + x_2 z^{-2} + \cdots$$

$$Y(z) = y_0 + y_1 z^{-1} + y_2 z^{-2} + \cdots \qquad (C.3)$$

$$\tilde{G}(z) = r_{-1} z + r_0 + r_1 z^{-1} + r_2 z^{-2} + \cdots$$

The coefficients x_m, y_m are the values of the input and output, respectively, at $t = mT$ (see Fig. 40). The term r_{-1} in $\tilde{G}(z)$ is a spurious effect of the inclusion of the first-order data hold. Since r_{-1} is an order of magnitude smaller than r_1 (see values listed in

---

[*] This relation is identical to Eq. (3.15).

Appendix B), the deletion of the z term in $\tilde{G}(z)$ does not cause any serious error but does, on the other hand, simplify the presentation of the ensuing analysis. The coefficient r_0 is retained, however, because it does not cause any added difficulty in the algebra.

Substituting Eqs. (C.3) into Eq. (C.2) and equating the coefficients of z^{-m}, we obtain

$$y_m = \sum_{j=0}^{m} r_j x_{m-j} \quad . \tag{C.4}$$

Let x', x'' be respectively the ith and $(i+1)^{th}$ approximation of x. Then from Eq. (C.4) we have

$$y'_m = \sum_{j=0}^{m} r_j x'_{m-j} \quad , $$

$$ \tag{C.5}$$

$$y''_m = \sum_{j=0}^{m} r_j x''_{m-j} \quad , $$

where y' and y'' are the outputs corresponding to the x' and x'' sequences respectively. With the notation $\epsilon = x'' - x'$, Eqs. (C.5) can be rewritten as

$$y''_m - y'_m = \sum_{j=0}^{m} r_j \epsilon_{m-j} \quad . \tag{C.6}$$

Now from Eq. (C.4) and Fig. 40, it can be seen that $y_m = \sum_{j=0}^{m} r_j$ is the response of the system at $t = mT$ to a unit-step input at $t = 0$. For a system with a dynamic calibration factor $k = 1.04$, we have

$$\lim_{m \to \infty} \sum_{j=0}^{m} r_j = k = 1.04 \quad . \tag{C.7}$$

Consider the values of r_0 through r_{10} from the table of Appendix B:

93

j	r_j
0	0.0232
1	0.0997
2	0.2089
3	0.2343
4	0.2092
5	0.1604
6	0.1068
7	0.0594
8	0.0233
9	- 0.0004
10	- 0.0135

From this we find that the sum $\sum_{j=0}^{6} r_j$ has a value of 1.0425. Thus r_0 through r_6 roughly speaking account for the correct response that corresponds to the limiting value given by Eq. (C.7). The remaining r_j's represent the oscillations that occur in the output of an under-damped system. If the errors ϵ throughout Eq. (C.6) are assumed to be of the same order of magnitude, the net contribution of $\sum_{j=7}^{m} r_j \epsilon_{m-j}$ will then be approximately zero, and from Eq. (C.6) we can write

$$y_m'' - y_m' = \sum_{j=0}^{6} r_j \epsilon_{m-j} \quad . \tag{C.8}$$

The important assumption is now made that the errors ϵ_{m-j}, for $j = 0$ through 6, form a linear sequence (see sketch on next page); that is, they are expressible in the form

$$\epsilon_{m-j} = \epsilon_0 - (j)\Delta\epsilon \quad . \tag{C.9}$$

94
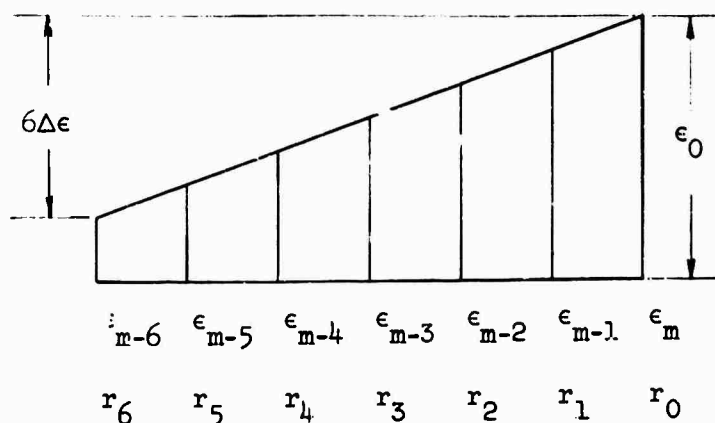
It is then possible to use the idea of a weighted average to determine which of the errors ϵ_{m-j} most accurately satisfies the relation

$$\epsilon_\nu \sum_{j=0}^{6} r_j = \sum_{j=0}^{6} r_j \epsilon_{m-j} \quad .$$ (C.10)

Letting $\epsilon_\nu = \epsilon_0 - \nu\Delta\epsilon$ and solving for ν from Eqs. (C.9) and (C.10), we obtain

$$\nu = \frac{\sum_{j=0}^{6} (j)r_j}{\sum_{j=0}^{6} r_j} = 3.46 \quad .$$ (C.11)

Thus if ν is approximated by 3, ϵ_ν becomes ϵ_{m-3}, and Eq. (C.8) may be approximated as

$$y_m'' - y_m' \cong \epsilon_{m-3} \sum_{j=0}^{6} r_j \quad .$$ (C.12)

Since $\epsilon = x'' - x'$, this equation can be rearranged to give

95

$$x_n'' = x_n' + \frac{y_{n+3}'' - y_{n+3}'}{\sum\limits_{j=0}^{6} r_j} \quad , \tag{C.13}$$

where $(m-3)$ has been replaced by n. On the right-hand side of Eq. (C.13), y'' is the output corresponding to the improved input x''. It is then reasonable to assume that if the recorded output y is used in place of y'', the quantity x'' calculated from Eq. (C.13) is closer to the actual input x and therefore represents an improvement on x'. We can thus write the final result as

$$x_n'' = x_n' + \frac{y_{n+3} - y_{n+3}'}{\sum\limits_{j=0}^{6} r_j} \quad . \tag{C.14}$$

In deriving this equation, the error sequence used goes back to $(m-6)$, or $(n-3)$; the derivation is thus applicable only for $n \geq 3$.

For $n = 2$, the ϵ corresponding to r_6 is zero (refer to sketch). The summation in Eq. (C.10) is carried to $j = 5$ only, resulting in $\nu = 3.06 \cong 3$. Hence the only modification required in Eq. (C.14) is in the summation of r_j's as follows:

$$x_2'' = x_2' + \frac{y_5 - y_5'}{\sum\limits_{j=0}^{5} r_j} \quad . \tag{C.15}$$

In a similar manner, expressions can be derived for $n = 1$ and $n = 0$ as follows:

96

$$x_1'' = x_1' + \frac{y_4 - y_4'}{\sum\limits_{j=0}^{4} r_j} \quad ,$$

$$(C.16)$$

$$x_0'' = x_0' + \frac{y_2 - y_2'}{\sum\limits_{j=0}^{2} r_j} \quad .$$

The initial guess for the input is taken to be the recorded pressure output shifted backward in time by 1 millisecond. The correction scheme works well with this guessed input except where jump discontinuities occur. Consider for example the input shape of Fig. 15 and the corresponding output. In the neighborhood of the point $t = 5$ milliseconds, the shifted output differs significantly from the input, and the correction scheme may break down here. To remedy the situation, the portion of the shifted output that causes the difficulty is deleted and replaced by a linearly extrapolated segment, shown by the dashed line in Fig. 15. A jump discontinuity is provided for, the point at which it is placed in the guessed output being determined fairly accurately from where the sharp rise occurs in the output. The guessed input for the segment to the left of $t = 5$ milliseconds may be any straight line with approximately the same slope as that of the recorded output in that interval.

The indirect correction scheme derived here is not unique. It is conceivable that two slightly different inputs will give the same output. For instance, the same signal superimposed on two carrier voltages of different, but high, frequencies will probably produce such an effect. It is then not possible to differentiate between the two cases when the inputs are to be calculated from the identical output. A case in point is when the recorded output contains small-amplitude oscillations that are superimposed on the main Pitot-pressure curve. These are in actuality due to random variations in the tunnel flow or to ramnents of the mechanical noise that are not completely removed by the monitoring accelerometer

97

output. When the recorded output is subjected to the correction scheme however, the oscillations are taken to be the result of a filtering process of large-amplitude oscillations in the original pressure trace. Successive improvement on the guessed input then introduces an unstable iterative procedure. This difficulty was in fact encountered in the data-reduction procedure. To eliminate the spurious effect, a certain amount of curve smoothing of the recorded output was found to be necessary before it could be used as the initial guessed input. This problem is discussed in some detail in Section 5.3.2. Provided that this instability condition is taken into consideration, the indirect correction scheme derived herein is judged to be adequate for the present application.

APPENDIX D

SOURCE-FLOW EFFECTS ON THE BOUNDARY LAYER

The boundary-layer transformations for two-dimensional flow used by Cohen and Reshotko (1956) are based on Stewartson's transformation and can be written

$$\xi' = \lambda_v \int_0^{\bar{s}} \frac{p_{ex}}{p_{t_{ex}}} \frac{a_{ex}}{a_{t_{ex}}} d\bar{s} \quad ,$$

$$\zeta' = \frac{a_{ex}}{a_{t_{ex}}} \int_0^{\bar{n}} \frac{\rho}{\rho_{t_{ex}}} d\bar{n} \quad ,$$

where $\bar{s}$ and $\bar{n}$ are nondimensionalized distances tangential and normal to the body surface; a, p, and ρ are respectively the speed of sound, pressure, and density of the fluid, and λ_v is a constant of proportionality in the linear viscosity law $(\mu/\mu_{t_{ex}}) = \lambda_v (T/T_{t_{ex}})$. The subscript "t" refers to total conditions, while "ex" pertains to the local inviscid flow outside the boundary layer (external flow). The value of λ_v is determined by the condition that the viscosity at the model temperature given by the linear law should match the value from Sutherland's law. Thus λ_v assumes the value

$$\lambda_v = \left(\frac{T_w}{T_{t_{ex}}}\right)^{\frac{1}{2}} \left(\frac{T_{t_{ex}} + T_{su}}{T_w + T_{su}}\right) \quad ,$$

where T_{su} is the Sutherland constant, which for nitrogen is 102.7°K (see Chapman and Cowling, 1952).

For axially symmetrical flow, as for example over the hemispherical nose under study, the transformation must be modified as follows (see for example Moore, 1964),

99

$$\xi = \lambda_v \int_0^{\bar{s}} \left(\frac{p_{ex}}{p_{t_{ex}}} \frac{a_{ex}}{a_{t_{ex}}} \right) \bar{r}^2 d\bar{s} \quad , \qquad (D.1a)$$

$$\zeta = \frac{a_{ex}}{a_{t_{ex}}} \int_0^{\bar{n}} \left(\frac{\rho}{\rho_{t_{ex}}} \right) \bar{r} \, d\bar{n} \quad , \qquad (D.1b)$$

where $\bar{r}$ is the nondimensionalized distance measured from the axis of symmetry.

The similarity variable used in the boundary-layer solutions is defined by

$$\eta = \zeta \left[\frac{m+1}{2} \frac{U_{ex}}{\nu_{t_{ex}} \xi} \right]^{\frac{1}{2}} \quad , \qquad (D.2)$$

where $\nu_{t_{ex}}$ is the kinematic viscosity at $T_{t_{ex}}$, and U_{ex} is the transformed velocity in the external inviscid stream, related to the physical velocity V_{ex} by:

$$U_{ex} = \frac{a_{t_{ex}}}{a_{ex}} V_{ex} \quad . \qquad (D.3)$$

The quantity m is the exponent in the power-law description of the inviscid flow

$$U_{ex} = C\xi^m \quad , \qquad (D.4)$$

Where C is a constant. In the present application, the inviscid flow cannot be described by this equation with a single value of m that is applicable over the entire hemispherical nose. It is assumed nevertheless that the power-law description applies locally, so that at a particular point of interest, the appropriate value of m to take is the one for which Eq. (D.4) describes the flow in the immediate neighborhood of

the point.

An important parameter in the solutions is the pressure-gradient parameter β, which is defined in terms of m as

$$\beta = \frac{2m}{m+1} \quad . \tag{D.5}$$

A second parameter is the enthalpy function at the model surface given by $S_w = h_w/h_{t_{ex}} - 1$. For the present experiments, h_w is assumed to be negligible in comparison with $h_{t_{ex}}$, so that S_w takes on the value -1.0.

It is now possible to show that the values of β for uniform flow and source flow do not differ significantly from each other. To calculate β, or equivalently m, we see from Eq. (D.4) that m is given by the expression $m = (\xi/U_{ex})(dU_{ex}/d\xi)$, which can be evaluated graphically from a plot of U_{ex} versus ξ. This plot in turn can be deduced from the surface-pressure distributions in Fig. 25 by application of the transformations (D.1a) and (D.3), since by virtue of the isentropic condition in the inviscid stream the pressure ratio completely specifies the flow. The values of β thus calculated for uniform flow $(r_b/L_o = 0)$ and source flow $(r_b/L_o = 0.02)$ at $\varphi = \pi/2$ are 1.674 and 1.685 respectively. The difference $(\beta_s - \beta_u)/\beta_u$ is 0.0066, which is substantially smaller than the source-flow parameter r_b/L_o.

We now examine the solutions of Cohen and Reshotko for the total-enthalpy ratio $h_t/h_{t_{ex}}$ and the velocity ratio V/V_{ex}, particularly with regard to their variation with the pressure-gradient parameter β. These solutions are given in Fig. 41 for non-negative values of β, that is, for cases where the pressure gradient is favorable. For values of β approaching the limiting value of 2, both ratios are insensitive to changes in β. This is particularly true of the total-enthalpy ratio, and Lees (1956) for example invoked the associated invariance of total-enthalpy gradient at the wall to justify the omission of the latter in computing the laminar heat transfer on cold blunt-nosed bodies. In the present instance, since no actual solution of the boundary-layer problem is being attempted, it is not necessary to neglect the pressure gradient

101

altogether. We can assume, however, that the distribution of the total-enthalpy ratio as a function of the similarity variable η is the same for uniform flow and source flow. In view of the small difference of 0.0066 between β_u and β_s, particularly when these are close to the limiting value of 2, we shall extend the assumption to include the invariance of the velocity ratio from uniform flow to source flow.

With the assumption of the identity of the ratios of total enthalpy and velocity, it is now possible to compare the uniform-flow and source-flow distributions of the static-temperature ratio T/T_{ex}. Starting with $h_t/h_{t_{ex}}$ and using the energy equation $h_t = \frac{1}{2} V^2 + \gamma RT/(\gamma-1)$, one obtains for T/T_{ex} the expression

$$\frac{T}{T_{ex}} = (1 + \frac{\gamma-1}{2} M_{ex}^2) \frac{h_t}{h_{t_{ex}}} - \frac{\gamma-1}{2} M_{ex}^2 (\frac{V}{V_{ex}})^2 \quad . \tag{D.6}$$

On the right-hand side of this equation the ratios $h_t/h_{t_{ex}}$ and V/V_{ex} are taken to be the same for uniform flow and source flow, and are obtainable from the solution of Cohen and Reshotko. The values for M_{ex_u} and M_{ex_s} at $\varphi = \pi/2$, deduced from the pressure results of Fig. 25, are respectively 2.81 and 2.93. The temperature distributions T_u/T_{ex_u} and T_s/T_{ex_s} thus calculated from Eq. (D.6) are shown in Fig. 42. The curves are very close to each other and are identical for values of η larger than 2.5. For smaller values of η, the difference is of the same order as the source-flow parameter $(r_b/L_o = 0.02)$. Within the accuracy of the present study, this difference is negligible and the temperature-ratio distribution can be taken to be identical in the transformed η-variable; that is,

$$\frac{T_s}{T_{ex_s}} = \frac{T_u}{T_{ex_u}} \quad \text{for any given } \eta \quad . \tag{D.7}$$

We are now in a position to consider how the boundary layer in the physical plane differs from uniform flow to source flow. The transformation

102

from the similarity variable η back to the physical coordinate $\bar{n}$ is accomplished with the use of Eqs. (D.1b) and (D.2), with the result

$$\bar{n} = \frac{a_{t_{ex}}}{a_{ex}} \frac{p_{t_{ex}}}{p_{ex}} \left[\frac{2}{m+1} \frac{\nu_{t_{ex}} \xi}{U_{ex}} \right]^{1/2} \int_0^\eta \frac{1}{\bar{r}} \frac{T}{T_{t_{ex}}} \, d\eta \quad . \qquad (D.8)$$

On the right-hand side of this equation, all quantities except the integral have been used before in the determination of β and are therefore known. By virtue of the relation (D.7), the ratio of the integral for uniform flow and source flow can be written

$$\frac{\displaystyle\int_0^\eta \frac{1}{\bar{r}_s} \frac{T_s}{T_{t_{ex}}} \, d\eta}{\displaystyle\int_0^\eta \frac{1}{\bar{r}_u} \frac{T_u}{T_{t_{ex}}} \, d\eta} = \frac{T_{ex_s}/T_{t_{ex}}}{T_{ex_u}/T_{t_{ex}}} \quad , \quad \text{for any given} \quad \eta \quad . \qquad (D.9)$$

Here we have used the condition that at $\varphi = \pi/2$

$$\bar{r}_s = \bar{r}_b + \bar{n}_s$$

$$\approx \bar{r}_b + \bar{n}_u$$

$$= \bar{r}_u \quad ,$$

since $\bar{r}_b$ is much larger than the difference $\bar{n}_s - \bar{n}_u$.

With these considerations, one can now calculate the ratio $\bar{n}_s/\bar{n}_u$ from Eq. (D.8). Because the ratio of the temperature integrals in Eq. (D.9) is independent of η, the ratio $\bar{n}_s/\bar{n}_u$ is the same for the entire boundary layer. Hence it is necessary to consider only the ratio of the "boundary-layer thickness" δ, with the result

$$\frac{\delta_s}{\delta_u} = 1.095 \quad , \quad \text{for} \quad r_b/L_o = 0.02 \quad .$$

103

For application to cases where r_b/L_o is smaller than 0.02, a linear interpolation is assumed, leading to the final result

$$\frac{\delta_s}{\delta_v} = 1 + 4.75 \left(\frac{r_b}{L_o}\right) , \quad \text{at} \quad \varphi = \pi/2 .$$

APPENDIX E

COMPARISON OF NORMALIZED MACH-NUMBER PROFILE FOR UNIFORM

FLOW AND SOURCE FLOW

In the development of the source-flow correction scheme for the viscous wake (Section 4.6), it was assumed that the distribution of the Mach-number ratio M/M_e was the same for both uniform flow and source flow. This condition, Eq. (4.27), was used in two instances: (1) in reducing Eq. (4.26) to the final result of Eq. (4.29) for wake-growth correction, and (2) in relating the uniform flow to the source flow in the correction for the magnitude of the Pitot pressure.[*] Although we cannot verify directly the accuracy of the assumed condition $(M/M_e)_s = (M/M_e)_u$, we can nevertheless demonstrate its plausibility on the basis of the results of some calculations pertaining to a related example.

The related problem may be stated as follows: We assume that at some initial longitudinal position, close to the wake neck, the distribution of M/M_e is the same for uniform flow and source flow, that is,

$$\left[\frac{M(\bar{r})}{M_e}\right]_{s,A} = \left[\frac{M(\bar{r})}{M_e}\right]_{u,A} , \quad \text{for } 0 \leq \bar{r} \leq 1 , \quad (E.1)$$

where $\bar{r}$ in this appendix denotes r/r_e and the subscript "A" refers to the initial station. This Mach-number distribution can be deduced from information that is considered given in the context of the present study. The problem then consists in showing that the similarity in the normalized Mach-number profile, Eq. (E.1), is preserved in the flow downstream of the initial station.

Some of the details of the foregoing related problem are now considered. For the initial station, we use station A with an x/d of 3.8, this being the nearest station studied experimentally. The Mach-number distribution $M_{s,A}(\bar{r})$ is deduced from the measured Pitot-pressure

---

[*] Specifically, this refers to step (5) on p. 65.

distribution $p'_{o_s}(\bar{r})$ and the static pressure $p_s(\bar{r}) \equiv p_s(r_e) = p_{e_s}$,
the last quantity being taken from the method-of-characteristics results
of Fig. 23.[*] The use of experimental data for the Pitot-pressure profile
ensures that the calculated Mach-number file has the proper distri-
bution, even though the magnitude may not necessarily be correct. Since
$M_{e_{s,A}}$ is by definition $M_{s,A}(1)$, the lefthand side of Eq. (E.1) is
now known. The Mach-number distribution for uniform flow $M_{u,A}(\bar{r})$ then
follows from Eq. (E.1) with the determination of $M_{e_{u,A}}$. This quantity
is deduced from the static and total pressures at the point $\bar{r} = 1$. The
distributions $M_{s,A}(\bar{r})$ and $M_{u,A}(\bar{r})$ thus calculated are listed in
columns (2) and (3), respectively, of the table at the end of this
appendix.

We now proceed downstream from the initial station and show that
the similarity in the distributions of the Mach-number ratio is preserved
for the range of longitudinal stations of interest. To establish this,
it is sufficient merely to show that the similarity holds at the most
distant station tested, that is, at station H with an x/d of 15.6.
To this end, we deduce independently both the uniform-flow and source-
flow distribution of the Mach-number ratio at station H. The distribution
$[M(\bar{r})/M_e]_{s,H}$ for the source-flow case can be calculated in a manner
similar to the corresponding distribution at station A, again using the
measured Pitot-pressure profile to ensure that the Mach-number distribution
adopted is realistic. As for deducing the uniform-flow distribution, we
note that at station H, the only quantity known thus far is the static
pressure from the method-of-characteristics results of Fig. 23. To
obtain the Mach-number information, a second pressure quantity is needed,
and for this we choose the total pressure. The distribution $p_{t_{u,H}}(\bar{r})$

---

[*] The fact that the wake static pressure (p_{2_e} in figure) is given
as the ratio p_{2_e}/p_{1_n} in this figure does not introduce any
difficulties. Since only pressure ratios are involved in the calcu-
lations, the quantity p_{1_n} cancels out in all cases.

can be calculated as follows. For each of the uses of uniform flow
and source flow at station A and of source flow at station H, the Mach-
number distribution and static pressure are known. It is thus possible
to calculate the respective total-pressure distributions, that is, the
distributions $p_{t_{u,A}}(\bar{r})$, $p_{t_{s,A}}(\bar{r})$, and $p_{t_{s,H}}(\bar{r})$. With the use of
Eq. (4.25) that relates these three quantities and $p_{t_{u,H}}(\bar{r})$, this
latter distribution can then be calculated. The required Mach-number
distribution $[M(\bar{r})/M_e]_{u,H}$ follows immediately from $p_{t_{u,H}}(\bar{r})$ and
$p_{e_{u,H}}$.

The distributions $M_{s,H}(\bar{r})$ and $M_{u,H}(\bar{r})$ calculated in the fore-
going are listed in columns (4) and (5) of the table, while the ratios
are given in columns (6) and (7). We see that whereas the Mach number
itself differs considerably for uniform flow and source flow, the ratios
differ only slightly for the two cases. From this the conclusion can
be drawn that the similarity of the distributions of Mach-number ratio
is indeed preserved in the flow downstream of the initial station.
Strictly speaking, this conclusion applies only to the related problem
that uses Eq. (E.1) as the starting point. The result does not provide
direct proof for the assumption $(M/M_e)_s = (M/M_e)_u$ throughout the entire
viscous wake. We note, however, that the basic assumption of the related
problem, Eq. (E.1), is itself in line with the results of calculations
pertaining to the development of the boundary layer. It was shown in
Appendix D, Fig. 41, that the temperature ratio T/T_{ex} did not differ
significantly for uniform flow and source flow. This implies that the
difference in the Mach-number ratio M/M_e is even smaller, thereby
justifying the assumption of Eq. (E.1). On this basis, it appears
reasonable to use the result of the related problem to substantiate the
assumption $(M/M_e)_s = (M/M_e)_u$ of Section 4.6.

107

$\bar{r} = r/r_e$	$M_{s,A}$	$M_{u,A}$	$M_{s,H}$	$M_{u,H}$	$[M/M_e]_{s,H}$	$[M/M_e]_{u,H}$
(1)	(2)	(3)	(4)	(5)	(6)	(7)
0	2.42	2.34	3.55	3.07	.711	.700
.1	2.44	2.36	3.61	3.12	.723	.711
.2	2.49	2.41	3.77	3.28	.755	.749
.3	2.58	2.50	3.96	3.46	.793	.789
.4	2.69	2.61	4.14	3.62	.829	.825
.5	2.82	2.73	4.33	3.79	.868	.864
.6	2.97	2.88	4.48	3.93	.897	.896
.7	3.11	3.01	4.63	4.06	.927	.926
.8	3.26	3.15	4.76	4.17	.954	.951
.9	3.40	3.29	4.88	4.29	.977	.977
1.0	3.53	3.42	4.99	4.39	1	1

REFERENCES

Alligood, B. T., J. B. Kyser, and D. W. Tsao, 1963, A traversing probe for Pitot-pressure mapping in a hypersonic tunnel. Stanford University, SUDAER no. 170.

Baradell, D. L., and M. H. Bertram, 1960, The blunt flat plate in hypersonic flow. NASA, TN D-408.

Berndt, S. B., 1962, On the influence of the non-uniform free-stream of a conical wind-tunnel nozzle on the axisymmetric hypersonic flow around blunt bodies. Natl. Res. Council of Canada, Aero. Rept. LR-338.

Bomelburg, H. J., 1958, A method for the measurement of the flow of air by means of series of electric sparks. Air Force Office of Scientific Res., OSR-TN-56-38.

Burke, A. F., and K. D. Bird, 1962, The use of conical and contoured expansion nozzles in hypervelocity facilities; in Advances in Hypervelocity Techniques, ed. by A. M. Krill, Plenum Press.

Chapman, S., and T. G. Cowling, 1952, The Mathematical Theory of Non-Uniform Gases, Cambridge Univ. Press.

Cheng, H. K., 1960, Hypersonic flow with combined leading-edge bluntness and boundary-layer displacement effect. Cornell Aero. Lab., Rept. no. AF-1285-A-4.

Chironis, N., 1961, Spring Design and Application, McGraw-Hill.

Clark, R. N., 1962, Introduction to Automatic Control Systems, Wiley.

Cohen, C. B., and E. Reshotko, 1956, Similar solutions for the compressible laminar boundary layer with heat transfer and pressure gradient. NACA, Report 1293.

Cole, J. D., 1957, Newtonian flow theory for slender bodies. J. Aero. Sci., vol. 24, p. 448.

Demetriades, A., and A. B. Bauer, 1966, Supersonic wind tunnel experiments with axisymmetric wakes. AIAA Paper, Preprint no. 66-453.

Denison, M. R., and E. Baum, 1963, Compressible free shear layer with finite initial thickness. AIAA Journal, vol. 1, no. 2, p. 342.

Eaves, R. H., Jr., and C. H. Lewis, 1965, Combined effects of viscous interaction and ideal source flow on pressure and heat-transfer distributions over hemisphere cylinders at $M_\infty \sim 18$. Arnold Engr. Devel. Center, AEDC-TR-65-158.

Feldman, S., 1960, Numerical comparison between exact and approximate theories of hypersonic inviscid flow past slender blunt nosed bodies. ARS Journal, vol. 30, p. 463.

Feldman, S., 1961, On trails of axisymmetric hypersonic blunt bodies flying through the atmosphere. J. Aero. Sci., vol. 28, no. 6, p. 433.

Grabau, M., R. L. Humphrey, and W. L. Little, 1961, Determination of test-section, after-shock, and stagnation conditions in Hotshot tunnels using real nitrogen at temperatures from 3000 to 4000°K. Arnold Engr. Devel. Center, AEDC-TN-61-82.

Hall, J. G., 1963, Effects of ambient nonuniformities in flow over hypersonic test bodies. Cornell Aero. Lab., Rept. no. 128.

Henrici, P., 1964. Elements of Numerical Analysis, Wiley.

Hildebrand, F. B., 1956, Introduction to Numerical Analysis, McGraw-Hill.

Inouye, M., 1966a, Numerical solutions for blunt axisymmetric bodies in a supersonic spherical source flow. NASA, TN D-3383.

Inouye, M., 1966b, Unpublished results.

Jury, E. I., 1964, Theory and Application of the z-Transform Method, Wiley.

Karamcheti, K., W. Vali, and W. G. Vincenti, 1961, Initial experience in the Stanford spark-heated hypervelocity wind tunnel. Stanford University, SUDAER no. 100.

Kuo, B. C., 1963, Analysis and Synthesis of Sampled-Data Control Systems, Prentice-Hall.

Kyser, J. B., 1964, Tracer-spark technique for velocity mapping of hypersonic flow fields. AIAA Journal, vol. 2, no. 2, p. 393.

Kyser, J. B., 1967, Additional study and further development of the tracer-spark technique for flow-velocity measurements. NASA, CR-760.

Lees, L., 1956, Laminar heat transfer over blunt-nosed bodies at hypersonic flight speeds. Jet Propulsion, vol. 26, no. 4, p. 259.

Lees, L., and L. Hromas, 1962, Turbulent diffusion in the wake of a blunt-nosed body at hypersonic speeds. J. Aero. Sci., vol. 29, no. 8, p. 976.

Liepmann, H. W., and A. Roshko, 1957, Elements of Gas Dynamics, Wiley

Lukasiewicz, J., 1961, Hypersonic flow-blast theory. Arnold Engr. Devel. Center, AEDC-TR-61-4.

Lykoudis, P. S., 1963, The growth of the hypersonic turbulent wake behind blunt and slender bodies. Rand Corp., RM-3270-PR.

Lykoudis, P. S., 1966, A review of hypersonic wake studies. AIAA Journal, vol. 4, no. 4, p. 577.

McCarthy, J. F., Jr., 1962, Hypersonic wakes. Grad. Aero. Lab. Calif. Inst. Tech., Memorandum no. 67.

Meyer, R. F., 1963, The blast wave analogy for a hypersonic source flow. Natl. Res. Council of Canada, Aero. Rept. LR-368.

Moore, F. K., 1964, Theory of Laminar Flows, ed. by F. K. Moore, Princeton University Press.

Ragazzini, J. R., and G. F. Franklin, 1958, Sampled-Data Control Systems, McGraw-Hill.

Rasmussen, M. L., and K. Karamcheti, 1966, Viscous effects far downstream in a slowly expanding hypersonic nozzle. AIAA Journal, vol. 4, no. 5, p. 807.

Reeves, B. L., and L. Lees, 1965, Theory of laminar near wake of blunt bodies in hypersonic flow. AIAA Journal, vol. 3, no. 11, p. 2061.

Sakurai, A., 1953, On the propagation and structure of the blast wave, I. J. Phys. Soc. Japan, vol. 8, no. 5, p. 662.

Sakurai, A., 1954, On the propagation and structure of a blast wave, II. J. Phys. Soc. Japan, vol. 9, no. 2, p. 256.

Savage, S. B., 1966, Effects of a source-type hypersonic free stream on the flow field about an axisymmetric cone. Aero. Quarterly, vol. XVII, part 2, p. 161.

Schlichting, H., 1960, Boundary Layer Theory, McGraw-Hill.

Smith, C. E., Jr., 1962, Thermodynamic properties of nitrogen. Lockheed Missiles and Space Co., Rept. no. 6-90-62-111.

Smith, C. E., R. L. Kramer, and A. C. Brown, 1966, A study of the laminar near-wake behind a cylinder at Mach 20. AIAA Journal, vol. 4, no. 7, p. 1187.

Smotherman, W. E., 1960, A miniature wafer-style pressure transducer. Arnold Engr. Devel. Center, AEDC-TR-60-11.

Smotherman, W. E., and W. V. Maddox, 1963, Variable reluctance pressure transducer development. Arnold Engr. Devel. Center, AEDC-TDR-63-135.

Van Dyke, M. D., 1958, The supersonic blunt-body problem — review and extension. J. Aero. Sci., vol. 25, no. 8, p. 485.

Van Hise, V., 1961, Analytic study of induced pressure on long bodies of revolution with varying nose bluntness at hypersonic speeds.   NASA, Tech. Rept. R-78.

Vas, I. E., E. M. Murman, and S. M. Bogdonoff, 1965, Studies of wakes of support-free spheres at M = 16 in helium.   AIAA Journal, vol. 3, no. 7, p. 1237.

Whitfield, J. D., and G. D. Norfleet, 1962, Source flow effects in conical hypervelocity nozzles.   Arnold Engr. Devel. Center, AEDC-TDR-62-116.
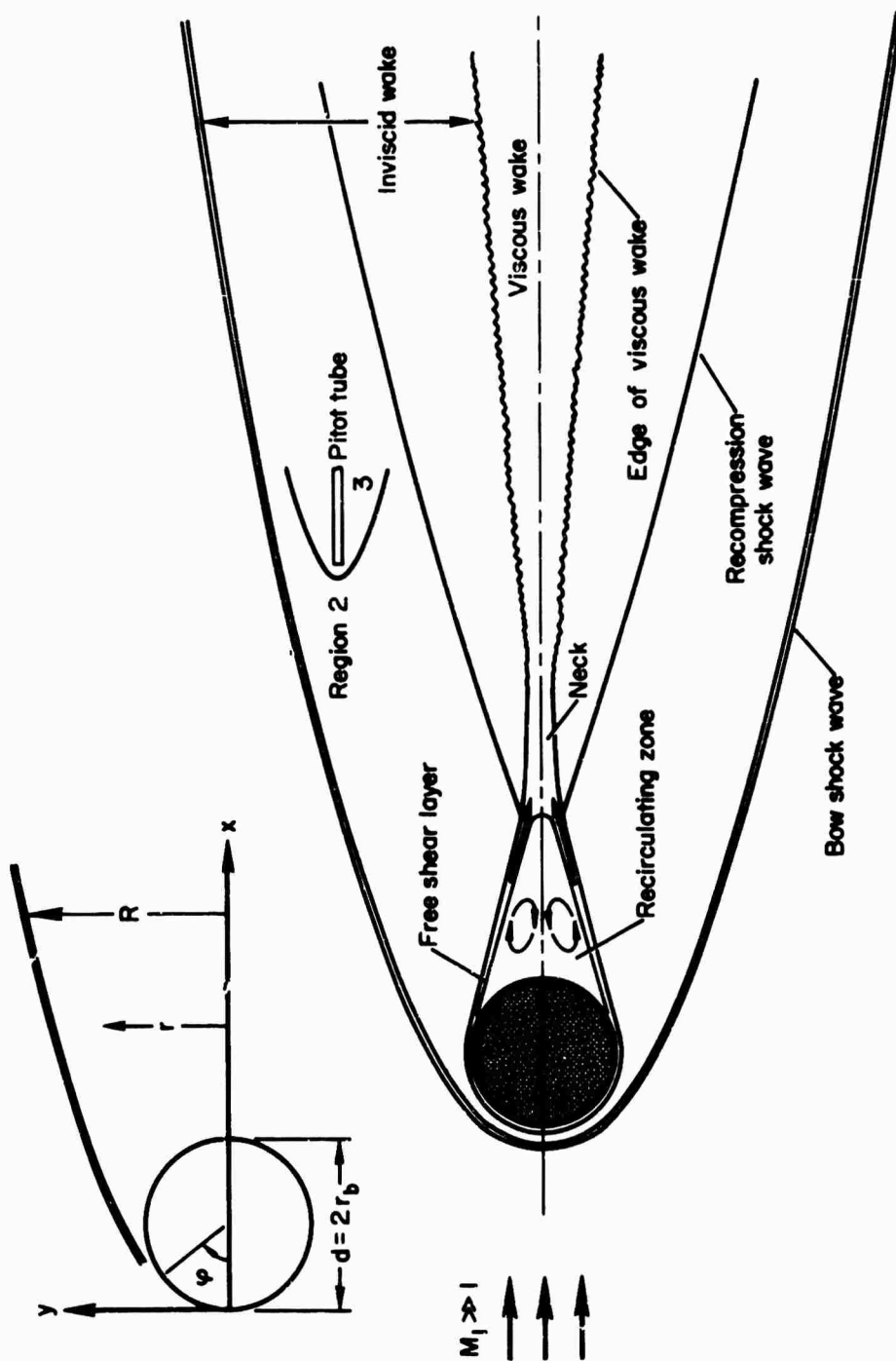
Figure 1. The wake behind a sphere in hypervelocity flow.

113
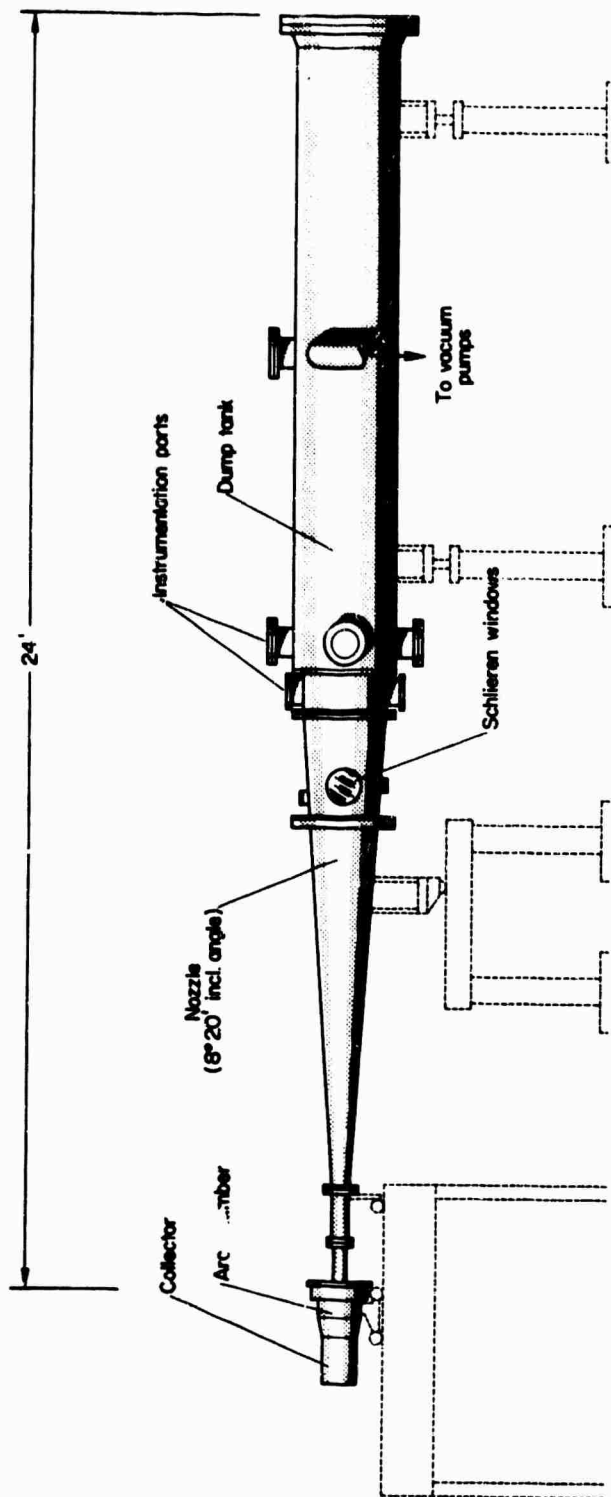
Figure 2. Tunnel schematic diagram.

114

Station	x, in.	x/d
A	7.6	3.8
B	10.2	5.1
C	13.2	6.6
D	16.2	8.1
E	19.2	9.6
F	22.2	11.1
G	25.2	12.6
H	31.2	15.6
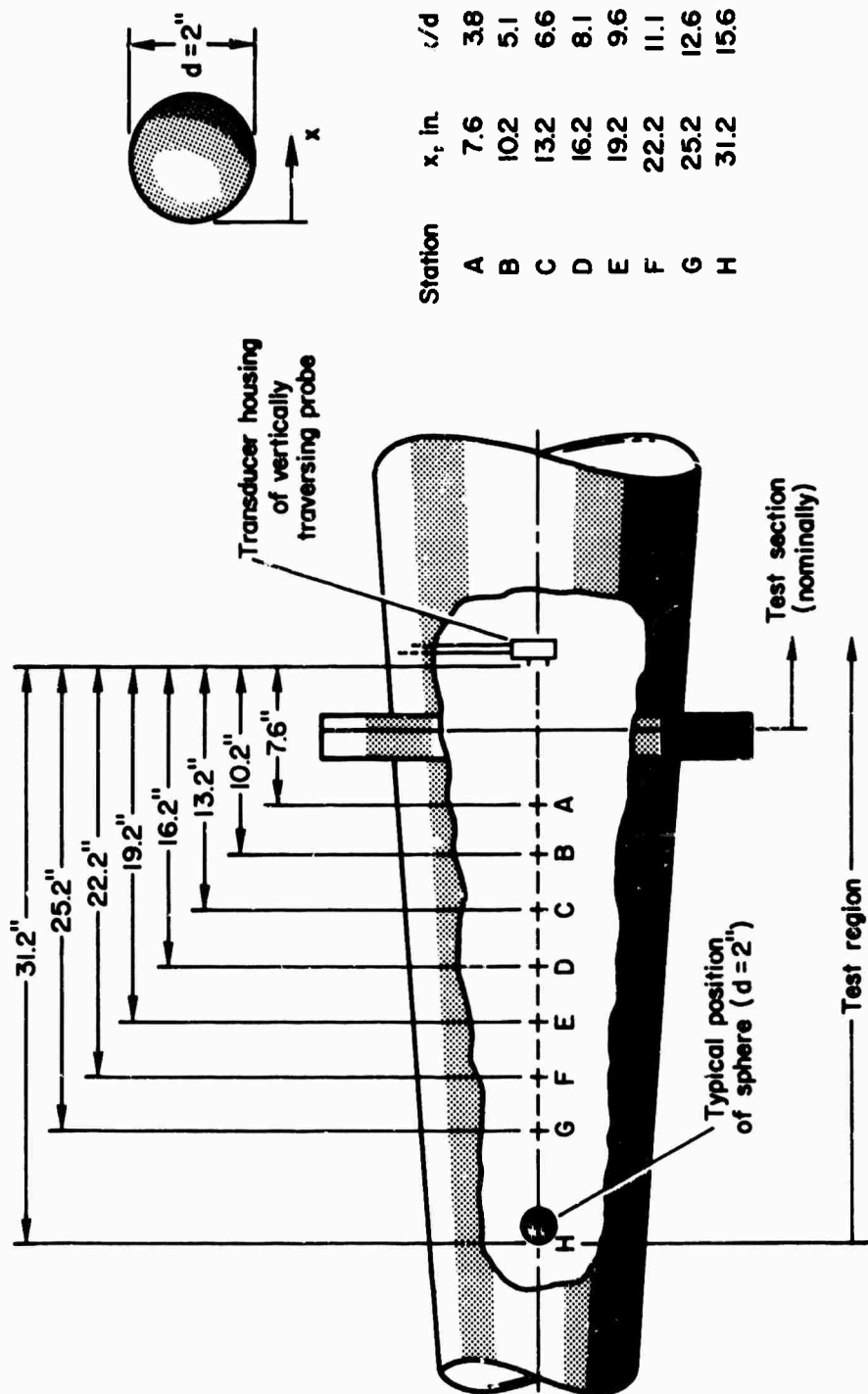
Figure 3.   Test stations.

115

(a) Sphere suspension.

(b) Side view of system for accelerating mass (loaded position).

Figure 4. Sphere suspension and release mechanisms.

116
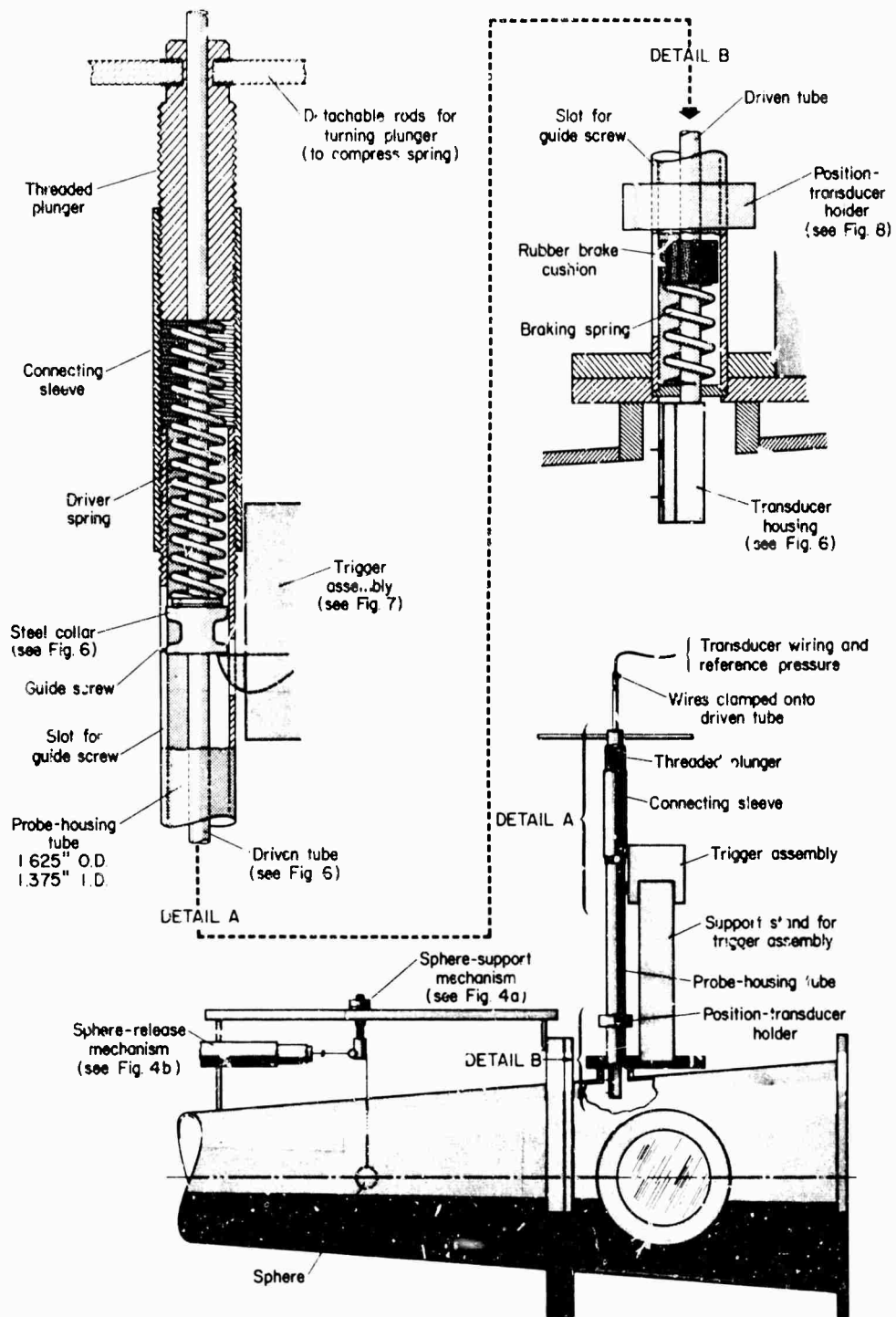
Figure 5. Vertically transversing probe (in loaded position) mounted on tunnel test section.

A-A
STEEL-COLLAR DETAIL

TRANSDUCER-HOUSING DETAIL
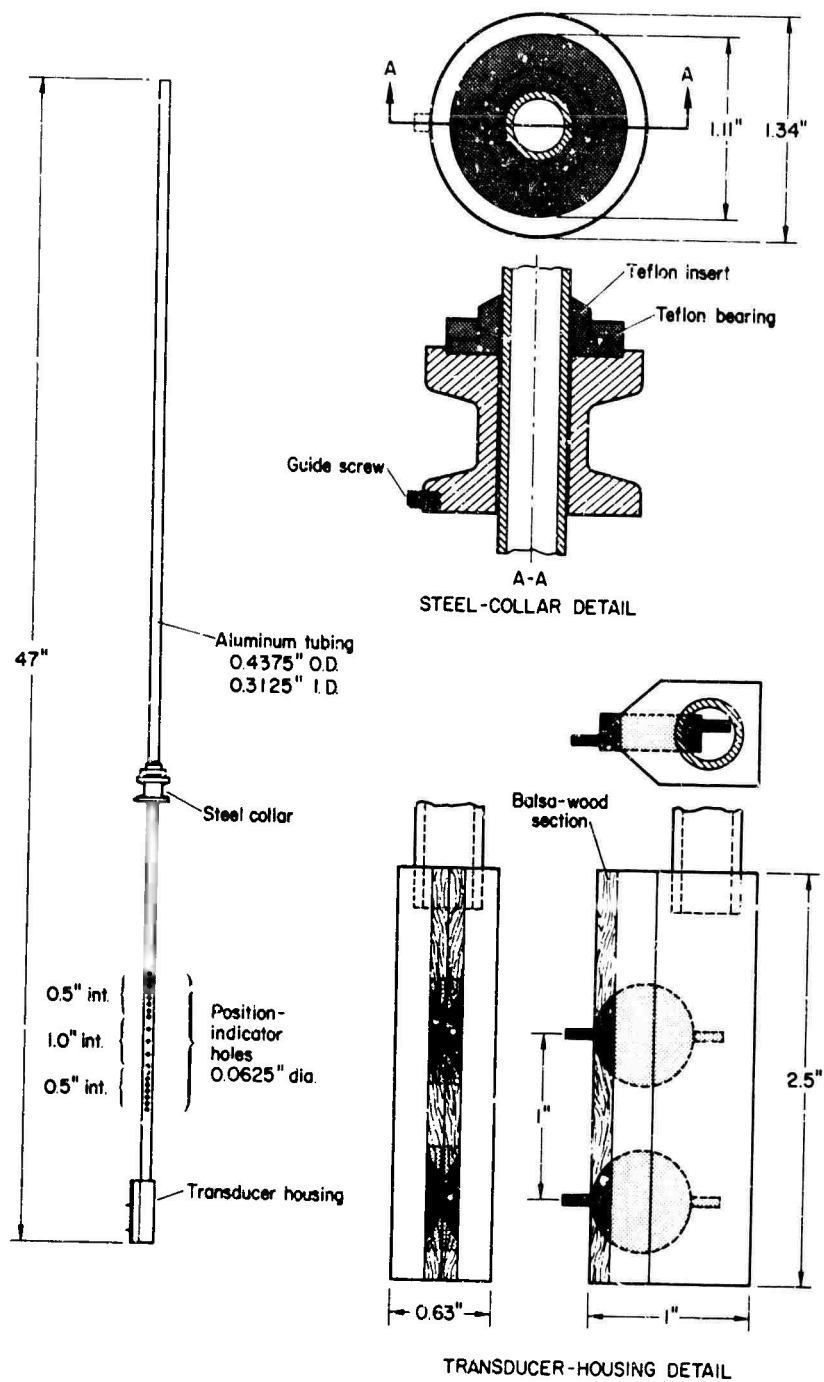
Figure 6.   Driven portion of vertically traversing probe.

118

2.3"

Front plate removed in side view

Top view

5.0"

Probe

5.0"

Cam

Ledex solenoid

Side view
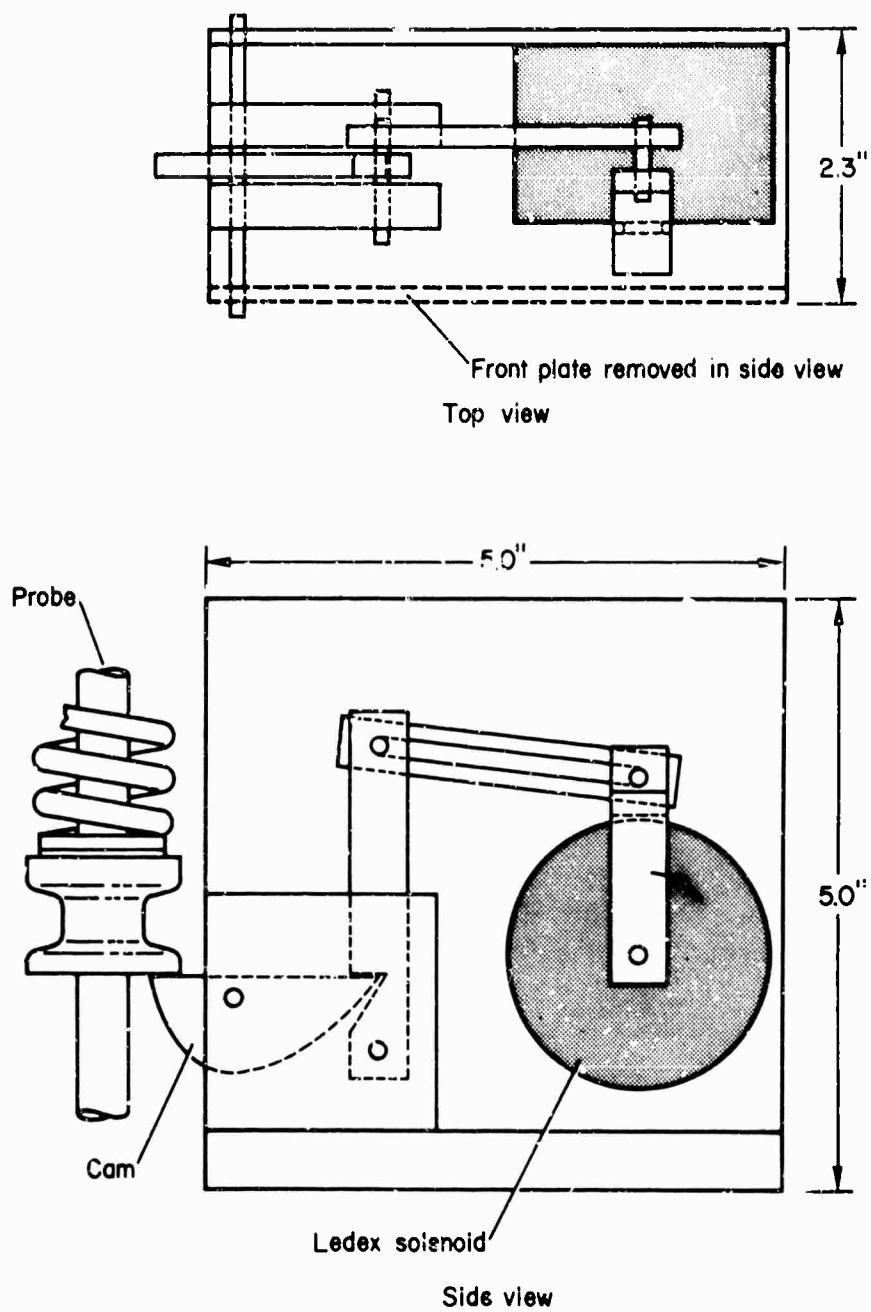
Figure 7.   Trigger assembly.

119

45 Vdc

Photocell

5.0 M

1.0 M

To oscilloscope

dc amplifier

To oscilloscope

Oscillograph

(b) Photocell circuit.

Tunnel longitudinal axis

Setscrews hold ring in place

Brass probe housing 1.675" O.D.

Aluminum ring 2.875" O.D.

A

A

Light

Idealized light path

Lucite rod

Photocell

A-A
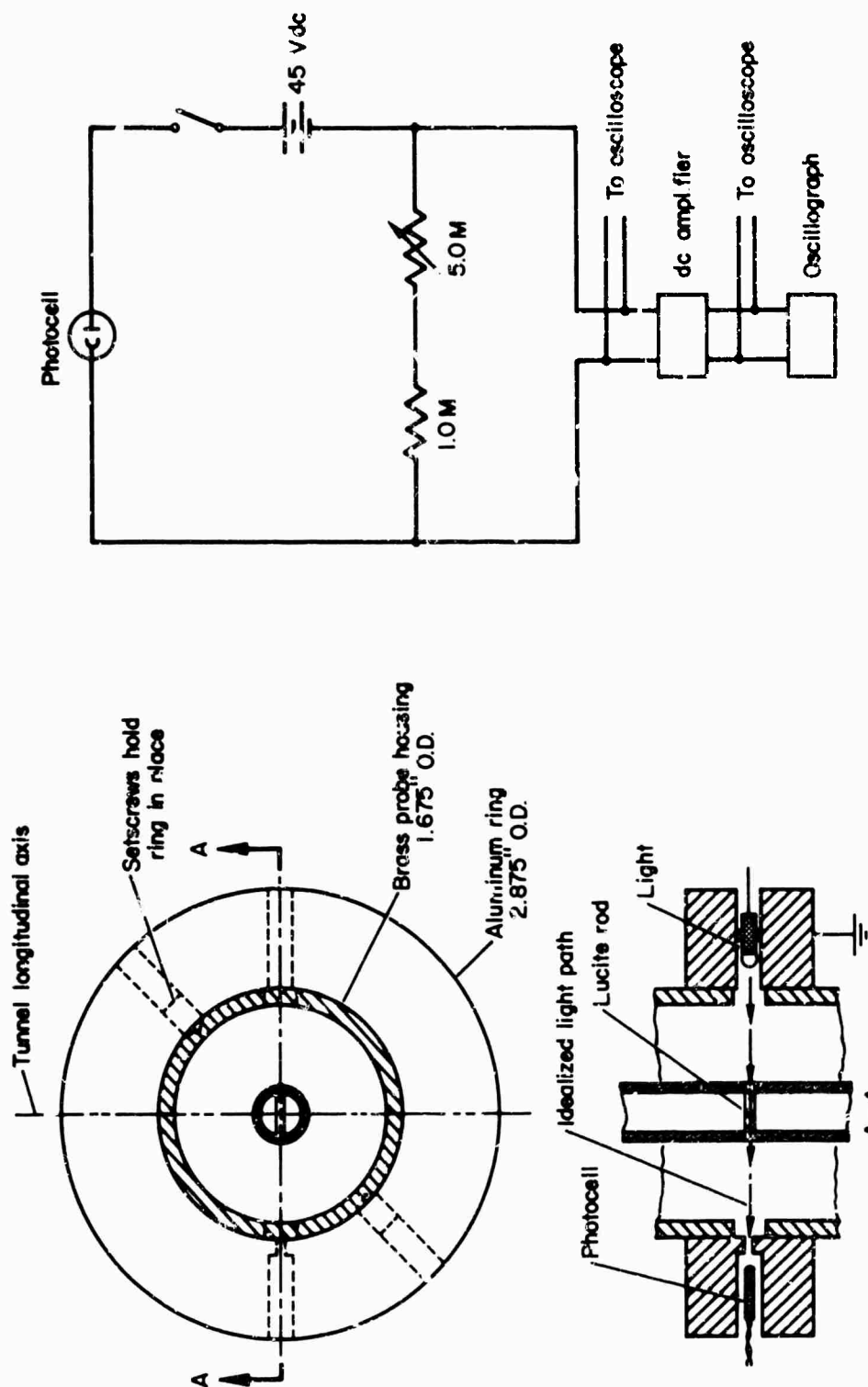
(a) Schematic diagram.

Figure 8.   Position transducer.

120
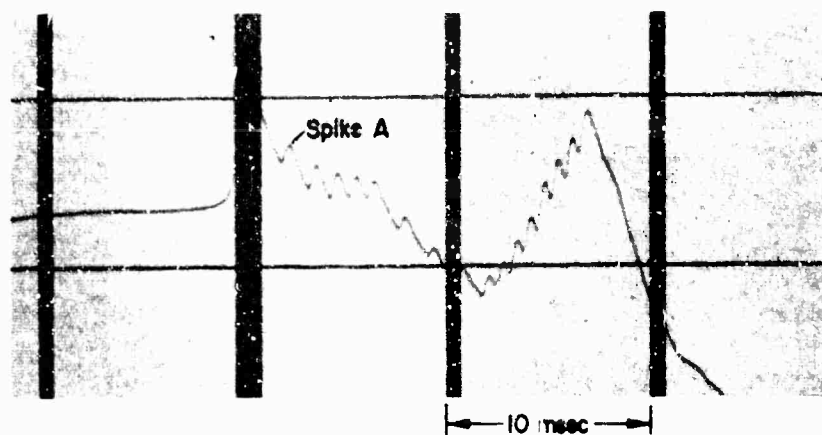
(a) Photocell output.
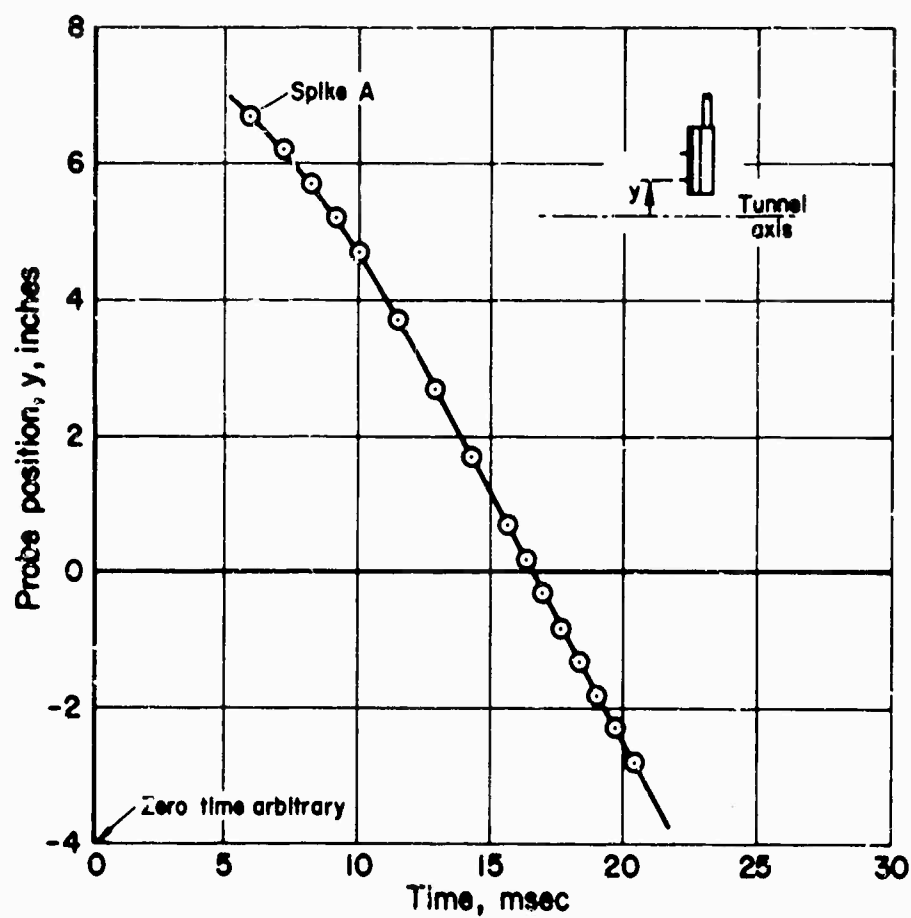
(b) Time-position plot.

Figure 9.   Time history of probe position.
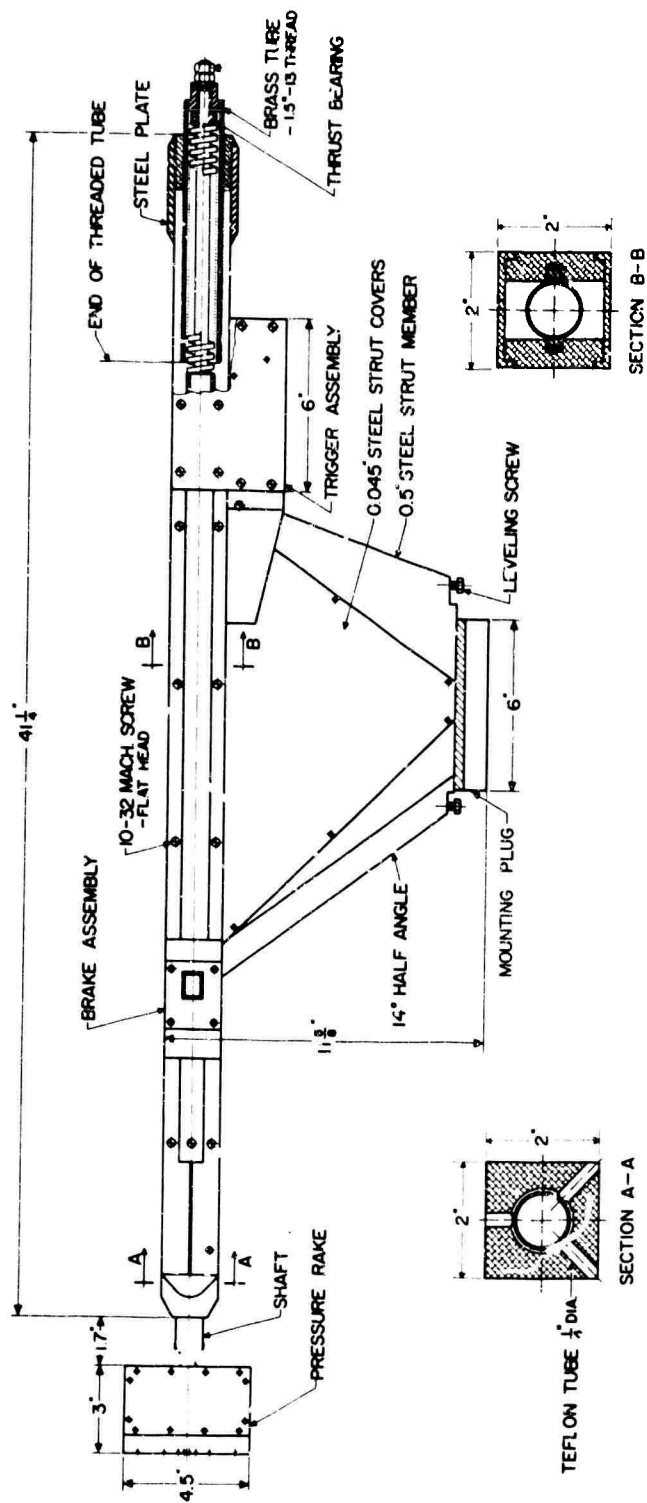
Figure IO. Axially traversing probe and mounting strut.
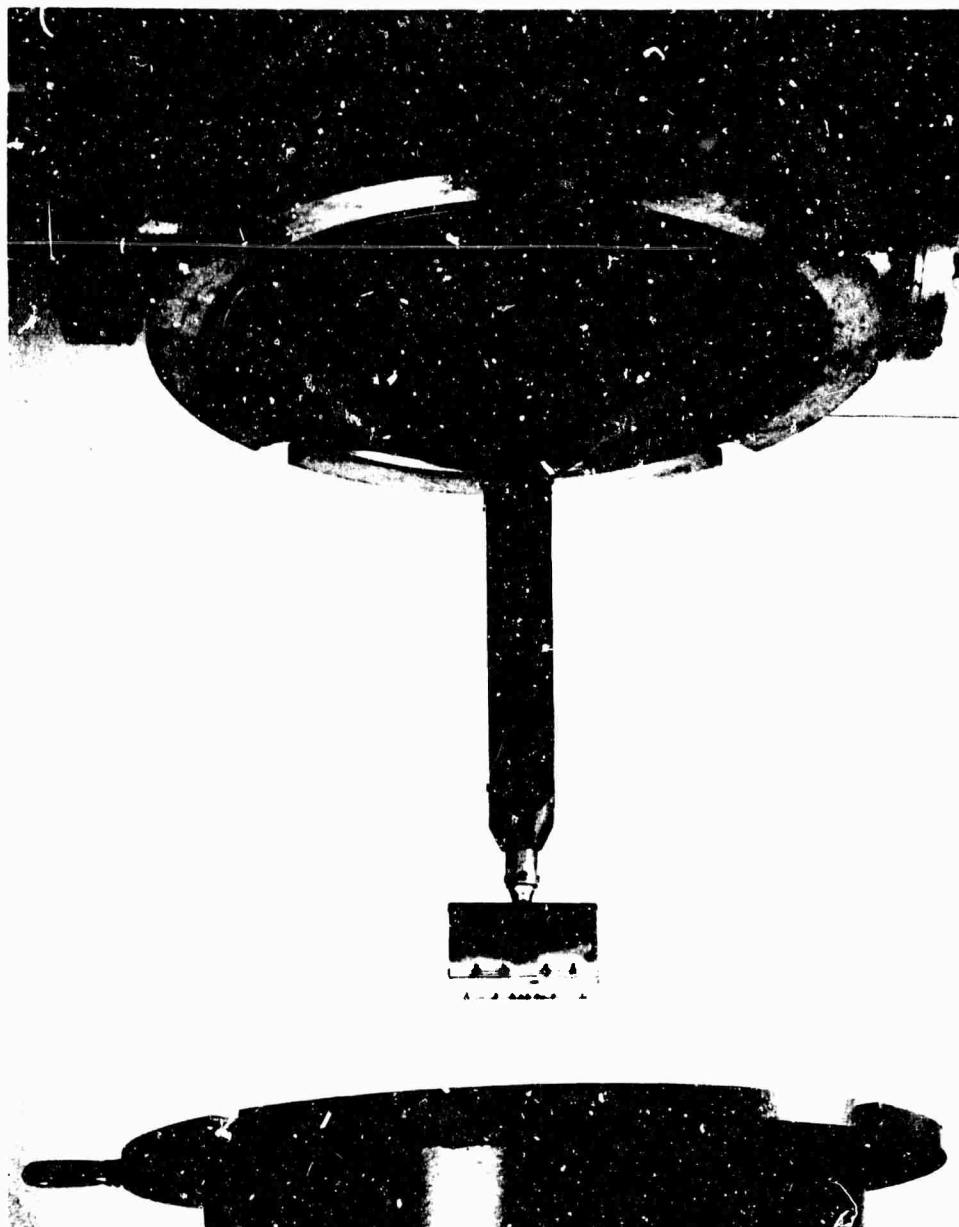
Figure 11. Axially traversing probe mounted in tunnel.

Pitot tubes
0.038" O.D.
0.034" I.D.

3.625"

0.125"

4.000"

Four tubes on 0.188" dia. circle

1.469"

0.844"

1.594"

0.938"

0.250"

0.250"

1.281"

1.094"

1.750"

1.969"
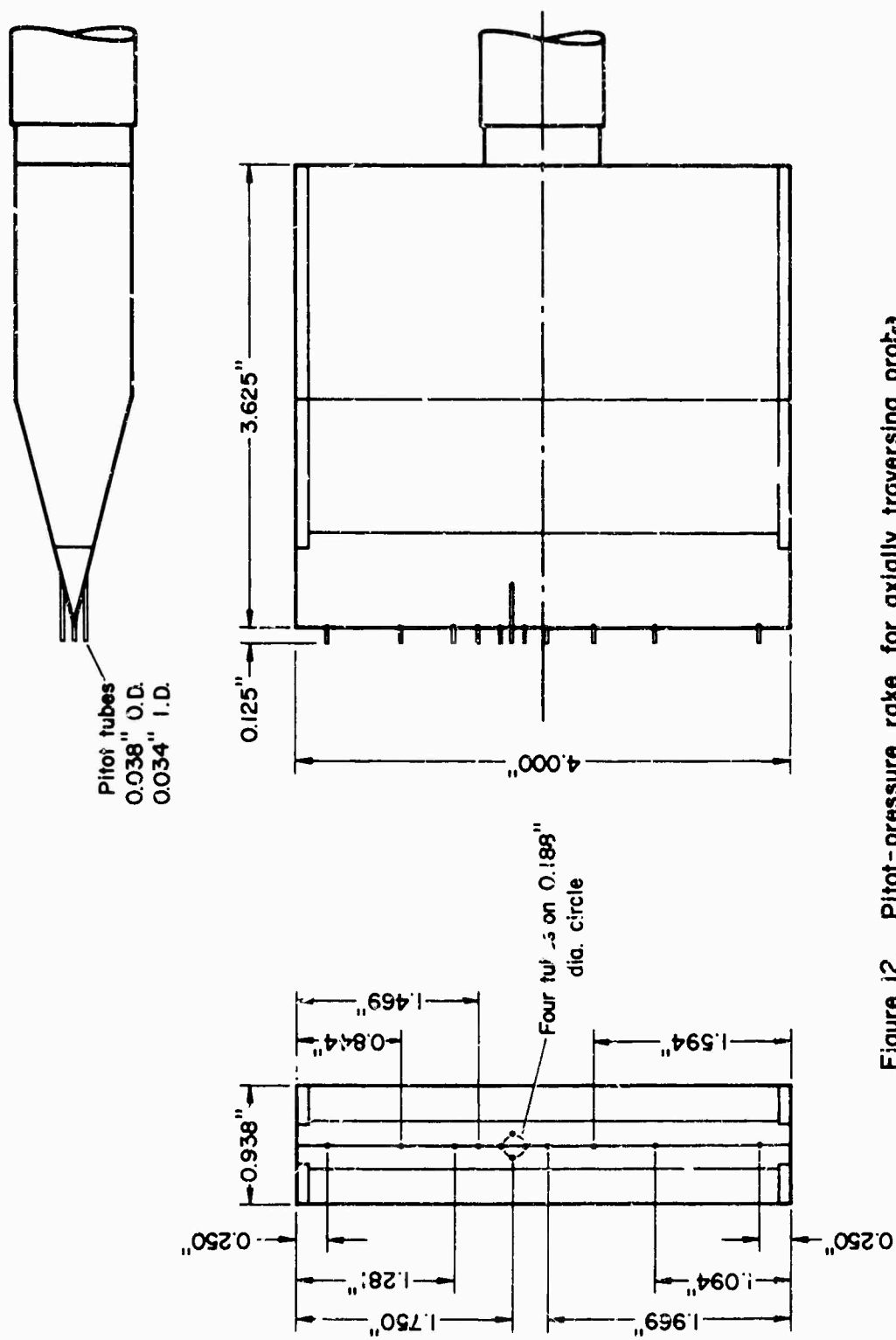
Figure 12.   Pitot-pressure rake for axially traversing probe.

124

(a) System for continuous signals.
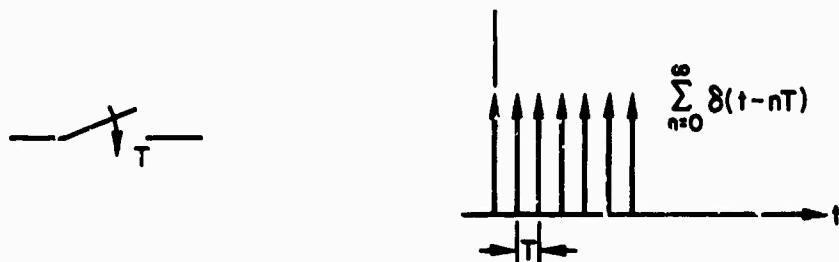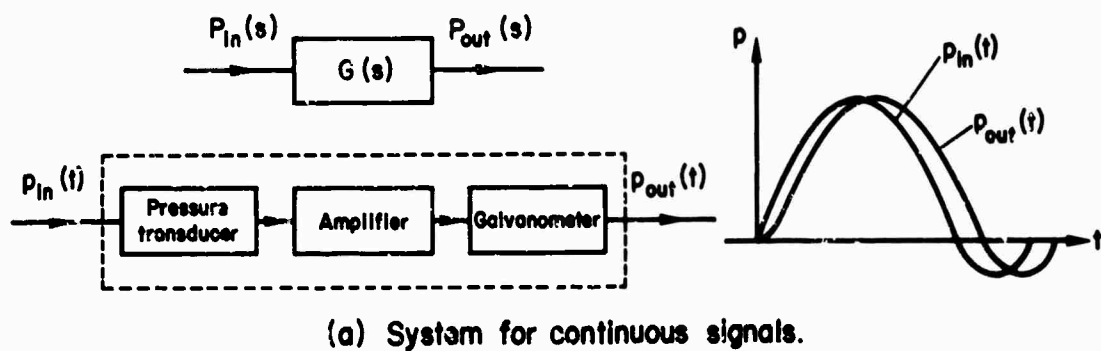
(b) Ideal input sampler and representation by unit-impulse train.

(c) Sampled-data system.
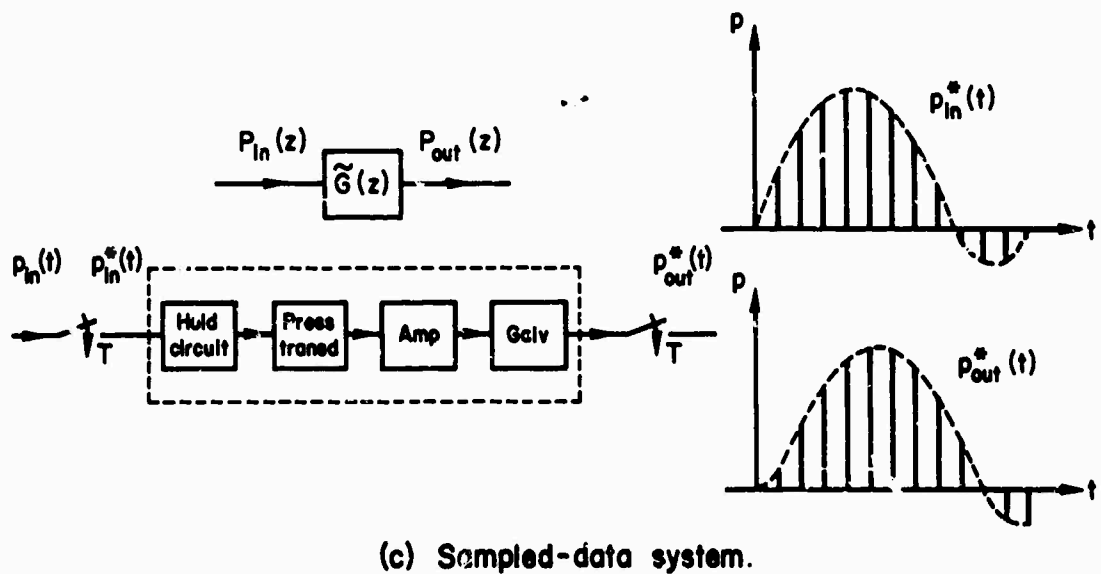
Figure 13.   The transducer-galvanometer system as a sampled-data control system.

125
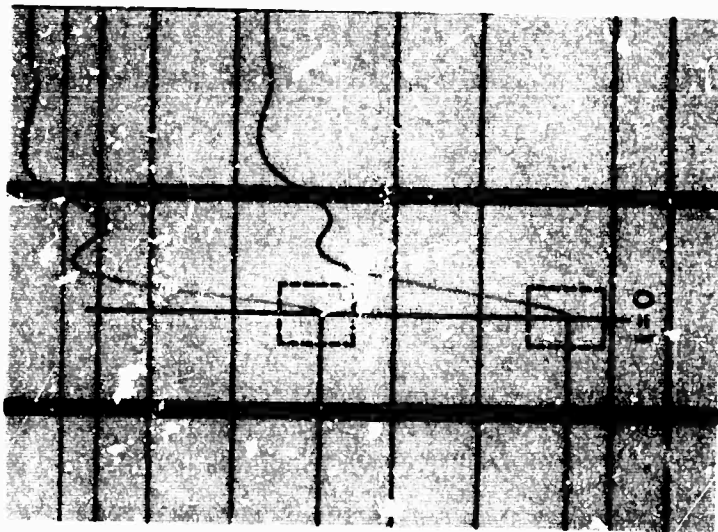
(a) Galvanometer output (two transducers).
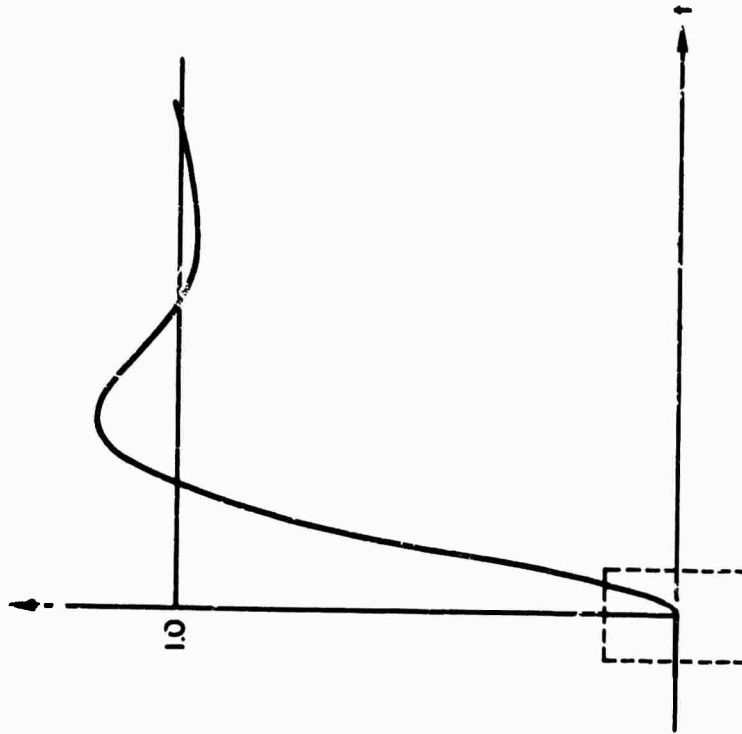
(b) Normalized output of second-order system.

Figure i4.   Comparison of galvanometer output with output of second-order system.
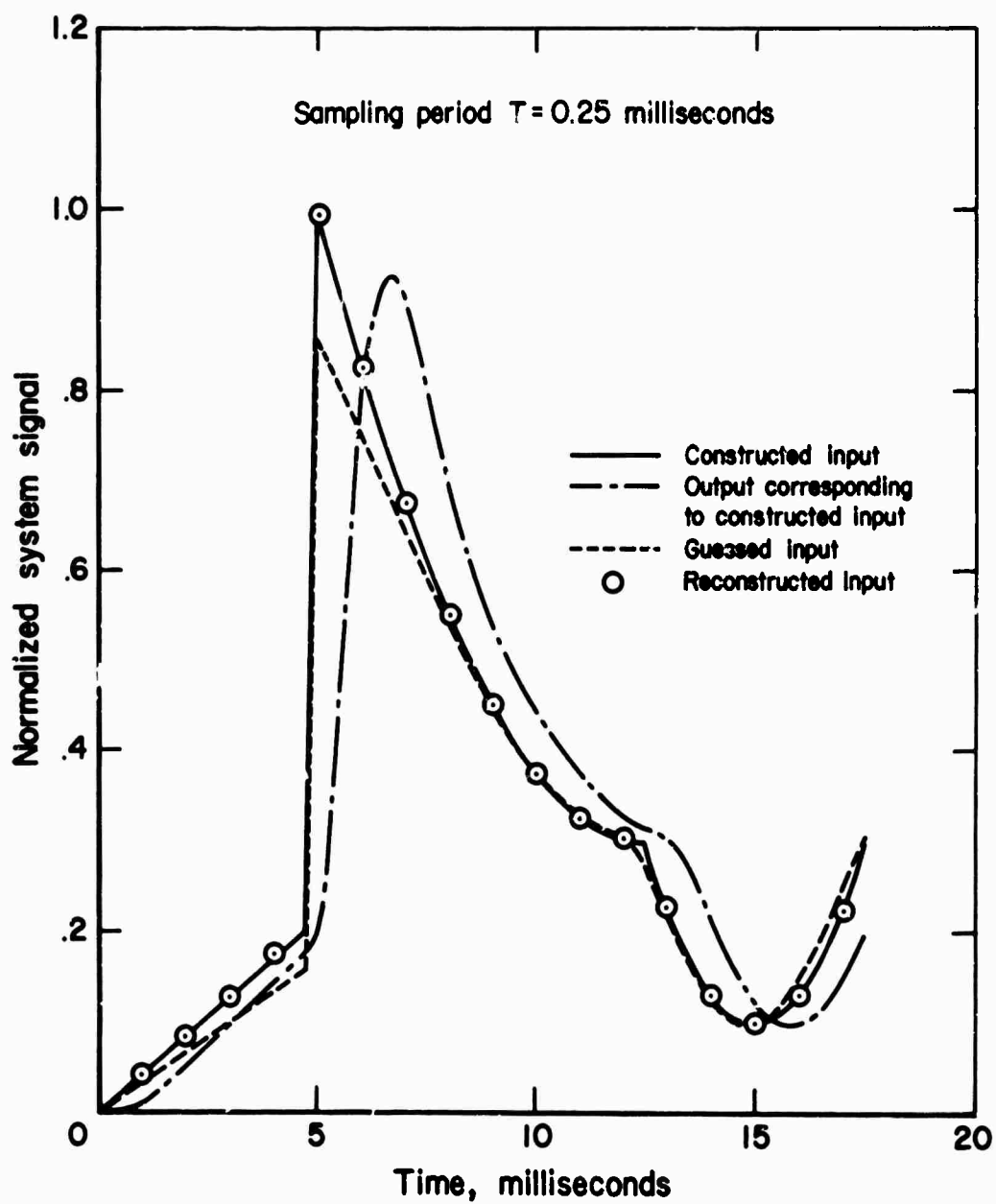
Figure 15. Comparison of reconstructed input with given (constructed) input.

127
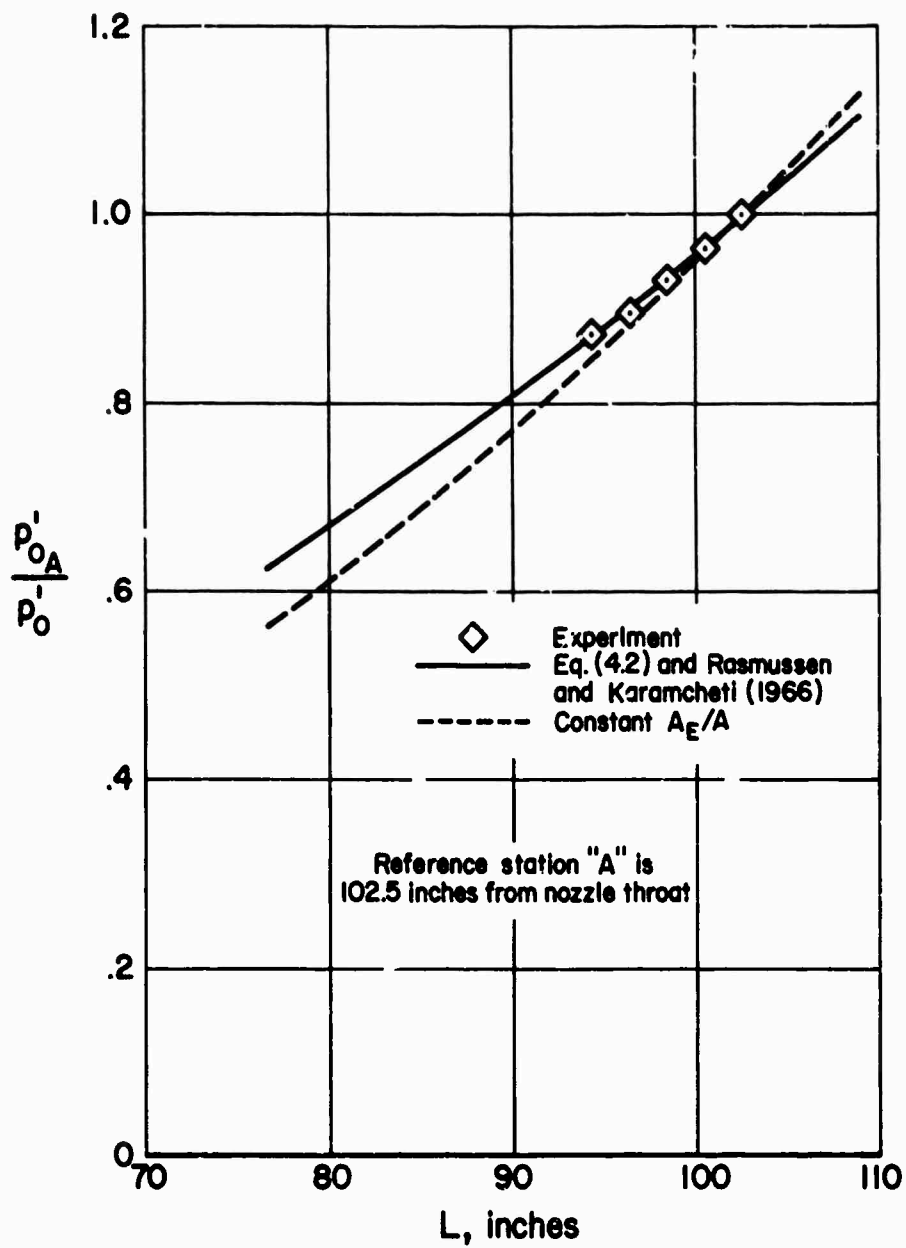
Figure 16. Longitudinal Pitot-pressure variation in
the tunnel free stream.
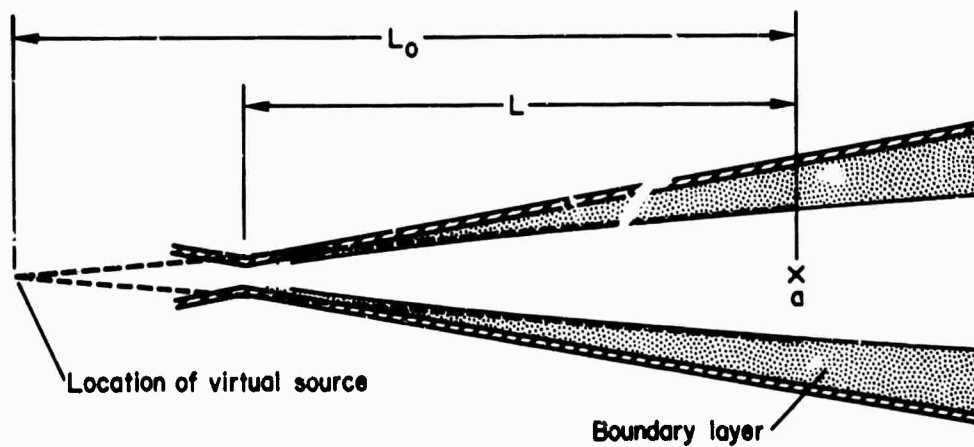
(a) Virtual-source representation.
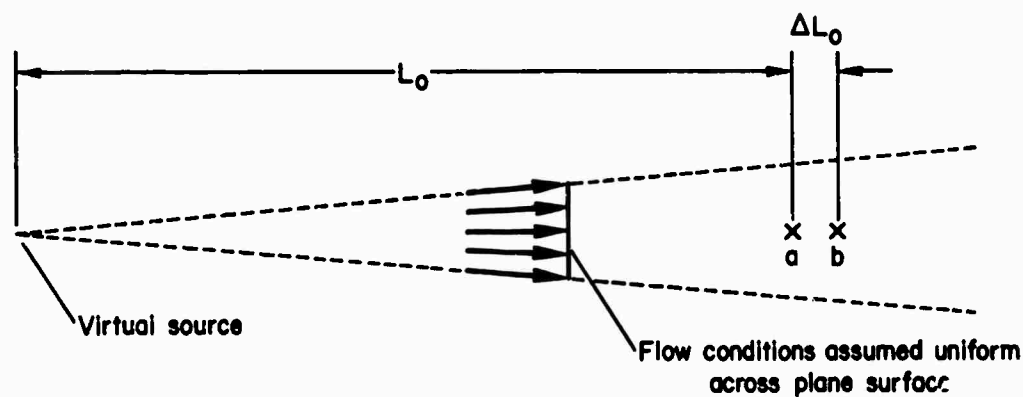
(b) One-dimensional approximation of flow from virtual source.

Figure 17.   Virtual-source representation of contouring effect of boundary layer.
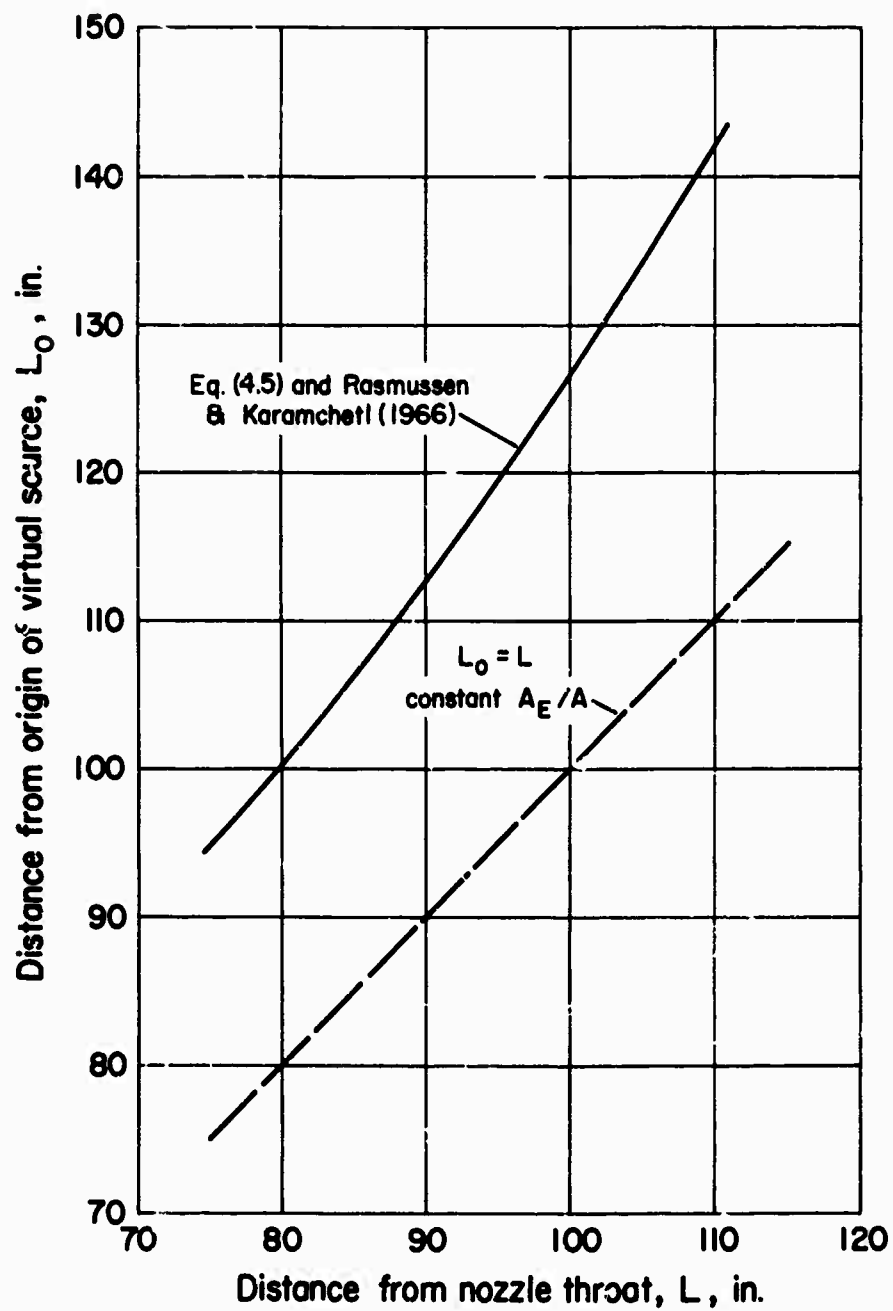
Figure 18. Location of virtual source.

130
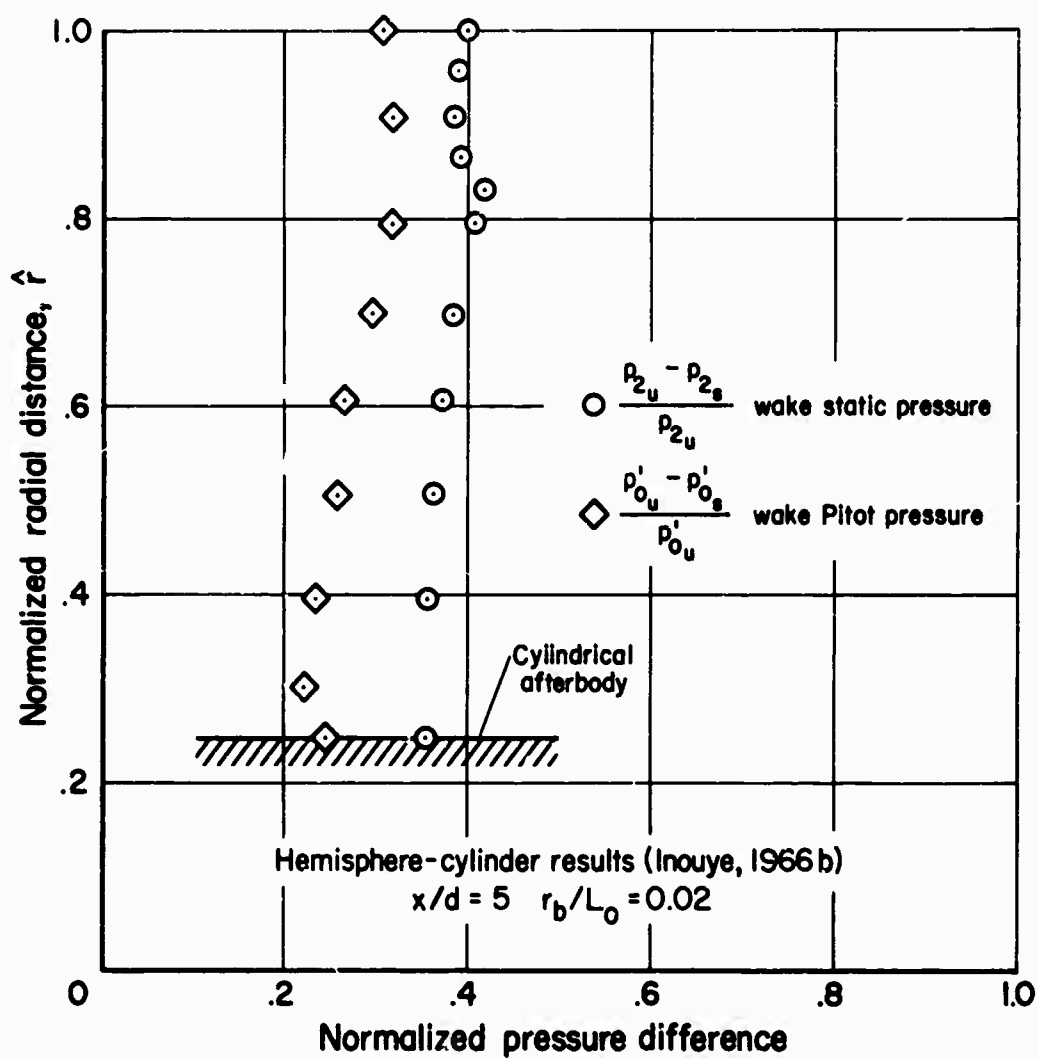
Figure 19.   Radial distribution of pressure difference
due to source-flow effects.
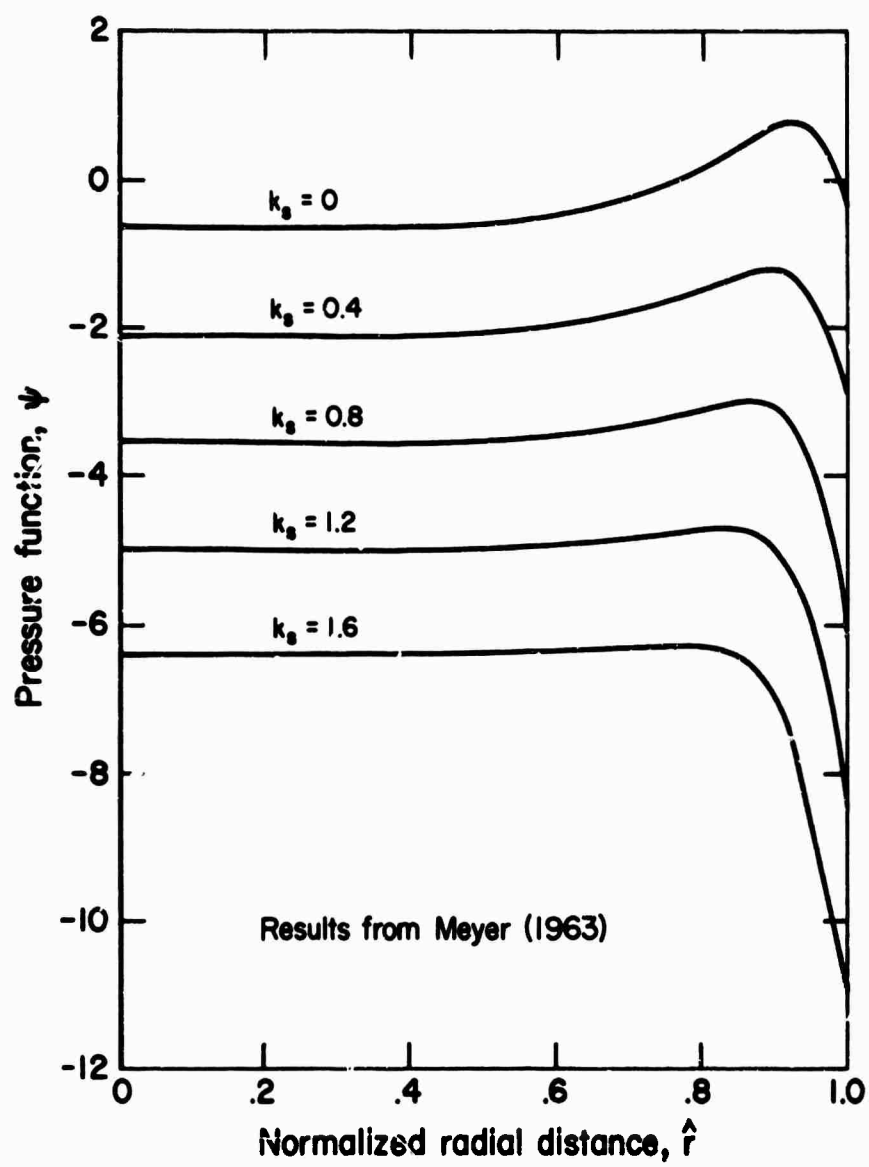
Figure 20.   Pressure function ψ from blast-wave theory.
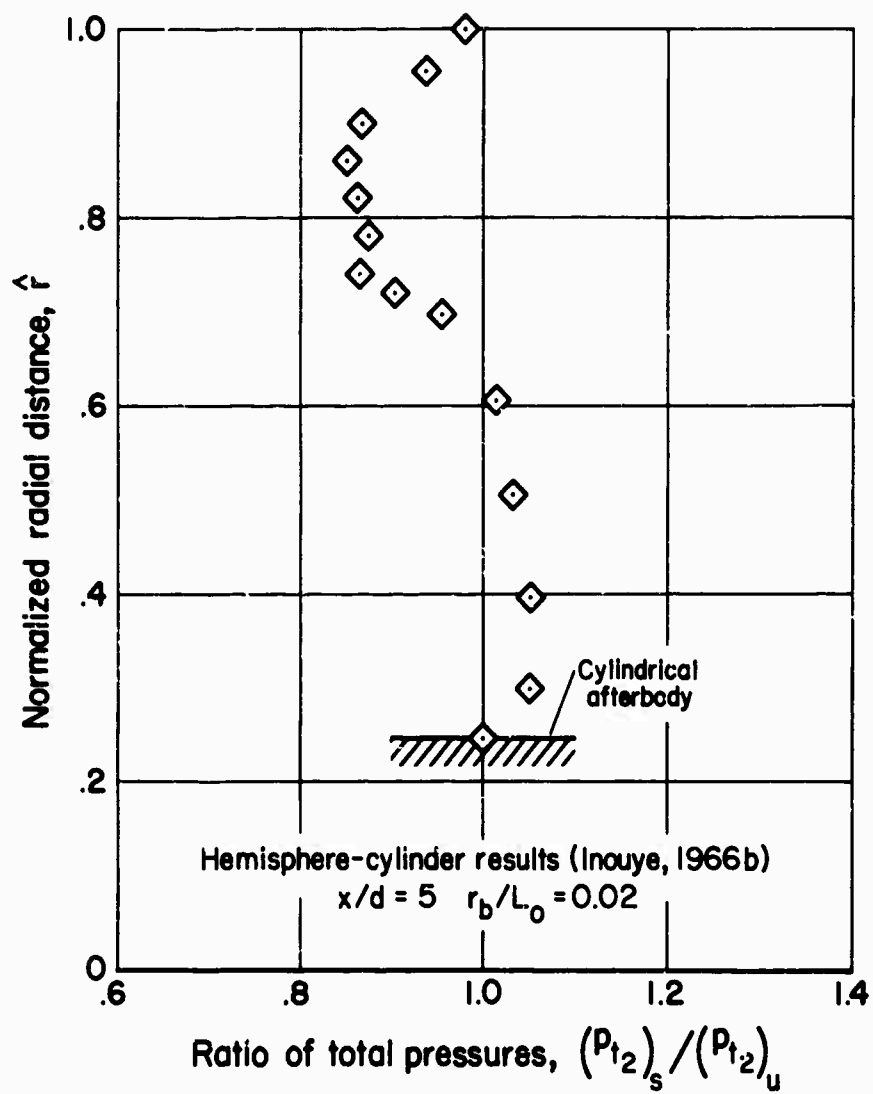
Figure 21. Radial distribution of total-pressure ratio.
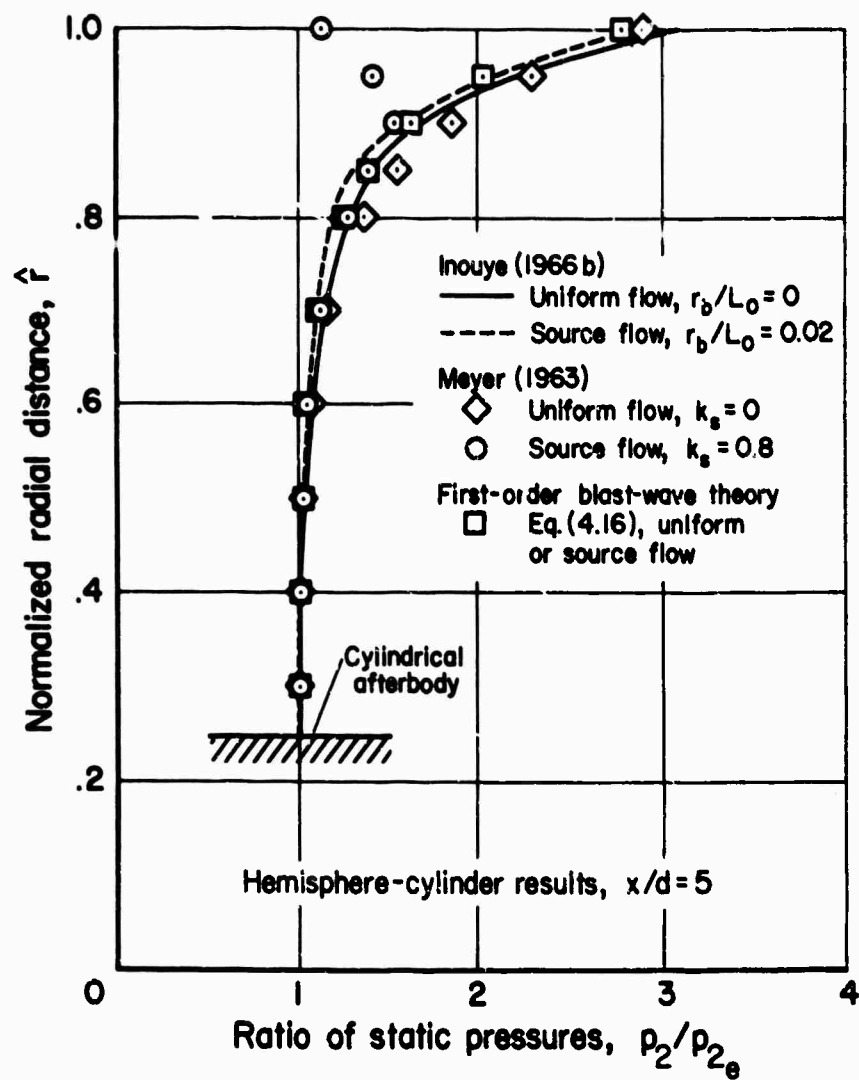
Figure 22. Radial distribution of static-pressure ratio.
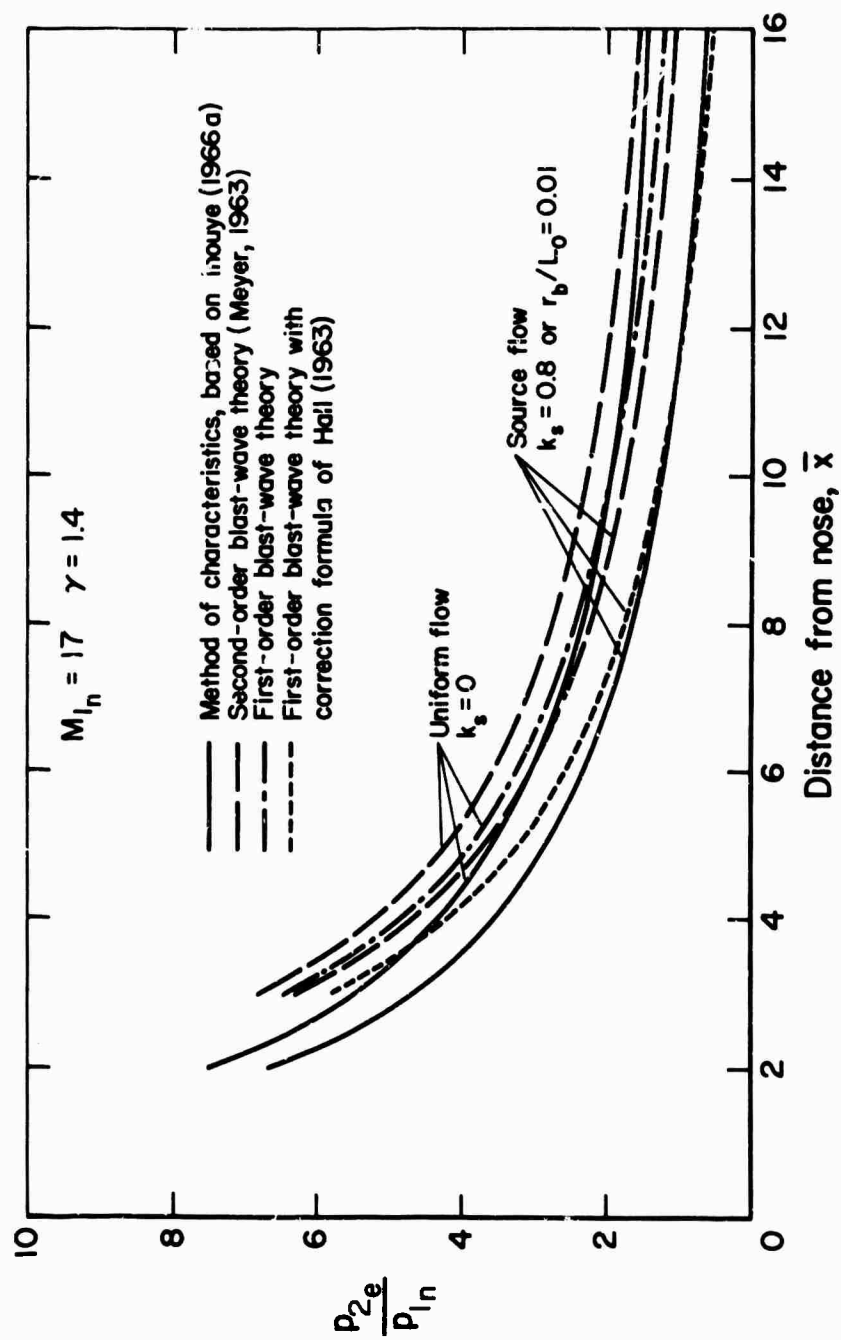
Figure 23. Surface pressure on hemisphere-cylinder model.

135
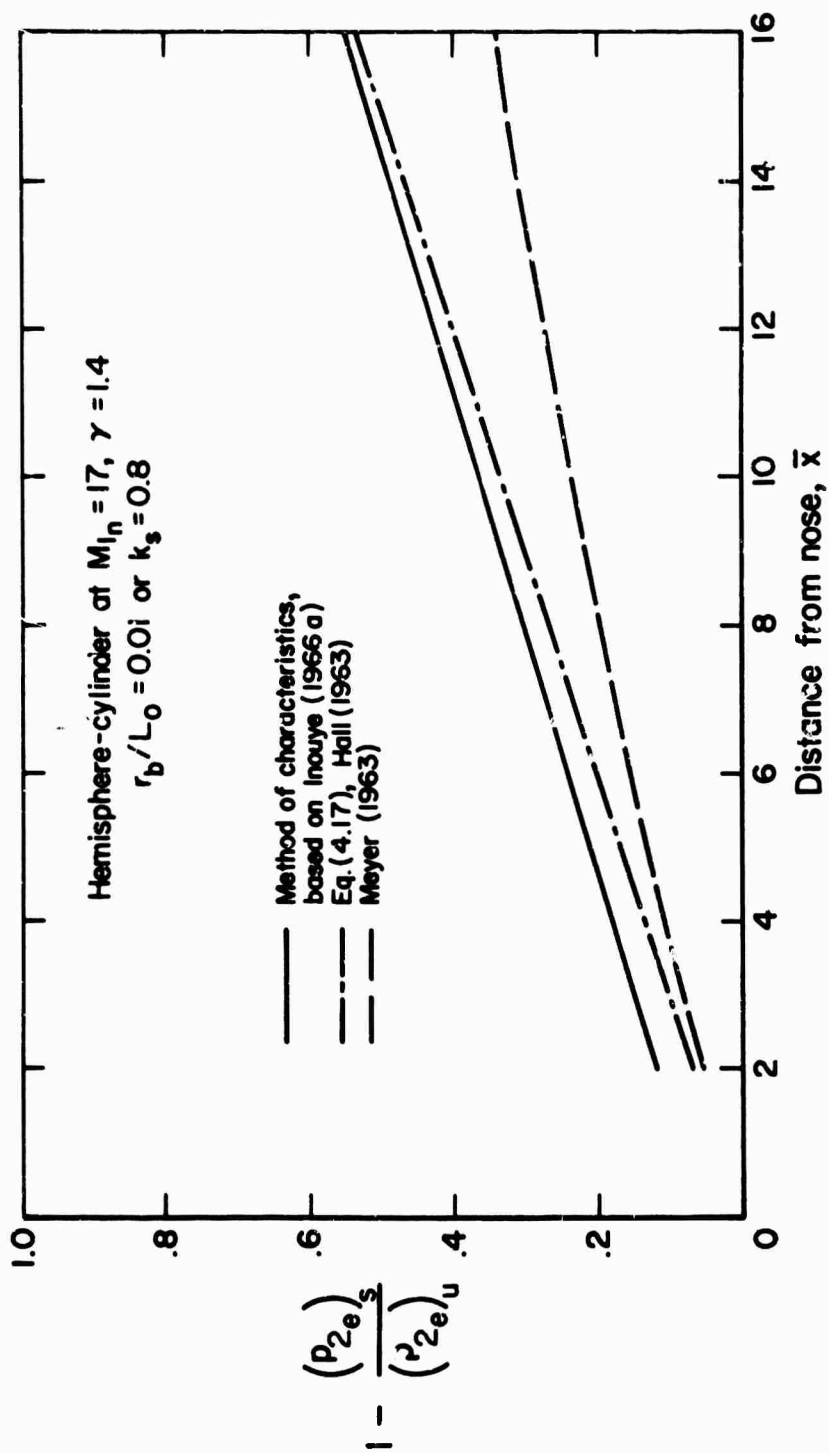
Figure 24. Correction curves for surface pressure.

136
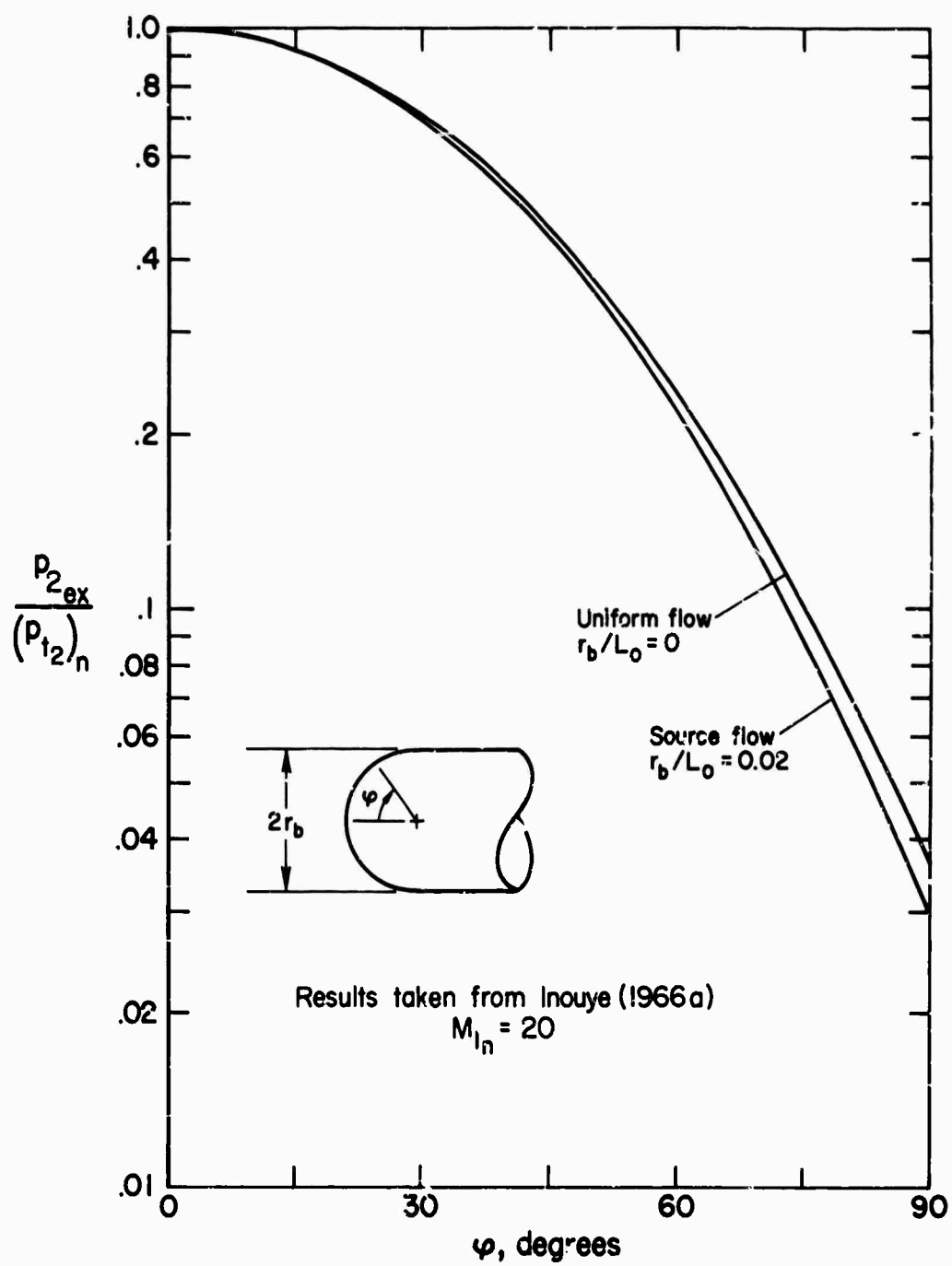
Figure 25. Surface-pressure distribution for hemispherical nose.
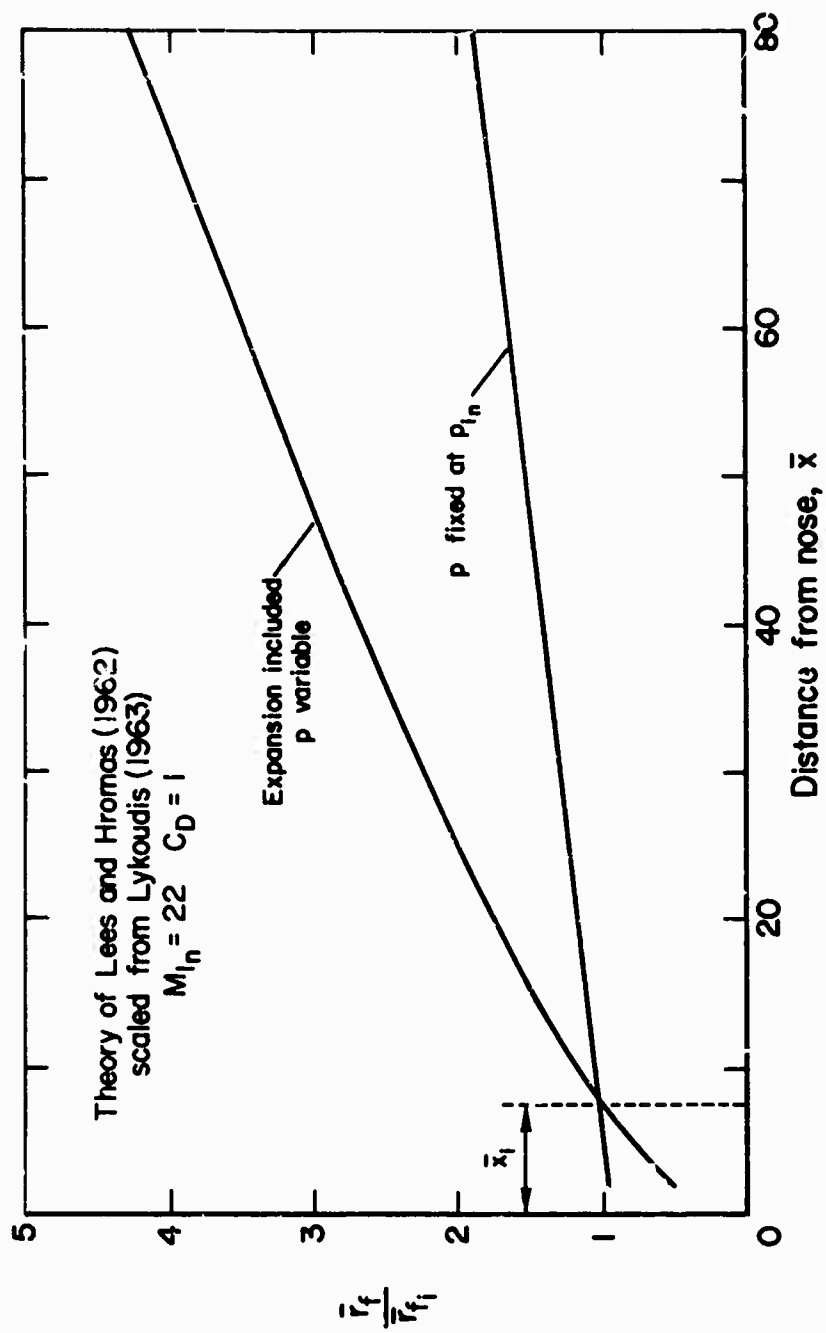
Figure 26. Effect of pressure variation on wake growth.

138
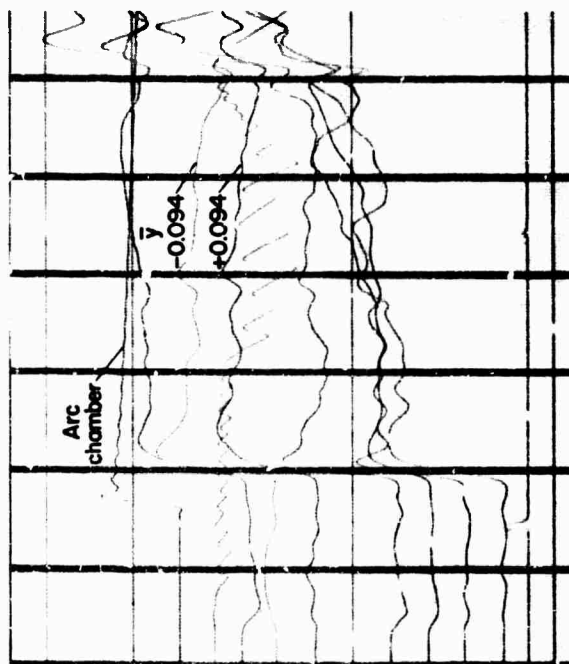
(b) Tunnel empty.

(a) In wake of sphere.
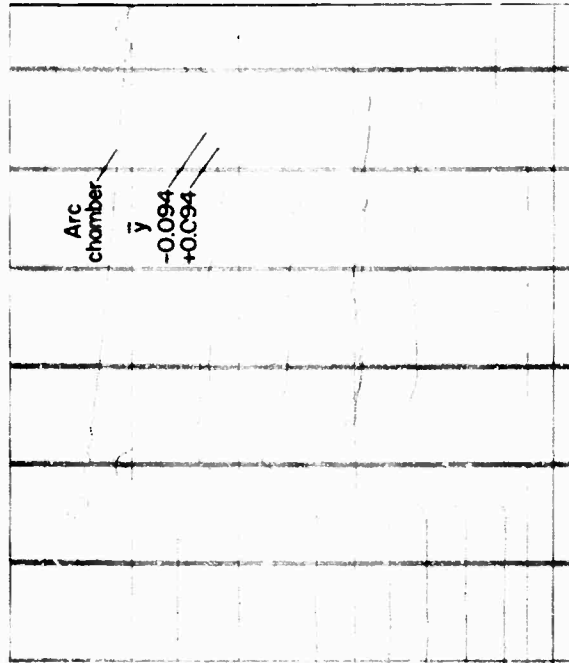
Figure 27. Oscillograph records for runs with radially traversing probe.

139
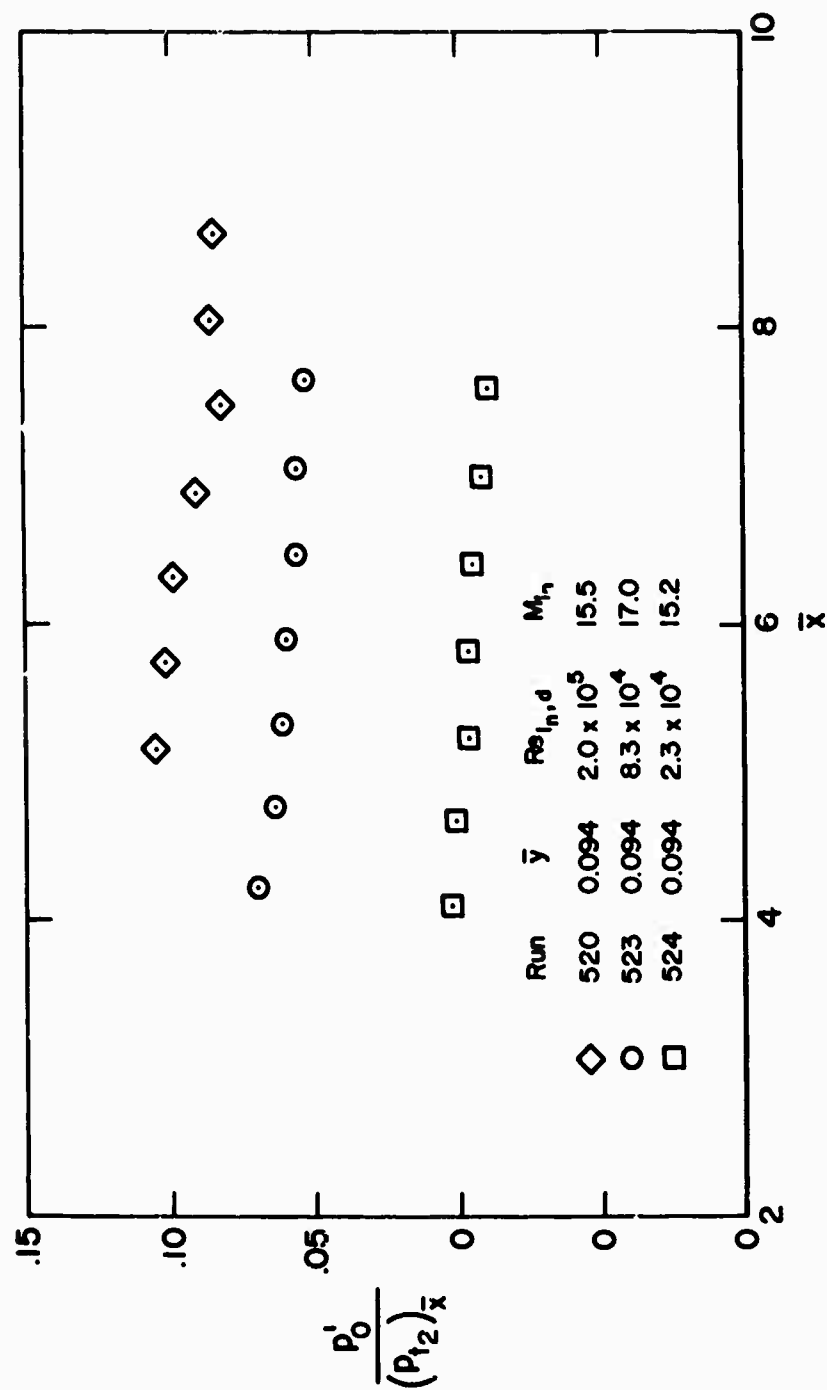
Figure 28. Longitudinal Pitot-pressure variation near wake axis.
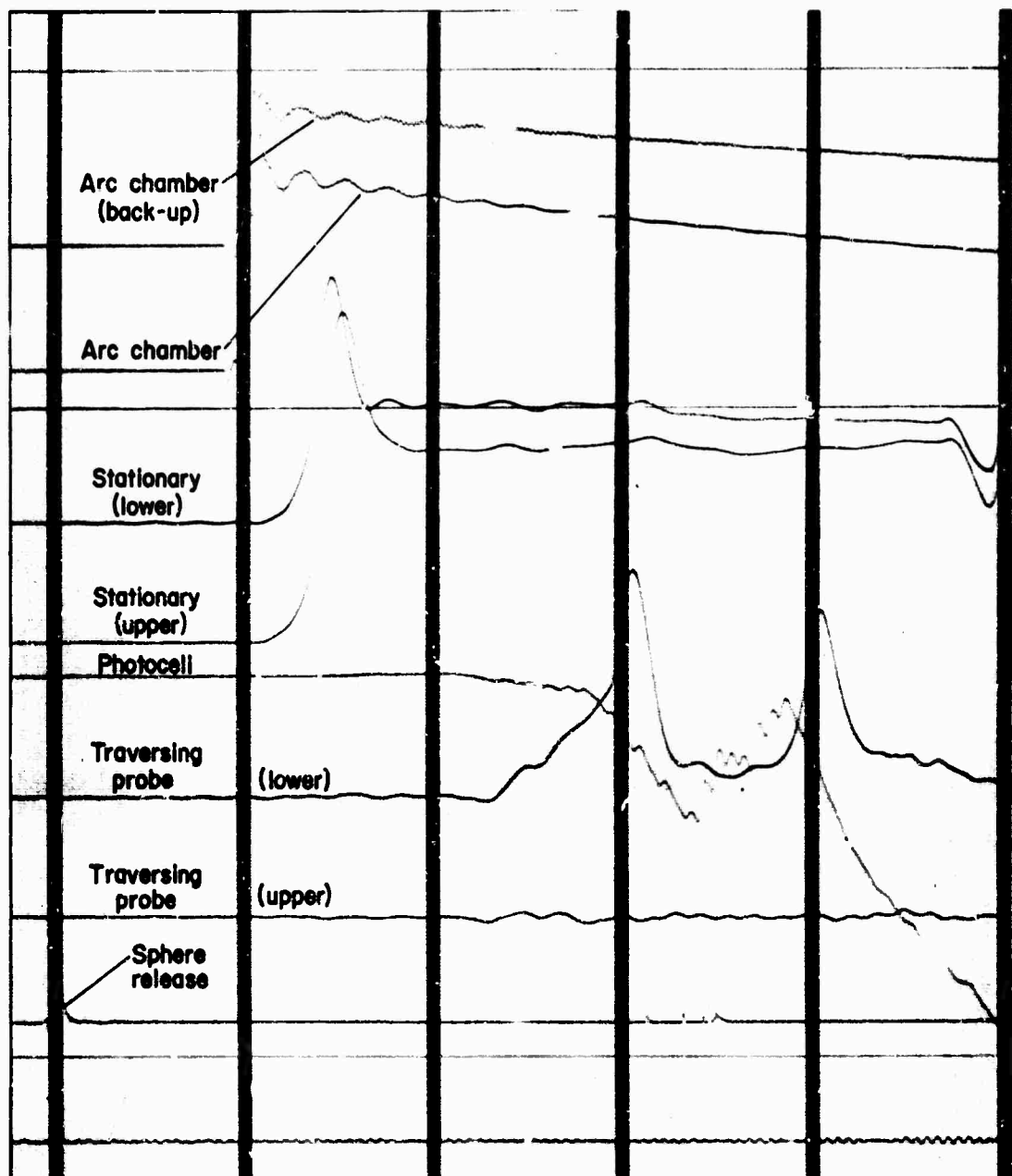
Figure 29. Oscillograph record for run with vertically
traversing probe.
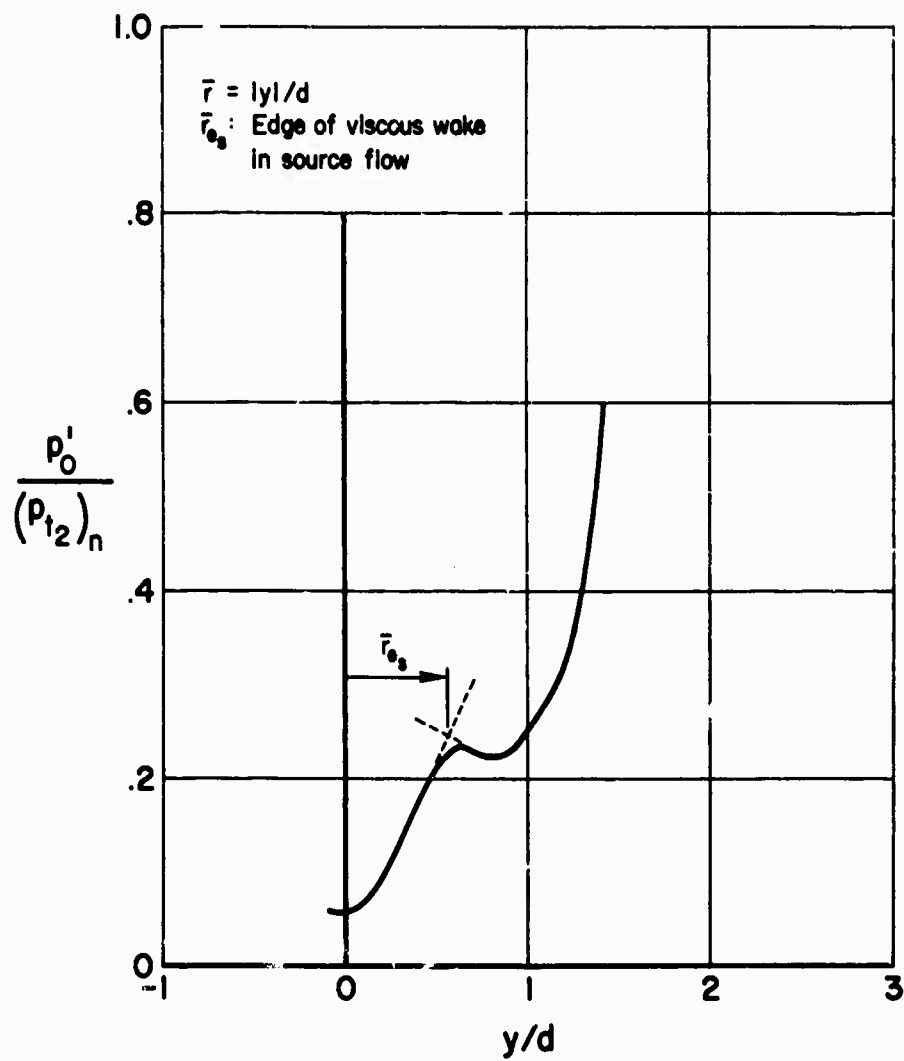
Figure 30.   Location of edge of viscous wake.
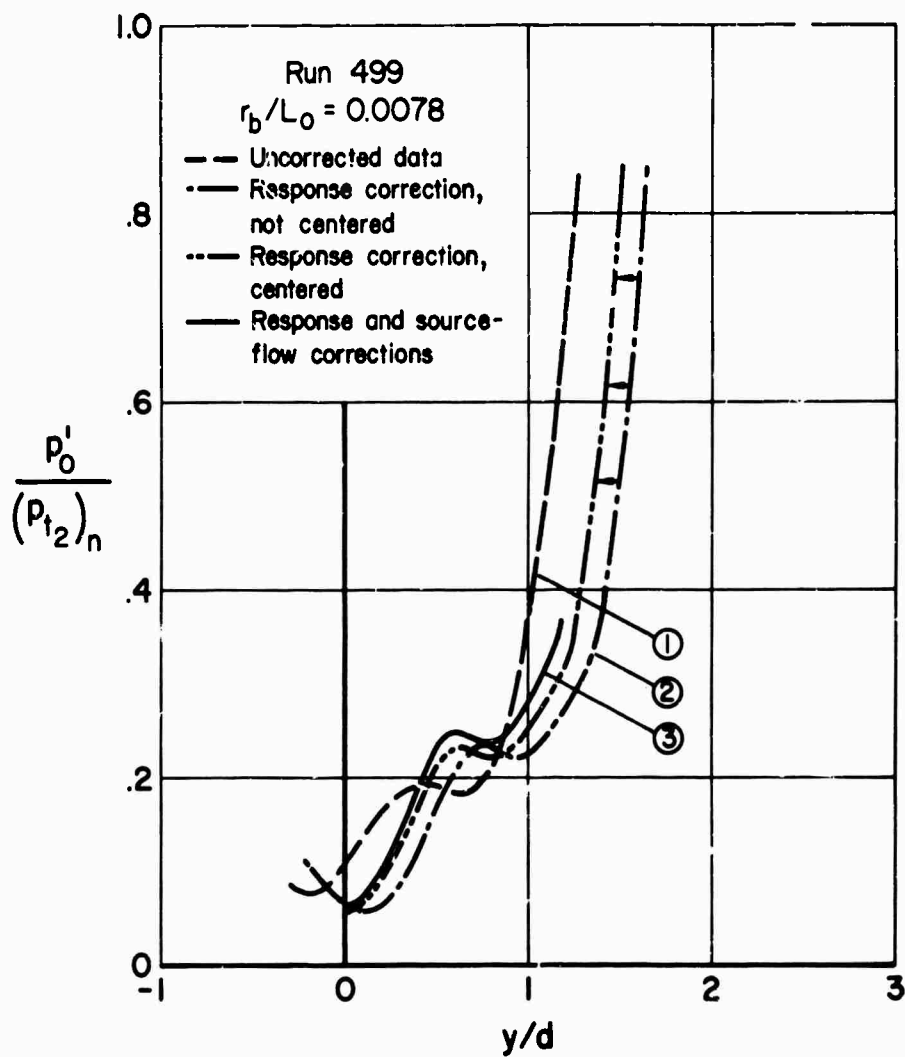
Figure 3I.   Typical Pitot-pressure results with
and without correction.

143

Run	Sta	x/d	r_b/L_0	$Re_{l_n,d}$	M_{l_n}
499	A	3.8	0.0078	2.18×10^4	16.0
498	B	5.1	0.0080	2.27×10^4	15.9
500	C	6.6	0.0083	2.19×10^4	15.6

---------- Response correction, centered

————— Response and source-flow corrections
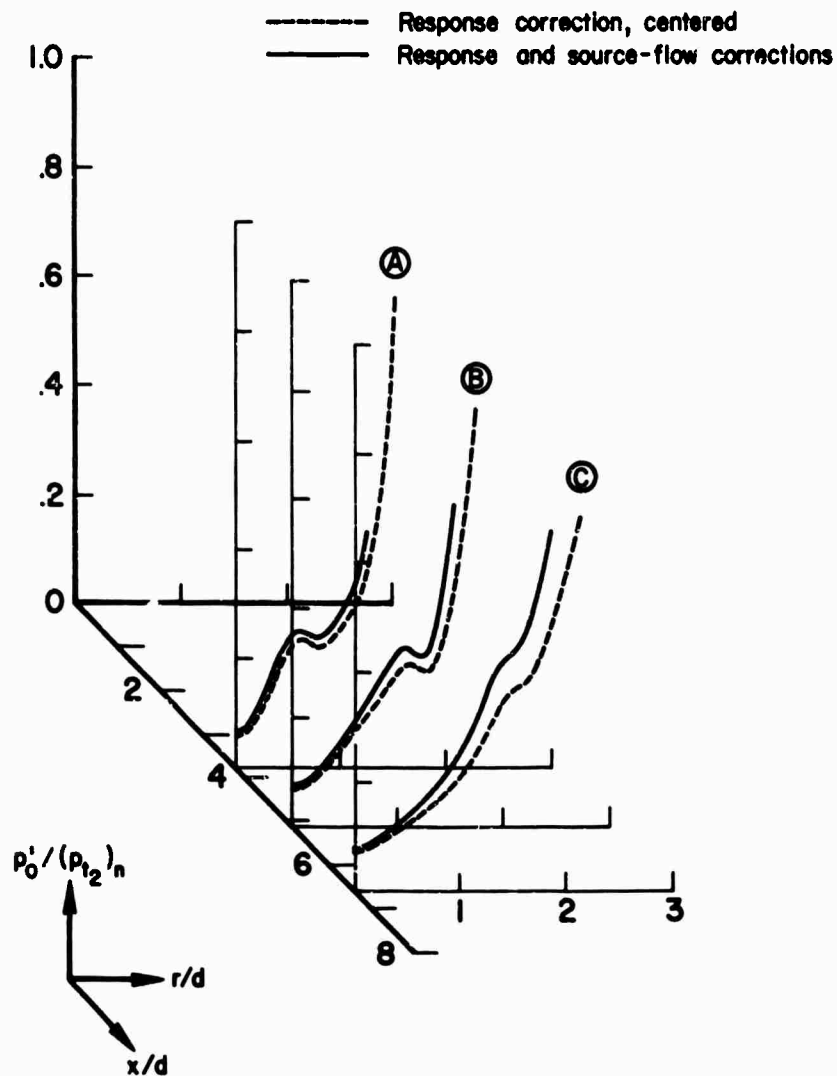
Figure 32. Corrected Pitot-pressure profiles for low Reynolds numbers.

144

Run	Sta	x/d	r_b/L_o	$Re_{i_n,d}$	M_{in}
494	A	3.8	0.0078	7.40×10^4	17.7
493	B	5.1	0.0080	7.96×10^4	17.6
495	C	6.6	0.0083	8.02×10^4	17.4

-------- Response correction, centered
———— Response and source-flow corrections
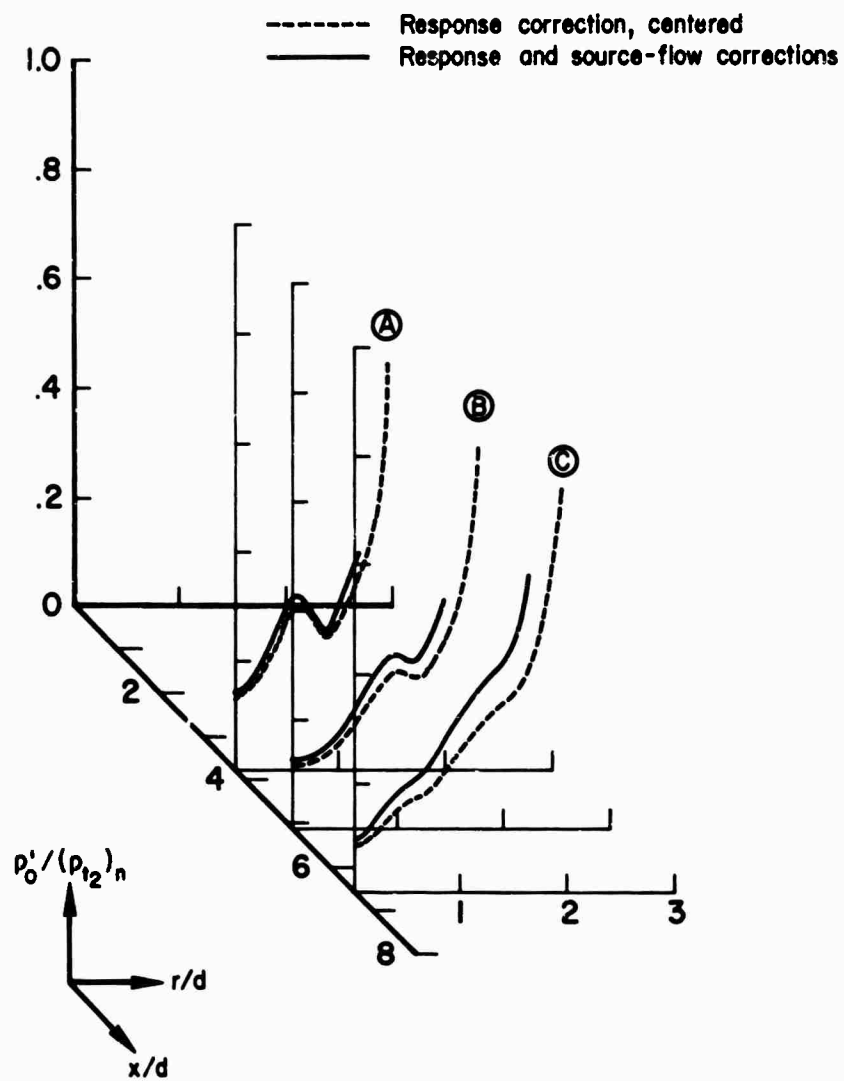
Figure 33. Corrected Pitot-pressure profiles for intermediate Reynolds numbers.

145

Run	Sta	x/d	r_b/L_o	$Re_{l_n,d}$	M_{l_n}
517	A	3.8	0.0078	1.77×10^5	16.2
512	B	5.1	0.0080	1.81×10^5	16.1
514	C	6.6	0.0083	1.80×10^5	15.9
518	D	8.1	0.0086	1.84×10^3	15.8
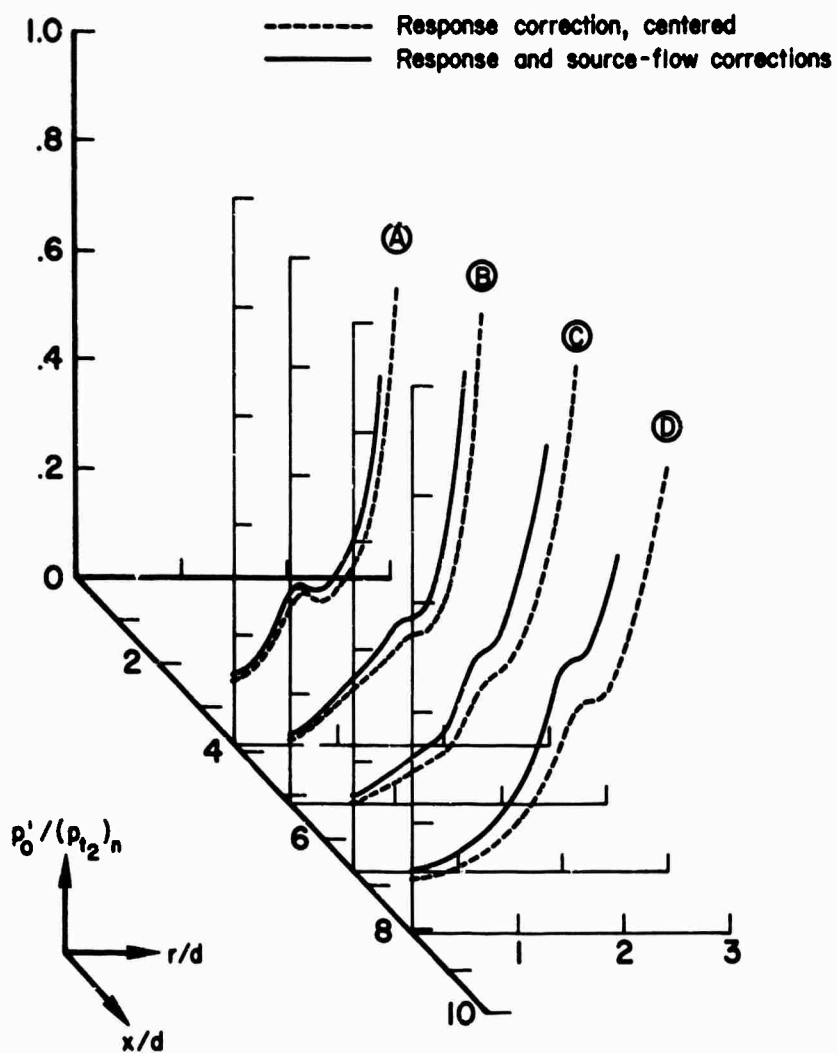
Figure 34. Corrected Pitot-pressure profiles for high Reynolds numbers.

146

Run	Sta	x/d	r_b/L_0	$Re_{l_n,d}$	M_{l_n}
471	B	5.1	0.0080	2.08×10^4	17.4
470	C	6.6	0.0083	2.01×10^4	17.1
469	D	8.1	0.0086	2.18×10^4	17.0
465	E	9.6	0.0089	2.15×10^4	16.8
462	F	11.1	0.0092	2.19×10^4	16.6
461	G	12.6	0.0096	2.24×10^4	16.4
459	H	15.6	0.0102	2.04×10^4	15.6

-------- Response correction, centered

———— Response and source-flow corrections
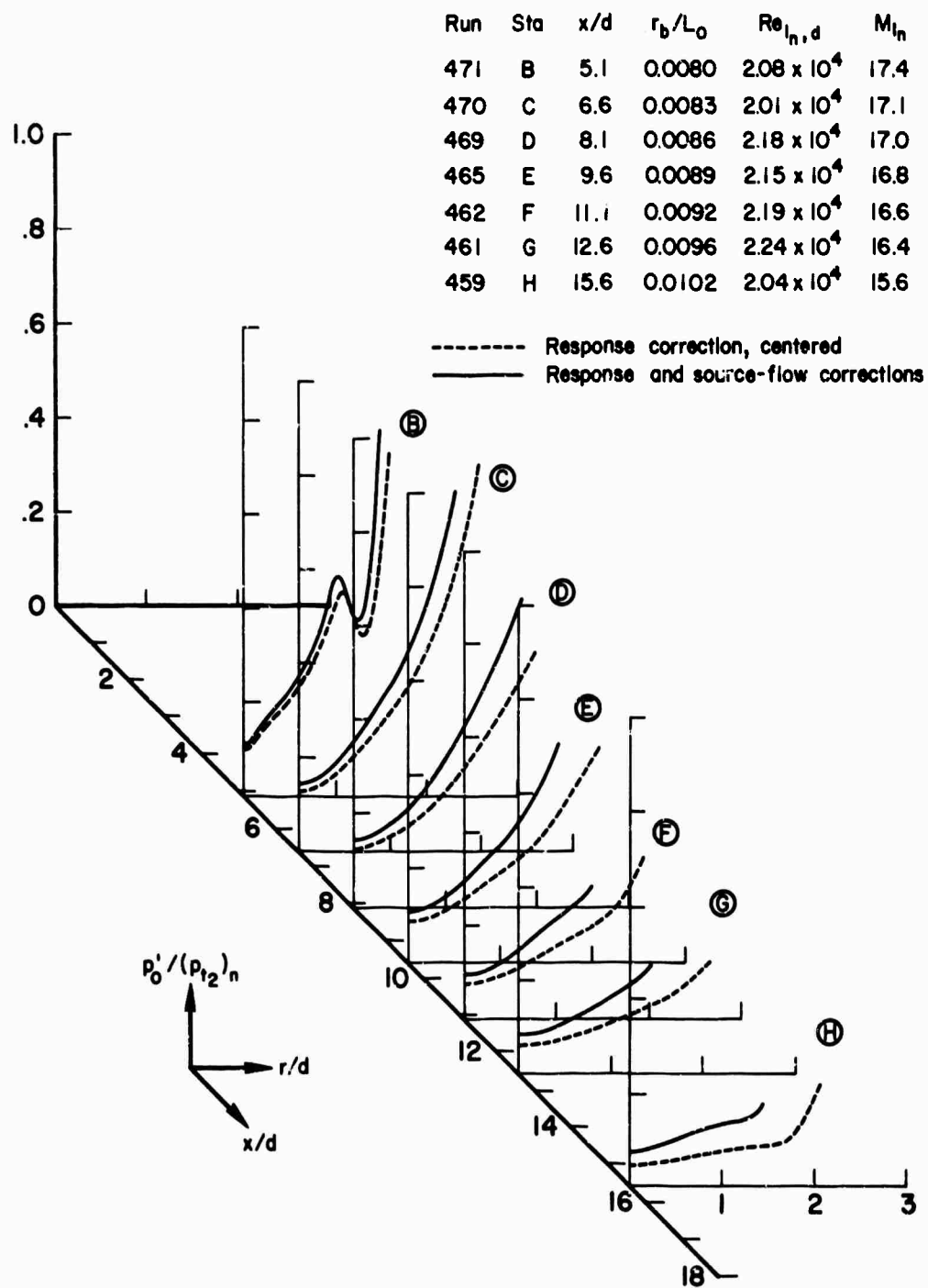
Figure 35. Corrected Pitot-pressure profiles for
low Reynolds numbers.

147
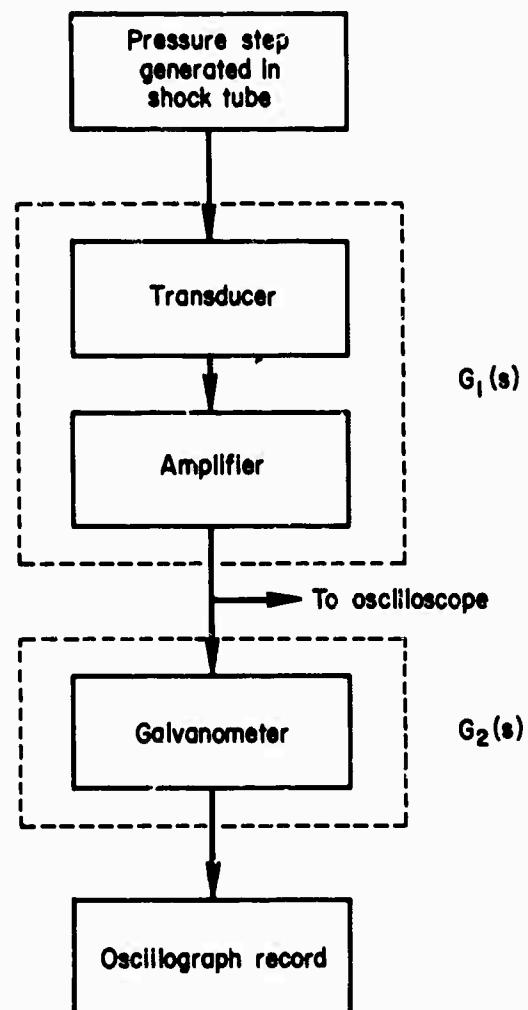
Figure 36. Schematic diagram of experimental procedure
for determining transfer function.
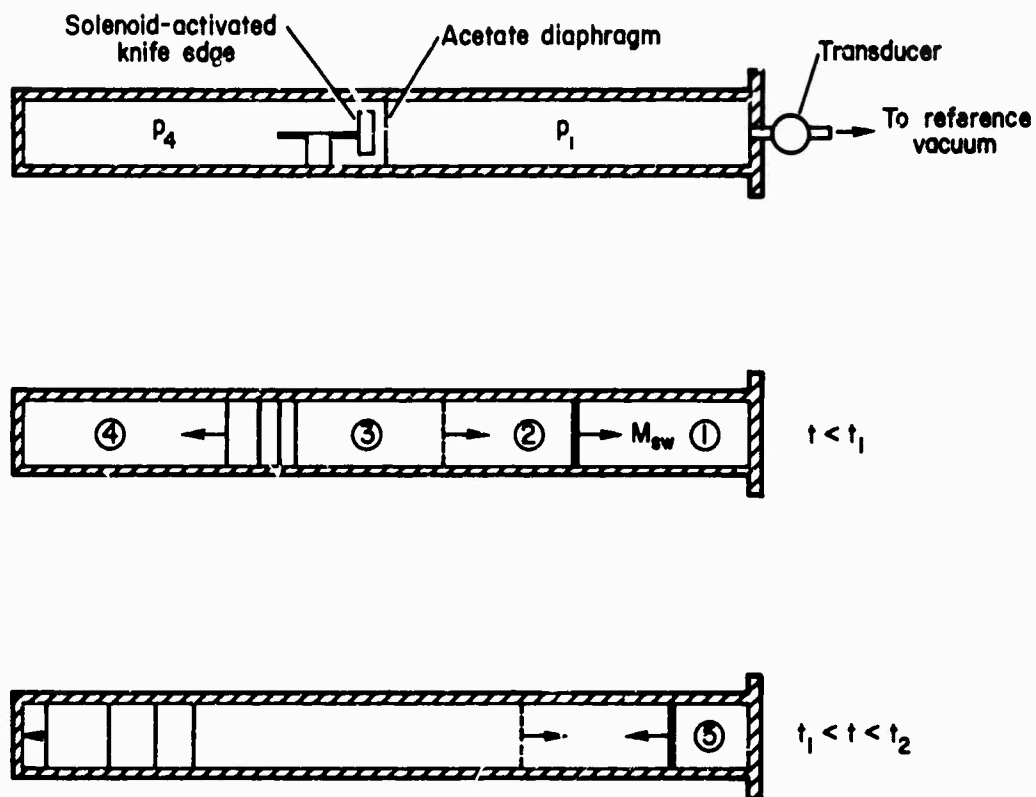
Figure 37. Shock-tube arrangement for response studies.

149
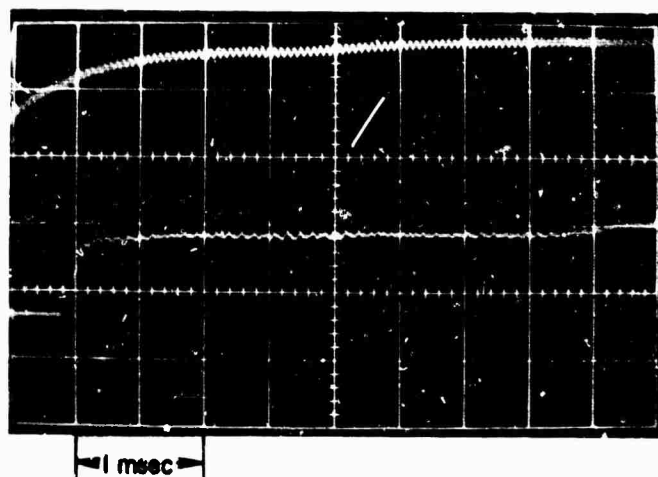
(a) Oscilloscope trace of amplifier output.
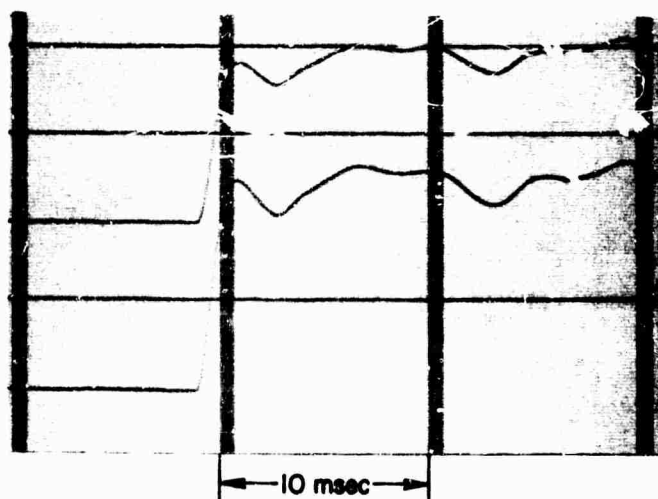
(b) Oscillograph record of galvanometer output
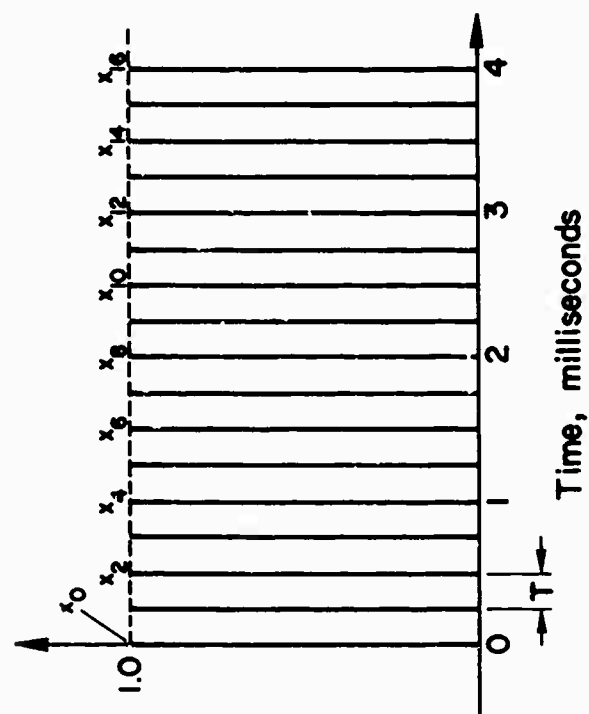(for two transducers).

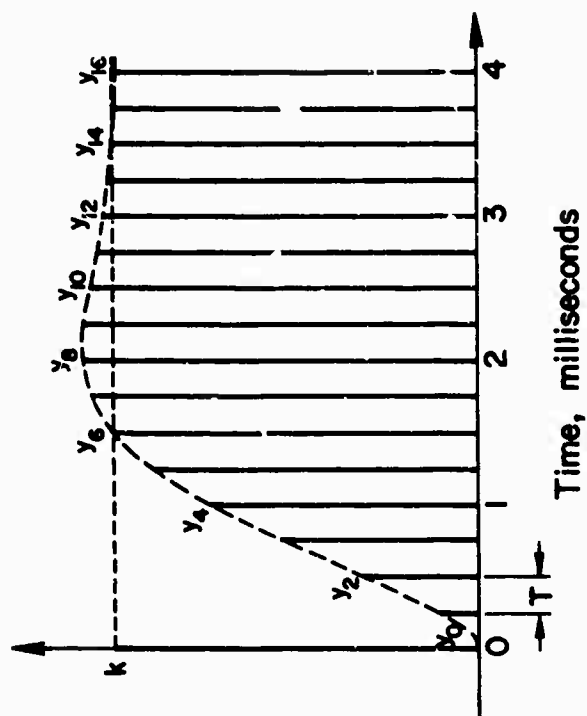Figure 38.   Response curves.

150
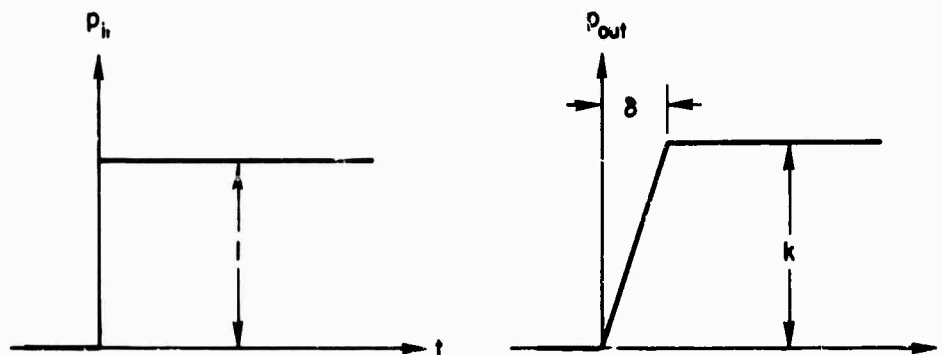
(a) Idealized response curve.
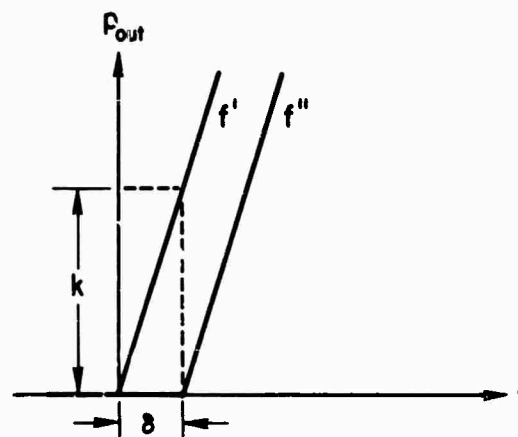
(b) Equivalent response diagram.

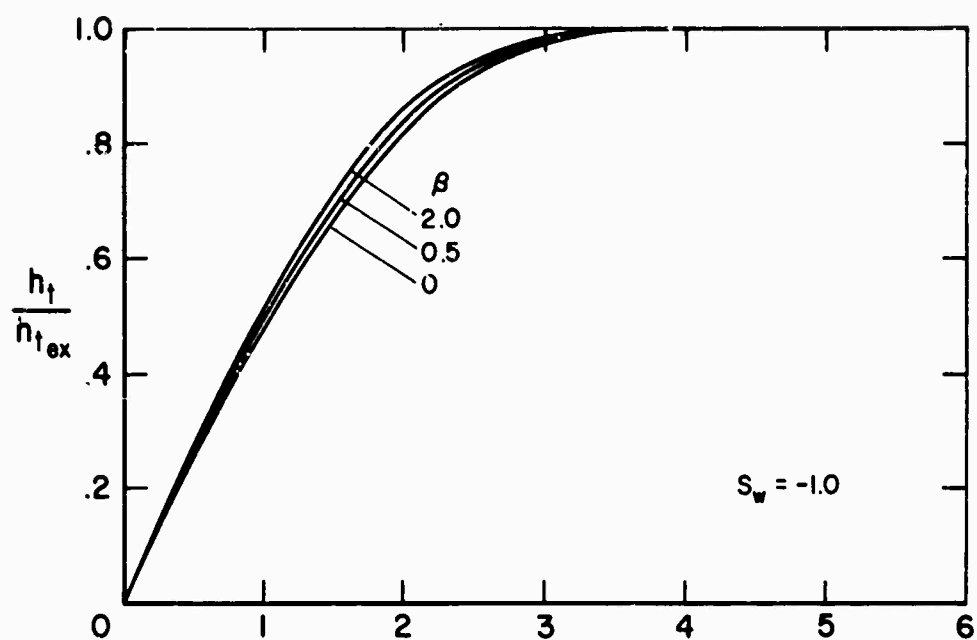Figure 39.   Idealization cf response characteristics
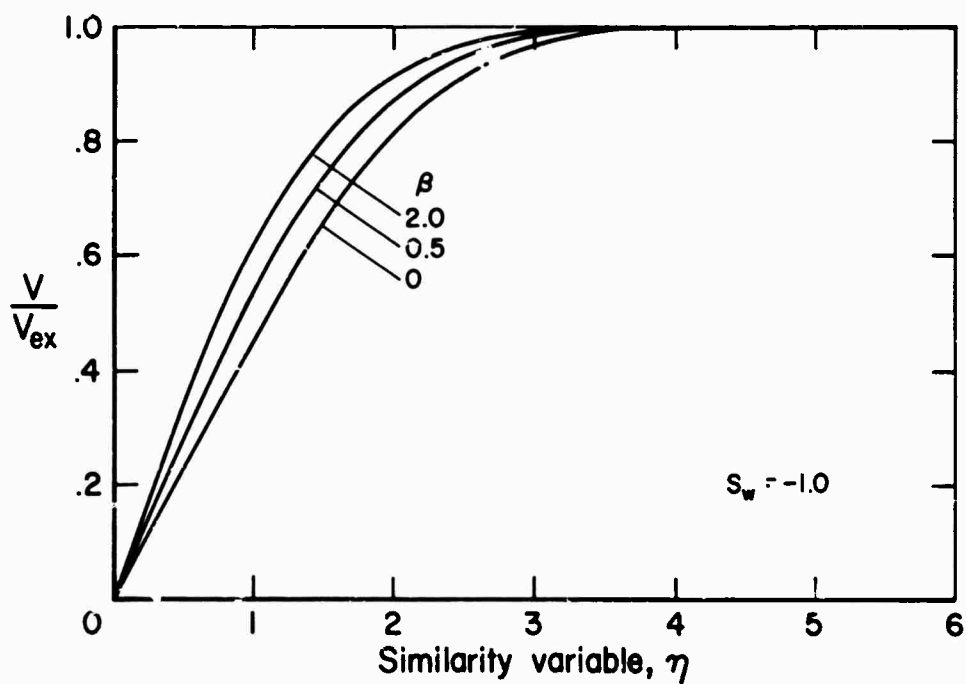of transducer-amplifier stage.

(b) Output.

Time, milliseconds

(a) Input.

Time, milliseconds

Figure 40. Sampled input and output.

152

(a) Total-enthalpy profile.

(b) Velocity profile.

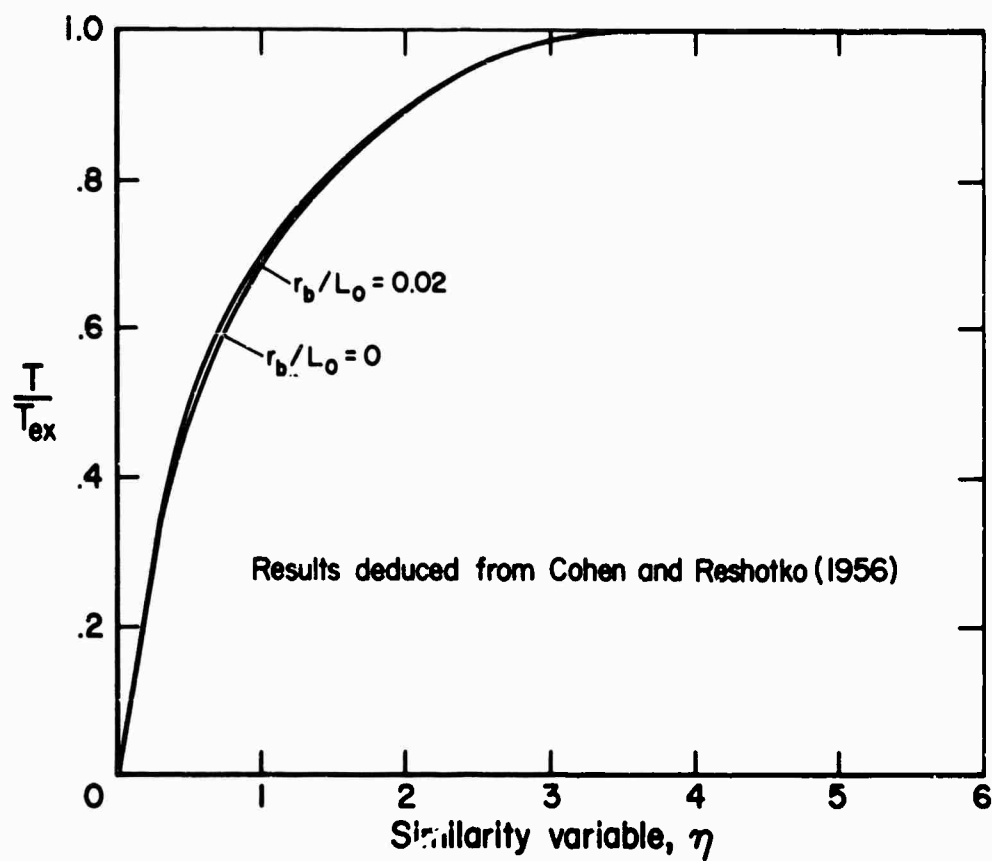Figure 41. Boundary-layer solutions of Cohen and Reshotko.

Figure 42. Comparison of temperature profiles in uniform
flow and source flow.

154